

Thermo-mechanical Modeling of a High Pressure Turbine Blade of an Airplane Gas Turbine Engine

Pedro Marques Borges Brandão

Thesis to obtain the Master of Science Degree in

Mechanical Engineering

Supervisors: Prof. Augusto Manuel Moura Moita de Deus
Prof. Virginia Isabel Monteiro Nabais Infante

Examination Committee:

Chairperson: Prof. Luís Manuel Varejão Oliveira Faria

Supervisor: Prof. Augusto Manuel Moura Moita de Deus

Members of the Committee: Prof. Maria de Fátima Reis Vaz

June 2015

Acknowledgment

I would like to thank my thesis supervisor, Professor Augusto Moita de Deus, for all his guidance, patience and help, as well as for creating an environment of trust and ease, and mainly for always being available to address all and any doubts, difficulties or issues, and providing valuable advice, suggestions and much needed constructive criticism during this project.

I would also like to thank my co-supervisor, Professor Virginia Infante, whom has accompanied this project since its inception and provided me with invaluable help, advice, and contacts, as well as directing me into the mentorship of my thesis advisor.

This project would also have been impossible without the support of the Maintenance and Engineering Management of SATA Air Açores, and I would like to specially thank its director, Engineer Pedro Viveiros, with whom the idea of this thesis was first developed, for providing me all the conditions for this project to be made, and also my colleagues at the Engineering Department, especially Engineering Manager Nuno Rangel, for all the help, advice and patience they afforded me, as well as for the invaluable data on which this project is based.

I would like to thank Professor Luis Sousa and Professor Marco Leite, for their assistance in the creation of the part's 3D model, Professor Luís Alves and Engineer Isabel Nogueira, for their help in extracting some of the scrap part's properties and composition data, and specially Professor Rui Ruben, for all his help and expertise with the Abaqus software, thus providing me the tools to complete this project.

I would also like to thank all my friends and colleagues, that for the past years have accompanied me in this journey, without whom I wouldn't have been able to reach this point in my life, my friends at TUCA, my teammates at AEIST Waterpolo and specially Vasco van Zeller, whose direct help with this project spared me countless hours of headaches.

To Débora Simões, I would like to thank her for her love, caring and for being there for me on the more frustrating and tough parts of this project.

Last but not least, I would like to thank my family, especially my mother, father and sister, for their infinite and unwavering love, patience and support, and for putting up with me for all these years, especially for the duration of this project.

Resumo

Durante a sua operação, os componentes de motores aeronáuticos estão sujeitos a condições de operação cada vez mais exigentes, tais como ciclos de temperaturas elevadas, elevadas velocidades de rotação e elevadas pressões, especialmente no caso das pás de turbina de alta pressão. Estas condições obrigam estas pás a estarem sujeitas a diferentes tipos de degradação dependente do tempo, um dos quais é a fluência, um mecanismo de ruína que pode reduzir significativamente a vida do componente, quer pela criação de fendas por fluência, quer através de sobre alongamento da pá que pode entrar em contacto com o revestimento interno da turbina.

Deste modo, o objetivo deste projeto é a criação de um modelo utilizando o método dos elementos finitos, a fim de ser capaz de prever o comportamento da pá da turbina de alta pressão em fluência e o seu alongamento ao longo do tempo.

A fim de atingir este objetivo, registos de voo de uma aeronave específica, providenciados por uma companhia aérea, foram utilizados para se obterem dados térmicos e mecânicos, isto é, a variação de temperatura entre turbinas e a variação de velocidade de rotação da turbina de alta pressão, para três tipos de ciclo de voo diferentes.

Para criar o modelo 3D necessário para a análise pelo método dos elementos finitos, uma pá de turbina de alta pressão descartada foi utilizada, assim como para obter a composição e propriedades do material, também necessárias para essa análise. A pá descartada foi digitalizada utilizando um scanner 3D, e um software de modelação 3D foi utilizado para o modelo. A fim de determinar a sua composição química, foi efetuada sobre a superfície da pá descartada uma microscopia por varrimento de eletrões, assim como uma análise por espectroscopia de energia dispersiva.

Todos os dados obtidos foram introduzidos no programa de elementos finitos e diferentes simulações foram efetuadas, primeiro com um modelo 3D simplificado de um paralelepípedo, para se aferir o modelo, seguidas de simulações com o modelo 3D simplificado obtido através da pá descartada.

Estas simulações geraram resultados aceitáveis, apesar das limitações do modelo, uma vez que muitos aspetos importantes tiveram que ser ignorados ou simplificados. Não obstante, este modelo é visto como um bom passo em diante, e diversas melhorias, que podem ser feitas a fim de se aumentar a precisão do modelo, foram identificadas.

Palavras-Chave

Pá de Turbina de Alta Pressão, Fluência, Análise pelo Método dos Elementos Finitos, Modelo 3D, Simulação.

Abstract

During their operation, modern aircraft engine components are subjected to increasingly demanding operating conditions, such as high temperature cycles, rotation speeds and pressure, especially the high pressure turbine (HPT) blades. These conditions make these blades undergo different types of time-dependent degradation, one of which is creep, a failure mechanism that can significantly reduce the parts life, either by generation of cracks, or by over-elongation of the blade tip, that may contact with the turbine's casing.

Thus, the goal of this project is to create a model using the finite element method (FEM), in order to be able to predict the HPT blade's creep behavior and its elongation over time.

In order to accomplish this, flight data records (FDR) for a specific aircraft provided by an aviation company were used to obtain thermal and mechanical data, i.e. inter turbine temperature (ITT) variation and HPT rotation speed variation, for three different flight cycles.

In order to create the 3D model needed for the FEM analysis, a HPT blade scrap was used, as well as to obtain the blade's chemical composition and material properties, also needed for that analysis. The blade scrap was scanned using a 3D mapping scanner, and 3D modeling software was used to create the model. In order to determine the scrap part's chemical composition, surface scanning electron microscopy (SEM) was performed as well as energy dispersive spectroscopy (EDS) analysis.

All the data gathered was fed into the FEM software used and different simulations were ran, first with a simplified 3D rectangular block shape to evaluate the model, and then with the simplified 3D model obtained from the blade scrap.

The simulations yielded suitable results, despite the limitations of the model, as many important considerations had to be taken out or simplified. Nevertheless, it is seen as a good work in progress and several improvements, that can be made in order to achieve greater model accuracy, were identified.

Keywords

High Pressure Turbine Blade, Creep, Finite Element Method, 3D Model, Simulation.

Table of contents

| | |
|--|------------|
| ACKNOWLEDGMENT | I |
| RESUMO | III |
| PALAVRAS-CHAVE | III |
| ABSTRACT..... | V |
| KEYWORDS..... | V |
| TABLE OF CONTENTS | VII |
| LIST OF TABLES | IX |
| LIST OF FIGURES | XI |
| LIST OF SYMBOLS | XV |
| 1. INTRODUCTION..... | 1 |
| 2. BACKGROUND..... | 2 |
| 2.1. GAS TURBINE CYCLE | 2 |
| 2.1.1. <i>The Brayton Thermal Cycle</i> | 2 |
| 2.1.2. <i>The Split-shaft Simple Cycle</i> | 4 |
| 2.2. AIRCRAFT GAS TURBINE ENGINES..... | 5 |
| 2.2.1. <i>Turbojet</i> | 5 |
| 2.2.2. <i>Turbofan</i> | 5 |
| 2.2.3. <i>Turboprop</i> | 6 |
| 2.3. THE PW150A TURBOPROP ENGINE | 7 |
| 2.3.1. <i>Overview</i> | 7 |
| 2.3.2. <i>Reduction Gearbox Module</i> | 7 |
| 2.3.3. <i>Turbomachinery Module</i> | 8 |
| 2.4. HIGH PRESSURE TURBINE (HPT) BLADE | 16 |
| 2.4.1. <i>Function of HPT Blades</i> | 17 |
| 2.4.2. <i>Common Failure Mechanisms</i> | 18 |
| 2.4.3. <i>Materials</i> | 24 |
| 2.4.4. <i>Protection Modes and Cooling Schemes</i> | 29 |
| 2.5. CREEP IN NICKEL-BASE SUPPERALLOY HPT BLADES..... | 32 |
| 2.5.1. <i>Creep Characteristics</i> | 32 |
| 2.5.2. <i>Creep Inducing Factors</i> | 33 |
| 2.5.3. <i>Superalloy Microstructure</i> | 33 |

| | |
|---|-----------|
| 3. METHODOLOGY | 36 |
| 3.1. PROBLEM DESCRIPTION | 36 |
| 3.2. FLIGHT DATA RECORD PROCESSING | 37 |
| 3.3. PART REVERSE ENGINEERING AND MODELING | 42 |
| 3.3.1. <i>Part Modeling</i> | 42 |
| 3.3.2. <i>Superalloy Material Data and Composition</i> | 45 |
| 3.3.3. <i>Superalloy Selection and Properties</i> | 49 |
| 3.4. FINITE ELEMENT MODELING..... | 55 |
| 3.4.1. <i>Rectangular Block Model</i> | 55 |
| 3.4.2. <i>Blade Model</i> | 61 |
| 4. RESULTS AND DISCUSSION | 66 |
| 4.1. THERMAL ANALYSIS RESULTS..... | 67 |
| 4.2. ANALYSES COMPARISON | 68 |
| 4.3. ELASTOPLASTIC ANALYSIS VS CREEP ANALYSIS..... | 70 |
| 4.4. CYCLE ACCUMULATION ANALYSIS | 74 |
| 5. CONCLUSION..... | 79 |
| 5.1. FUTURE WORK | 80 |
| 6. REFERENCES | 81 |
| APPENDIX..... | 2 |
| APPENDIX A – EXAMPLE EXCERPT FROM ORIGINAL FLIGHT DATA RECORD FILE PROVIDED BY THE AIRLINE COMPANY..... | 2 |
| APPENDIX B – MESH CONVERGENCE AND ERRORS..... | 3 |
| APPENDIX C – TEMPERATURE DISTRIBUTION ON THE THERMAL MODEL..... | 5 |
| APPENDIX D – DISTRIBUTION OF STRESS, STRAIN AND DISPLACEMENT FOR THE REMAINING DIRECTIONS..... | 9 |

List of Tables

Table 3.1 – Type of data collected from the FDR 37

Table 3.2 – IATA airport codes and coordinates [72]..... 37

Table 3.3 – Flight Routes for each aircraft 38

Table 3.4 – Flight cycle periods and number of cycles for expected lifetime for Engine 1 42

Table 3.5 – Zscanner 700 specs [73]..... 43

Table 3.6 – HPT blade weight measurements 45

Table 3.7 – EDS of Top section 47

Table 3.8 – EDS of Body section 48

Table 3.9 – EDS of Base section 48

Table 3.10 – Chemical composition wt% [74] 49

Table 3.11 – Temperature-dependent thermal and mechanical properties of the CMSX-4 superalloy [75] 50

Table 3.12 – Physical constants and thermal properties provided for TMS-75 superalloy [76].. 50

Table 3.13 – Tensile strength provided for the TMS-75 superalloy [76] 52

Table 3.14 – Creep rupture strength provided for the TMS-75 superalloy [76] 52

Table 3.15 - Temperature-dependent thermal and mechanical properties of the TMS-75 superalloy 53

Table 3.16 – Temperature and stress dependent plastic strain for the TMS-75 superalloy 53

Table 3.17 – Steady-state creep constants for the TMS-75 superalloy 54

Table 4.1 – Nodal results for one PDL-FNC flight cycle. 68

Table 4.2 – Nodal results for trend study of 3000 flight hours 78

Table A1 – Creep analysis associated error for 0,75 mm seed size for the blade model. A3

Table A2 – Creep analysis associated error with 0,6 mm seed size for the rectangular block model..... A4

Table A3 – Displacement (U2) error associated with 0,75 mm seed size for the blade model. . A4

Table A4 – Displacement (U2) error associated with 0,6 mm seed size for the rectangular block model..... A4

List of Figures

| | |
|--|----|
| Figure 2.1 – The air-standard Brayton Cycle. [7] | 3 |
| Figure 2.2 – The Split-shaft Simple Cycle. [9]..... | 4 |
| Figure 2.3 – Schematic diagram of a) centrifugal flow turbojet engine; b) axial flow turbojet engine.[13][14]..... | 5 |
| Figure 2.4 – Schematic diagram of a) 2-spool, low-bypass turbofan engine; b) high-bypass turbofan engine. [18] [19] | 6 |
| Figure 2.5 – Schematic diagram of a turboprop engine. [22]..... | 6 |
| Figure 2.6 – Schematic diagram of the PW150A Turboprop Engine. [26]..... | 7 |
| Figure 2.7 – Reduction Gear Box Module. [28]..... | 8 |
| Figure 2.8 – Turbomachinery Module. [27] | 8 |
| Figure 2.9 – LP Compressor. [31]..... | 10 |
| Figure 2.10 – Pressure and velocity during compression axial flow. [32] | 10 |
| Figure 2.11 – HP Compressor. [33] | 11 |
| Figure 2.12 – Pressure and velocity during centrifugal flow. [34] | 11 |
| Figure 2.13 – Combustion Section. [35]..... | 12 |
| Figure 2.14 – Combustor. [36] | 12 |
| Figure 2.15 – Power Turbine Section. [39] | 13 |
| Figure 2.16 – Pressure and velocity in the flow of a reaction turbine. [40] | 14 |
| Figure 2.17 – HP Turbine. [41]..... | 15 |
| Figure 2.18 – LP Turbine. [42] | 15 |
| Figure 2.19 – Power Turbines. [43]..... | 16 |
| Figure 2.20 – Example of an HPT blade. [45]..... | 16 |
| Figure 2.21 – Typical pressure, temperature and velocity profiles in a gas turbine engine. [46] | 17 |
| Figure 2.22 – a) Fatigue cracking found in trailing edge of blade (right of pencil mark); b) SEM image of crack surface showing striations. [49] | 19 |
| Figure 2.23 – a) Creep damage; b) Grain boundary separation; c) Appearance of creep cracking in a directionally solidified blade material. [49]..... | 20 |
| Figure 2.24 – Sulphidation attack of a turbine blade. [49]..... | 21 |
| Figure 2.25 – Erosive wear of leading edges of rotor blades. [51] | 22 |
| Figure 2.26 – Scratches on protective coating conducive to corrosion on the leading edge of a turbine blade. [51]..... | 23 |
| Figure 2.27 – Basic operations of the investment casting process. [57]..... | 27 |
| Figure 2.28 – Investment casting of single-crystal turbine blade. [59]..... | 28 |
| Figure 2.29 – Grain structures of single-crystal, directionally solidified, and conventionally cast turbine blades. [54]..... | 28 |
| Figure 2.30 – schematic of a thermal barrier coating system. [62] | 30 |
| Figure 2.31 – Schematic of a modern gas turbine blade with common cooling techniques. [63]31 | |

| | |
|--|----|
| Figure 2.32 – Schematic of a creep curve exhibiting the three stages of creep. [67] | 32 |
| Figure 2.33 – Effect of temperature and stress on creep. [68] | 33 |
| Figure 2.34 – a) Undamaged structure of γ' quasi-cuboids; b) rafted γ' resulting from exposure to stress at high temperature; c) re-precipitated γ' . [49]..... | 34 |
| Figure 2.35 – a) Crystallographic pores; (b) Crack growth with nucleation at a pore and propagation along γ' -rafts. [70]..... | 35 |
| Figure 2.36 – Precipitation of TCP phases. [70] | 35 |
| Figure 3.1 – PW150A engines of the Bombardier DHC8-400 aircraft in flight. [71]..... | 36 |
| Figure 3.2 – Engine 1 flight cycle curves for PDL-FNC flight route for a) NH; b) ITT. | 39 |
| Figure 3.3 – Engine 1 flight cycle curves for SJZ-TER flight route for a) NH; b) ITT. | 39 |
| Figure 3.4 – Engine 1 flight cycle curves for PDL-HOR flight route for a) NH; b) ITT. | 39 |
| Figure 3.5 – PDL-FNC flight route's averaged cycles for a) TIT; b) ω HPT. | 41 |
| Figure 3.6 – SJZ-TER flight route's averaged cycles for a) TIT; b) ω HPT. | 41 |
| Figure 3.7 – PDL-HOR flight route's averaged cycles for a) TIT; b) ω HPT. | 41 |
| Figure 3.8 – HPT blade scrap. | 42 |
| Figure 3.9 – 3D surface mapping of the HPT blade scrap in the ZScan software..... | 44 |
| Figure 3.10 – a) Polygon mesh of part surface; b) editable surface of part. | 44 |
| Figure 3.11 – a) HPT blade 3D model a) with drawing edges; b) without drawing edges. | 44 |
| Figure 3.12 – HPT blade's base width. | 45 |
| Figure 3.13 – SEM and EDS HPT blade sections. | 46 |
| Figure 3.14 – Young's modulus obtained using rectangular parallelepiped resonance. [76] | 51 |
| Figure 3.15 – Thermal conductivity obtained using the Laser-Flush Method. [76] | 51 |
| Figure 3.16 – Specific heat obtained using an adiabatic calorimeter (Nernst Method). [76] | 51 |
| Figure 3.17 – Rectangular block created in the Part Module..... | 55 |
| Figure 3.18 – Definition of analysis steps in the Step Module. | 56 |
| Figure 3.19 – Predefined field created using the Load Module. | 57 |
| Figure 3.20 – Boundary condition applied on the surface of the rectangular block..... | 57 |
| Figure 3.21 – Definition of seed size in the Mesh Module. | 58 |
| Figure 3.22 – Definition of centrifugal load using the Load Module. | 59 |
| Figure 3.23 – Definition of boundary condition in the Load Module..... | 60 |
| Figure 3.24 – Definition of Predefined Field-2 in Step-Cent. | 60 |
| Figure 3.25 – Definition of predefined field for isothermal analyses in the Load Module. | 61 |
| Figure 3.26 – a) Imported blade model; b) Repositioned blade model and secondary coordinate system. | 62 |
| Figure 3.27 – Thermal boundary condition on surface of blade model..... | 63 |
| Figure 3.28 – Definition of centrifugal load using the Load Module. | 63 |
| Figure 3.29 – Faces constrained normal to contact faces (ZZ axis)..... | 64 |
| Figure 3.30 – Faces constrained normal to the vertical direction (YY axis)..... | 64 |
| Figure 3.31 – Faces pinned along all directions. | 65 |
| Figure 3.32 – Faces constrained along the axial direction (XX axis). | 65 |

| | |
|---|----|
| Figure 4.1 – Nodes selected for a) the blade model; b) the rectangular block model. | 66 |
| Figure 4.2 – Temperature distribution model with midsection cut along the XY plane for a) the rectangular block model; b) the blade model. | 67 |
| Figure 4.3 – Stress (S22) distribution for the four analyses performed. | 69 |
| Figure 4.4 – Displacement (U2) distribution for the four analyses performed. | 69 |
| Figure 4.5 – Strain (E22) distribution for the four analyses performed. | 70 |
| Figure 4.6 – Stress (S22) distribution after 10 PDL-FNC flight cycles. | 71 |
| Figure 4.7 – Displacement (U2) distribution after 10 PDL-FNC flight cycles. | 71 |
| Figure 4.8 – Strain (E22) distribution after 10 PDL-FNC flight cycles. | 72 |
| Figure 4.9 – Stress (S22) distribution after 5 PDL-FNC flight cycles. | 72 |
| Figure 4.10 – Displacement (U2) distribution after 5 PDL-FNC flight cycles. | 73 |
| Figure 4.11 – Strain (E22) distribution after 5 PDL-FNC flight cycles. | 73 |
| Figure 4.12 – Vertical displacement (U2) variation in meters of Node 204 for a) 10 cycles; b) 50 cycles. | 74 |
| Figure 4.13 – Stress (S22) distribution after 50 PDL-FNC flight cycles. | 75 |
| Figure 4.14 – Displacement (U2) distribution after 50 PDL-FNC flight cycles. | 75 |
| Figure 4.15 – Strain (E22) distribution after 50 PDL-FNC flight cycles. | 76 |
| Figure 4.16 – Von Mises Stress (S_{VM}) distribution after 50 PDL-FNC flight cycles. | 76 |
| Figure 4.17 – Comparison between three different flight routes after 50 cycles. | 77 |
| Figure A1 – Temperature distribution at 10 seconds for a) rectangular block model; b) blade model. | A5 |
| Figure A2 – Temperature distribution at 25 seconds for a) rectangular block model; b) blade model. | A5 |
| Figure A3 – Temperature distribution for a) rectangular block model at 525 s; b) blade model at 535 s. | A5 |
| Figure A4 – Temperature distribution for a) rectangular block model at 1025 s; b) blade model at 1035 s. | A6 |
| Figure A5 – Temperature distribution for a) rectangular block model at 1775 s; b) blade model at 1785 s. | A6 |
| Figure A6 – Temperature distribution for a) rectangular block model at 5275 s; b) blade model at 5285 s. | A6 |
| Figure A7 – Temperature distribution for a) rectangular block model at 5525 s; b) blade model at 5235 s. | A7 |
| Figure A8 – Temperature distribution for a) rectangular block model at 5775 s; b) blade model at 5785 s. | A7 |
| Figure A9 – Temperature distribution for a) rectangular block model at 7775 s; b) blade model at 7785 s. | A7 |
| Figure A10 – Temperature distribution in the thermal model during the cooling period for instant a) 7885 s; b) 7985 s; c) 8050 s. | A8 |
| Figure A11 - Stress (S11) distribution after 50 PDL-FNC flight cycles. | A9 |

| | |
|--|-----|
| Figure A12 - Stress (S12) distribution after 50 PDL-FNC flight cycles. | A9 |
| Figure A13 - Stress (S13) distribution after 50 PDL-FNC flight cycles. | A10 |
| Figure A14 - Stress (S23) distribution after 50 PDL-FNC flight cycles. | A10 |
| Figure A15 - Stress (S33) distribution after 50 PDL-FNC flight cycles. | A11 |
| Figure A16 - Strain (E11) distribution after 50 PDL-FNC flight cycles. | A11 |
| Figure A17 - Strain (E12) distribution after 50 PDL-FNC flight cycles. | A12 |
| Figure A18 - Strain (E13) distribution after 50 PDL-FNC flight cycles. | A12 |
| Figure A19 - Strain (E23) distribution after 50 PDL-FNC flight cycles. | A13 |
| Figure A20 - Strain (E33) distribution after 50 PDL-FNC flight cycles. | A13 |
| Figure A21 - Displacement (U1) distribution after 50 PDL-FNC flight cycles. | A14 |
| Figure A22 - Displacement (U3) distribution after 50 PDL-FNC flight cycles. | A14 |

List of Symbols

| | |
|-------------|--|
| b | Rotation Axis Midpoint Reference Dimension |
| C_p | Specific Heat Capacity |
| E | Young's Modulus |
| e | Elongation |
| E_{22} | Vertical Strain Component |
| G | Shear Modulus |
| h_1 | Enthalpy of State 1 |
| h_2 | Enthalpy of State 2 |
| h_3 | Enthalpy of State 3 |
| h_4 | Enthalpy of State 4 |
| h_{4a} | Enthalpy of State 4a |
| h_5 | Enthalpy of State 5 |
| k | Thermal Conductivity |
| K_1 | Temperature Dependent Material Constant |
| K_2 | Material Constant |
| l | HPT Blade's base width |
| \dot{m}_a | Air Mass Flow Rate |
| \dot{m}_f | Fuel Mass Flow Rate |
| m_{HPT} | Mass of HPT Blade |
| m_s | Mass of Submerged HPT Blade |
| N | Number of HPT Blades |
| n | Creep Stress Exponent |
| P | Outer Perimeter of HPT Disk |
| $Q_{2,3}$ | Heat Added to System |
| Q_c | Activation Energy for Creep |
| r | Radius of HPT Disk |
| R | Ideal Gas Constant |
| s | Seconds |
| r_p | Pressure Ratio |
| S_{22} | Vertical Stress Component |
| S_{VM} | Von Mises Stress |
| T | Temperature |
| T_{amb} | Ambient Temperature |
| T_f | Firing Temperature |
| T_m | Melting Point Temperature |
| U_2 | Vertical Displacement Component |
| V | Volume of Displaced Water/HPT Blade |

| | |
|-----------|-------------------------------|
| W_a | Split-shaft Cycle Output Work |
| W_C | Work of Compressor |
| W_{ca} | Work of High Pressure Turbine |
| W_{cyc} | Total Work Output |
| W_t | Work of Turbine |

Greek

| | |
|--------------------|--|
| α | Mean Thermal Expansion Coefficient |
| γ | Specific Heat Ratio |
| ϵ_{pl} | Plastic Strain |
| $\dot{\epsilon}_S$ | Creep Strain Rate |
| ν | Poisson's Ratio |
| ρ | Density |
| ρ_{HPT} | Density of HPT Blade |
| ρ_{H2O} | Density of Pure Water |
| σ | Stress |
| $\sigma_{0.2}$ | 0.2% Proof Stress |
| σ_{UTS} | Ultimate Tensile Stress |
| τ | Rupture Life |
| ω_{HPT} | HPT Rotation Speed in Radians Per Second |
| γ | Gamma Matrix |
| γ' | Gamma Prime |
| γ'' | Gamma Double Prime |
| η_c | Compressor Efficiency |
| η_{cyc} | Overall Efficiency |
| η_{ideal} | Ideal Cycle Efficiency |
| η_t | Turbine Efficiency |

Abbreviations

| | |
|------------|--------------------------------|
| BCT | Body Centered Tetragonal |
| CAE | Complete Abaqus Environment |
| EDS | Energy Dispersive Spectroscopy |
| FCC | Face Centered Cubic |
| FDR | Flight Data Record |
| FEM | Finite Element Method |
| FOD | Foreign Object Damage |
| GCP | Geometrically Close-Packed |
| HCF | High Cycle Fatigue |

| | |
|-------------|---|
| HP | High Pressure |
| HPT | High Pressure Turbine |
| IATA | International Air Transport Association |
| IBR | Integrated Blade Rotors |
| ITT | Inter Turbine Temperature |
| LCF | Low Cycle Fatigue |
| LP | Low Pressure |
| NH | High Pressure Turbine Rotation Speed |
| RGB | Reduction Gearbox |
| RPM | Revolutions per Minute |
| SEM | Scanning Electron Microscopy |
| TBC | Thermal Barrier Coatings |
| TCP | Topologically Close-Packed |
| TIT | Turbine Inlet Temperature |
| TMF | Thermo-mechanical Fatigue |
| TRD | Aircraft Delta |
| TRE | Aircraft Echo |
| TRF | Aircraft Foxtrot |
| TRG | Aircraft Golf |
| UTS | Ultimate Tensile Stress |

1. Introduction

In the fields of aviation and power generation, the use of gas turbines is dependent upon the durability and performance of their components. That is so in aviation since the security and safety of passengers and crew relies on the dependability of the engine components. The main concerns for manufacturers, operators and maintenance crews are to ensure not only the best possible performance of the equipment but also the durability and reliability of the components. Different operators and maintenance crews have to adjust their flight operations and schedules in order to both attend to the needs of the public as well as make sure that the reliability and performance of the aircraft engines and their components are not compromised. [1]

Modern gas turbine engines are extremely sophisticated pieces of equipment subjected to many different flight conditions that become increasingly hard to predict due to many different factors such as flight speed, fuel type, atmospheric conditions, foreign objects and particles, and sudden changes in speed, demanding that the manufacturers take in to account as many different combinations of such conditions as possible, in order to ensure the best possible performance, reliability and durability of the engine and its components. [2]

Sometimes, however, commercial demands make it necessary for engines to function beyond the manufacturer's recommendations, and that can create reliability issues and shorten the useful life of certain engine components. This can be the need to use higher speeds for certain portions of the flight cycle or the need to make shorter flight cycles in order to guarantee certain flight paths. Thus, critical sections of the engine will be negatively affected. Critical sections are defined as those whose failure will be considered catastrophic and compromise the entire safety of the aircraft and its passengers. [2]

In these conditions, the most affected critical section will be the hot section, i.e. the combustion section, comprised of the combustion chamber and the high pressure turbine, in which temperatures are the highest in the entire engine. In most modern high-performance gas turbine engines, the turbine inlet temperatures must be raised in order to increase the power output and thermodynamic efficiency [3], thus demanding that the high pressure turbine (HPT) blades operate in an environment where temperatures will typically be well above their materials melting point. In order to maintain mechanical integrity of the blades, cooling has to be applied to the airfoil. [4]

With the goal of studying the life cycle of major engine components, especially for the HPT blades, a regional airline operation was studied. This airline operates within the Azores islands and also provides flights between the island of São Miguel and the island of Madeira, as well as between the latter and the island of Gran Canaria, all these routes within the North Atlantic Ocean. Its fleet is comprised of four Bombardier DHC8-400 airliners, also known as the Dash 8 Q400, for which the PW150A engine studied was especially designed.

The goal of this study was, ultimately, to provide this airline company with a predictive model that would take real in-flight data and, through it, enable the engineers to study the effects of mechanical and thermal loads these blades go through in each flight cycle, and thus predict the creep behavior of the HPT blades for different types of flight routes.

In order to accomplish this, the in-flight conditions that are recorded on the Flight Data Record (FDR) of this airline operation were analyzed. Using that information, Finite Element Method (FEM) simulations were made and the level of creep that these blades suffer was determined. In order to do this, three different cycles with periods of approximately 20 minutes, 1 hour and 2 hours were analyzed. With the cycle modeling defined, several successive cycles could then be applied and a basic trend could be assumed. The difference between each type of cycle period could then be determined and rough predictions on the creep behavior of the HPT blades made for their expected life of 3000 flight hours.

It is hoped that this study is a useful contribution that eventually can enable the airline to better define their flight paths and flight schedules in order to get the best possible performance and durability out of their HPT blades.

2. Background

2.1. Gas Turbine Cycle

Gas turbine engines function as gas generators, capable of accelerating a hot gas flow and then expand it either through a turbine, to generate shaft power, or through a nozzle, to produce thrust. This works through the use of the Brayton Thermal Cycle that extracts chemical energy from a fuel and converts it into mechanical energy using air as the working fluid. [1] [5]

2.1.1. The Brayton Thermal Cycle

In the Brayton Thermal Cycle, as can be seen in **Figure 2.1**, the air at room temperature (state 1) is sucked through a compressor and is compressed to a high pressure (state 2) as fuel is added in a combustor and continuously burnt to a firing temperature (state 3) after which the resulting high-temperature, high-pressure air is expanded through a turbine to atmospheric pressure (state 4). [6]

A simple application of the First Law of Thermodynamics to the air-standard Brayton cycle assumes no changes in kinetic and potential energy, giving us:

- Work of compressor

$$W_C = \dot{m}_a (h_2 - h_1) \quad (2.1)$$

- Work of turbine

$$W_t = (\dot{m}_a + \dot{m}_f)(h_3 - h_4) \quad (2.2)$$

- Total work output

$$W_{cyc} = W_t - W_c \quad (2.3)$$

- Heat added to system

$$Q_{2,3} = (\dot{m}_a + \dot{m}_f)(h_3) - \dot{m}_a h_2 \quad (2.4)$$

- Overall efficiency

$$\eta_{cyc} = W_{cyc}/Q_{2,3} \quad (2.5)$$

In the case of the actual cycle, the effect of the compressor (η_c) and turbine (η_t) efficiencies must be considered as well, giving us the overall efficiency as:

$$\eta_{cycle} = \left(\frac{\eta_t T_f - \frac{T_{amb} r_p^{(\frac{\gamma-1}{\gamma})}}{\eta_c}}{T_f - T_{amb} - T_{amb} \left(\frac{r_p^{(\frac{\gamma-1}{\gamma})} - 1}{\eta_c} \right)} \right) \left(1 - \frac{1}{r_p^{(\frac{\gamma-1}{\gamma})}} \right) \quad (2.6)$$

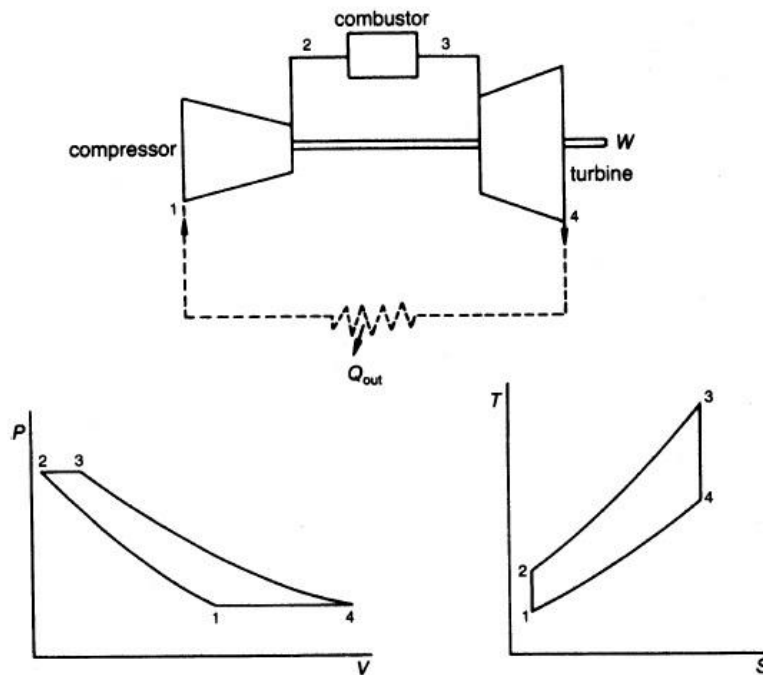


Figure 2.1 – The air-standard Brayton Cycle. [7]

2.1.2. The Split-shaft Simple Cycle

The Split-shaft Cycle is mainly used for high torque and large load variations. As seen in **Figure 2.2**, the first turbine drives the compressor and the second turbine is used as a power source. From the T-S graph we can obtain the relationships between the turbines, giving us:

$$h_{4a} = h_3 - W_{ca} \tag{2.7}$$

$$h_4 = h_3 - (W_{ca}/\eta_t) \tag{2.8}$$

We then get the output work as:

$$W_a = (\dot{m}_a + \dot{m}_f)(h_{4a} - h_5)\eta_t \tag{2.9}$$

Both shafts operate independently and can do so at different speeds. The advantage of this cycle is its high torque at low speed, which is convenient for variable mechanical-drive applications but of little to no value for constant full-power operation. [8]

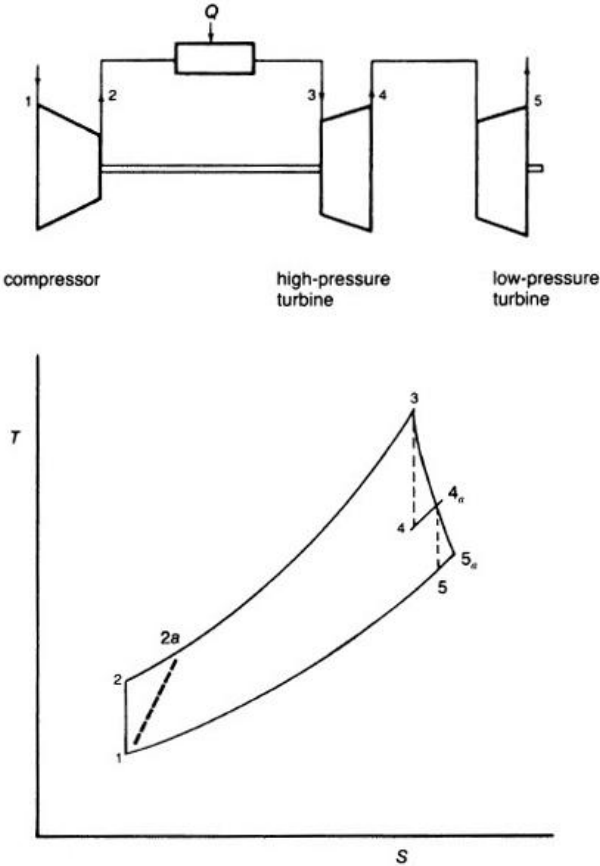


Figure 2.2 – The Split-shaft Simple Cycle. [9]

2.2. Aircraft Gas Turbine Engines

For most aircraft using gas turbine engines, the working principle is basically the same for all the three major types of engine. The gas turbine is basically divided in three sections, a compressor section at the front of the engine that draws in the air and compresses it, a combustion section where fuel is added and ignited in order to heat the compressed air, and a turbine section where the power of the air flow is then extracted. All of this occurs according to the principles mentioned in the previous section [5], and the three aforementioned types of engine, the turbofan, turbojet and turboprop, have only minor differences in the way thrust is achieved. [10]

2.2.1. Turbojet

The most simple of all applications of the gas turbine in aircraft engines, the turbojet is mostly used in high speed aircraft for military applications such as fighter jets. The thrust is achieved by the hot gases generated in the combustion process that escape through an exhaust nozzle. [11]

The compression can be achieved either through a centrifugal compressor driven by the turbine section, that pushes the air outwards, requiring it to be redirected parallel to the axis of thrust, as seen in **Figure 2.3 a)**, or through a multi-stage axial compressor, also driven by the turbine, in which the air flow remains parallel to the axis of thrust, as seen in **Figure 2.3 b)**. [12]

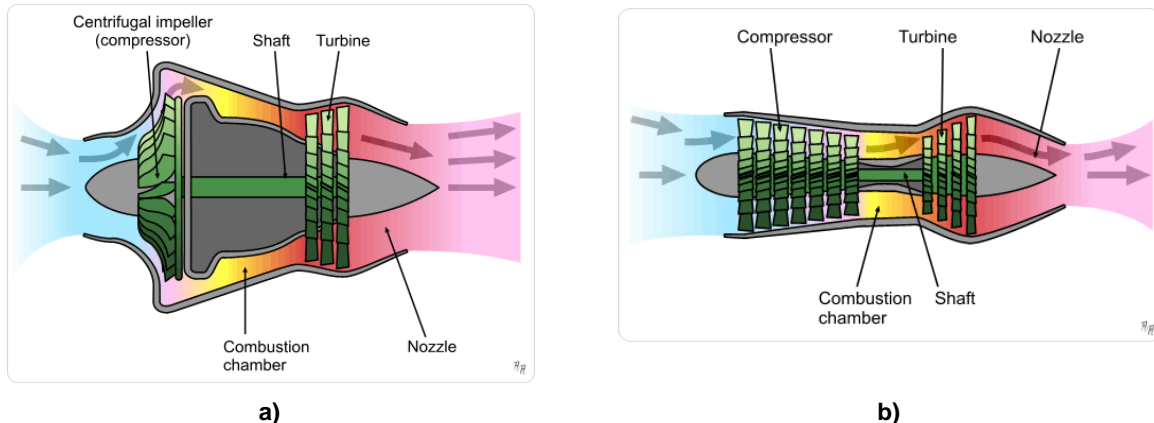


Figure 2.3 – Schematic diagram of a) centrifugal flow turbojet engine; b) axial flow turbojet engine.[13][14]

2.2.2. Turbofan

The most common commercial type of engine in use, the turbofan engine combines the thrust mechanism used in the turbojet with the thrust provided by the fan that acts like a ducted propeller. The relation between both cold and hot airflows is defined by the bypass ratio, where there will be a higher bypass ratio the more cold airflow/less hot airflow (core airflow) is there providing thrust. [15]

Low bypass ratio turbofan engines normally have a multi-stage fan, as seen in **Figure 2.4 a)**, developing a relatively higher pressure ratio and thus yielding a higher exhaust speed (due to the main

airflow being the core airflow). These types of turbofan engines are mostly used in military applications, given that, in some cases, the pressure ratio achieved can be greater than that of turbojet engines. [16][17]

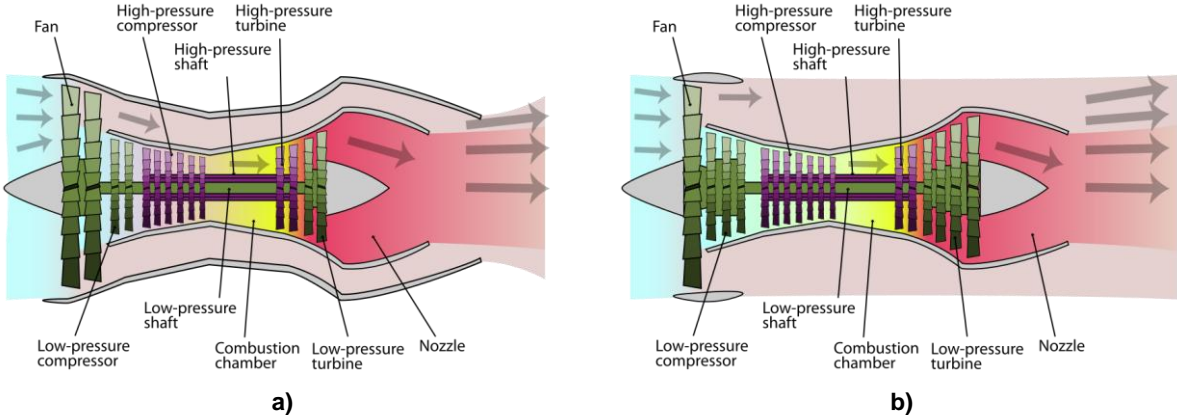


Figure 2.4 – Schematic diagram of a a) 2-spool, low-bypass turbofan engine; b) high-bypass turbofan engine. [18] [19]

To achieve high bypass ratios the multi-stage fan is replaced with a single stage unit and the fan is scaled to achieve the desired mixed thrust, as seen in **Figure 2.4 b)**. Although the bypass airflow (cold airflow) will move at lower speeds, it will have a large enough volume that it will still produce significant thrust. Since most of the noise is due to the high speed core airflow, the overall speed of these engines will be lower due to the mix of cold and hot airflow, and the noise factor will be much lower, making this type of engine much more suitable for civil aviation and certain military applications. [20]

2.2.3. Turboprop

In turboprop engines, virtually all of the hot gases are expanded through the turbine driving the compressor and the attached propeller, with only a small amount of thrust being created by gas exiting the exhaust nozzle. The propeller is connected to the gas turbine through a reduction gear box that will convert the high RPM and low torque output of the gas turbine into low RPM and high torque output for the propeller, which will thus be responsible for the thrust, as seen in **Figure 2.5**. [21]

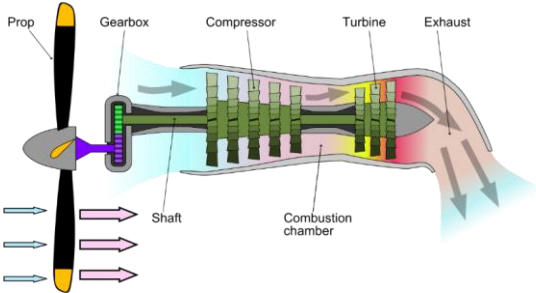


Figure 2.5 – Schematic diagram of a turboprop engine. [22]

2.3. The PW150A Turboprop Engine

2.3.1. Overview

Especially designed for the Bombardier DHC8-400 regional airliner, also called the Dash 8 Q400, the PW150A is a gas turbine turboprop engine with the ability to attain jet-like speeds with the fuel efficiency, low emissions and operating economics typical of turboprop engines. [23]

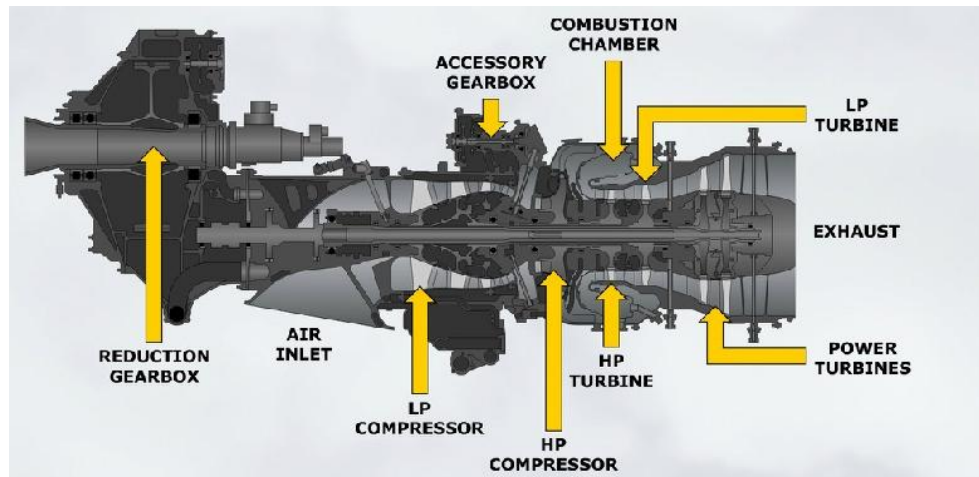


Figure 2.6 – Schematic diagram of the PW150A Turboprop Engine. [24]

In **Figure 2.6**, we can see it is comprised of two modules, the Reduction Gearbox (RGB) Module and the Turbomachinery Module. The RGB is responsible for the reduction of the power turbine input and increase of the torque. The Turbomachinery Module, divided into Air Inlet Section, Compressor Section, Combustion Section and Power Turbine Section, is responsible for generating power that, through the RGB module, will generate rotation of the propeller and the thrust to move the aircraft. [25]

2.3.2. Reduction Gearbox Module

One of the two primary modules of the engine, the RGB, seen in **Figure 2.7**, transmits turbomachinery power to the propeller, reducing the input power turbine speed (17.501 rpm) to one suitable for the output propeller operation (1020 rpm) and also serves as support for the propeller, thus transmitting thrust to the aircraft structure.

The RGB has two housings, rear and front, containing a double-reduction gear-train, respectively, the first and second stage. The first stage reduction gear-train (reduction ratio of 3.92 to 1) gets power from the power turbine shaft that is connected to the RGB input shaft, and the second stage reduction gear-train (reduction ratio of 4.37 to 1) drives the propeller shaft. [26]

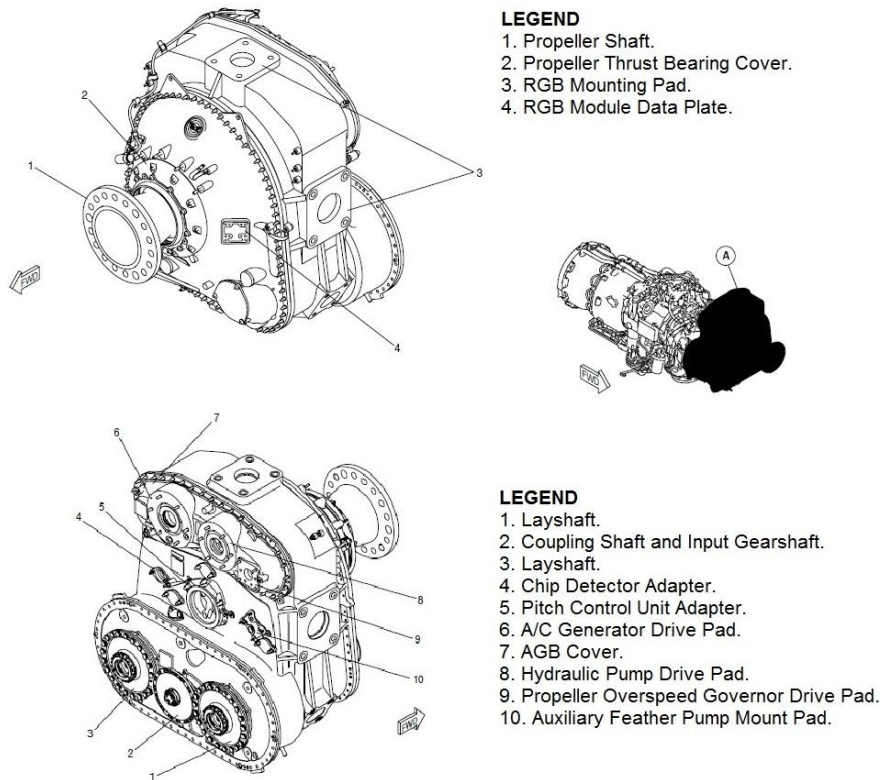


Figure 2.7 – Reduction Gear Box Module. [26]

2.3.3. Turbomachinery Module

The Turbomachinery Module, seen in **Figure 2.8**, contains the axial and centrifugal compressors, combustor, high pressure, low pressure and power turbines, and accessory drives. The axial and centrifugal compressors, and the power turbines are attached to co-axially located shafts which are supported by roller and ball bearings. All these components are contained in the following sections. [25]

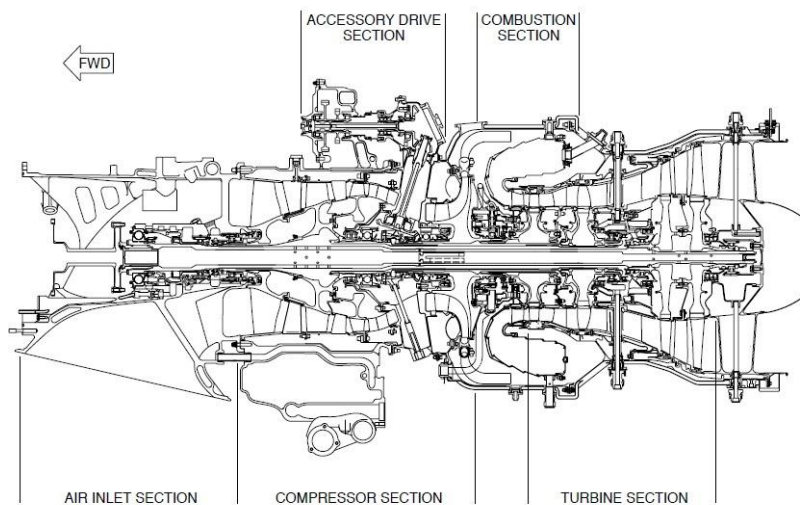


Figure 2.8 – Turbomachinery Module. [25]

- **Air Inlet Section**

Located between the RGB and the Compressor Section, the Air Inlet Case provides air to the engine, through the Compressor Section, under all flight conditions and with as little pressure as possible. Made of magnesium alloy, hot oil flows through internal passages in the case in order to prevent the formation of ice, and it provides structural connection between the RGB and Turbomachinery modules. [27]

- **Compressor Section**

The Compressor Section is responsible for raising the pressure of the incoming air before passing it to the Combustion Section, with a gas path based on an 18 to 1 compression ratio.

It has two independent compressors, the Low Pressure (LP) Compressor, an axial three stage compressor and the High Pressure (HP) Compressor, a centrifugal impeller, each with its own single-stage turbine to make it turn.

At the first three stages of compression (LP compression), a series of axial rotors and stators compress, direct, and diffuse the air. The fourth stage of compression (HP compression) comes from the HP centrifugal impeller, from which the air goes through the diffuser pipes.

The compressed air will then sustain the combustion and give energy to rotate the compressors and power (propeller) sections, as well as providing cooling to the main hot section components and supply bleed air for the aircraft environmental control system (air conditioning and de-icing). [28]

- **Low Pressure Compressor**

The Low Pressure (LP) Compressor is located in the LP Compressor Case, is driven by an independent axial turbine and provides the first three stages of compression to the air mass flowing through the engine.

It is a three stage axial compressor, as seen in **Figure 2.9**, and is comprised of rotor and stator components, all of them carrying blades of airfoil section. The rotor components, attached to rotating disks, are three axial Integrated Blade Rotors (IBR) (1st, 2nd and 3rd stage), all of titanium alloy and Foreign Object Damage (FOD) resistant. They are followed by the stator components, attached to a stationary ring, that are comprised of a 1st and 2nd stage vane assembly in full vane ring cascade, both damped, and a 3rd stage non damped double row cascade. [29]

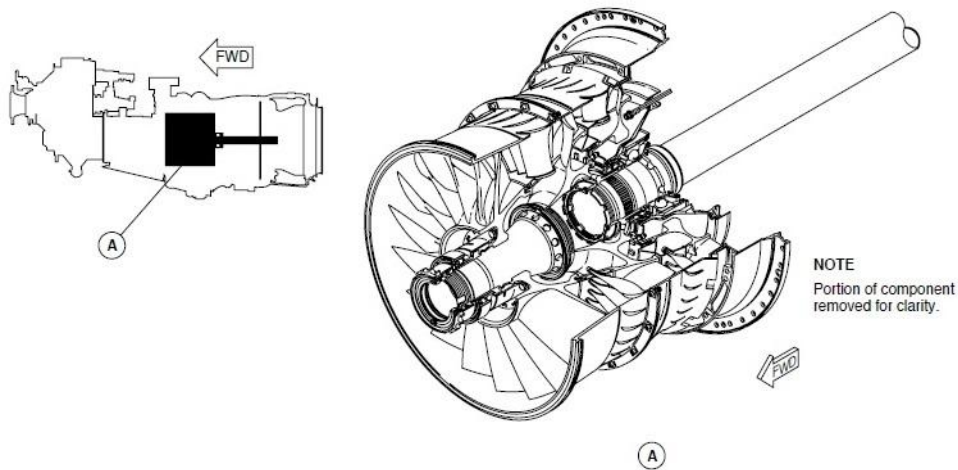


Figure 2.9 – LP Compressor. [29]

The compressor rotor spool is driven by its attached turbine as the rotor blades accelerate the air rearwards and the airflow emerges with an increased velocity due to the rotating movement of the blades, and a higher pressure and temperature caused by the flowing through the divergent passage formed by the rotor. The airflow then passes through the divergent passages formed by the stator blades which convert some of the kinetic energy into pressure energy and directs the airflow onto the next set of rotors at the correct angle that is the most efficient. The airflow emerges from each stage at approximately the same velocity as it entered, but with an increase in pressure and an increase in temperature, as seen in **Figure 2.10**.

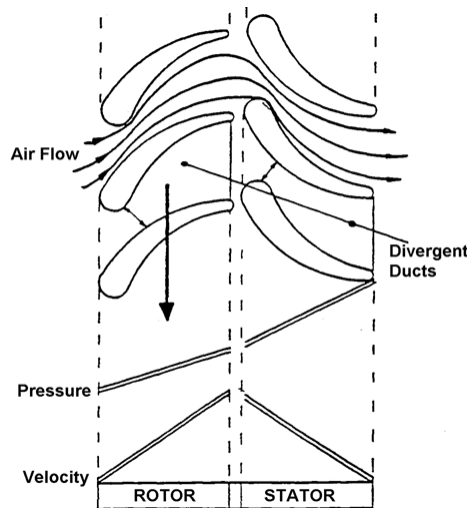


Figure 2.10 – Pressure and velocity during compression axial flow. [30]

The flow path of the blades and vanes within this section has a decreasing cross-sectional area in the direction of flow. This decrease in area reduces the volume of air as compression progresses from stage to stage. As the pressure is built up by successive sets of blades and vanes, the volume required is reduced and, within the compressor, it is gradually decreased as this compression process is repeated for each stage of the axial compressor. [30]

- **High Pressure Compressor**

The High Pressure (HP) Compressor is a centrifugal high pressure impeller located in the Intercompressor Case and driven by an independent axial turbine. It provides the fourth and last stage of compression to the air mass going through the engine. The Intercompressor Case is located between the LP Compressor Case and the gas generator case and forms a path that allows air to flow from the LP Compressor to the HP Compressor.

The HP Compressor, here seen in **Figure 2.11**, is made up of one stage comprising a centrifugal impeller and diffuser pipes. The impeller is the rotating element and the diffuser is the stationary element. The impeller consists of a backing plate or disc with radial vanes attached to the disc from the hub to the outer rim. [31]

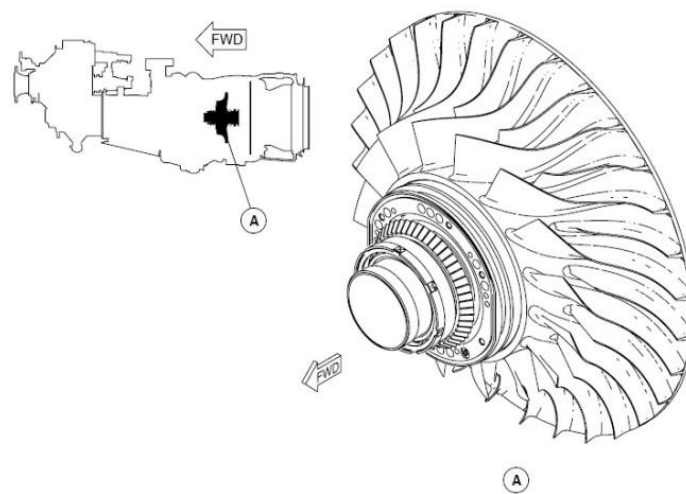


Figure 2.11 – HP Compressor. [31]

The impeller is rotated at high speed by the turbine and air is continuously induced into the center of the impeller, perpendicular to the axis of rotation. The centrifugal action causes the air to flow radially outwards along the vanes to the impeller tip, accelerating the air and also causing a rise in pressure. The air then passes into the diffuser pipes that convert most of the kinetic energy into pressure energy, as seen in **Figure 2.12**. [32]

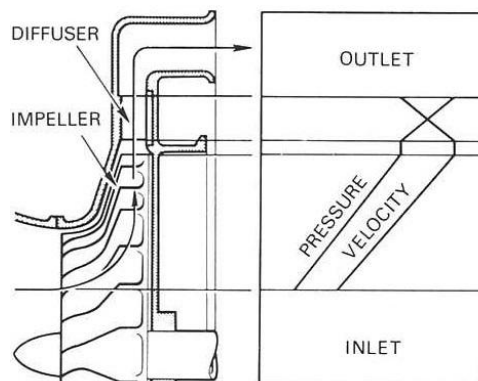


Figure 2.12 – Pressure and velocity during centrifugal flow. [32]

- **Combustion Section**

The combustion section, seen in **Figure 2.13**, provides an area for the combustion of the fuel/air mixture. It contains a Gas Generator Case that is located between the Intercompressor Case and the Turbine Support Case and in the gas generator case there is an annular reverse-flow combustion chamber.

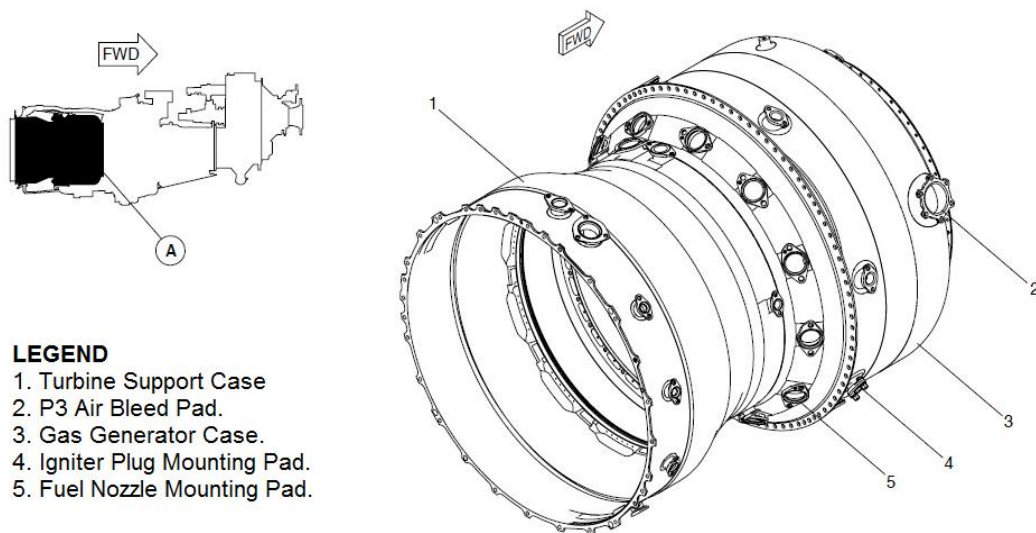


Figure 2.13 – Combustion Section. [33]

The fuel nozzles protrude into the combustion chamber from the rear and two igniter plugs are installed in the Gas Generator Case and come out into the combustion chamber. Fuel is added to the compressed air in the combustion chamber and the igniters are used for starting, but are not required once the fuel/air mixture is lit. [33]

Compressed air from the HP diffuser ducts flows into the Gas Generator Case around the combustion liner, into the dilution holes and through holes in the machined louvers, and the Combustor, seen in **Figure 2.14**, burns a mixture of fuel and air, delivering the resulting gases to the turbines. [34]

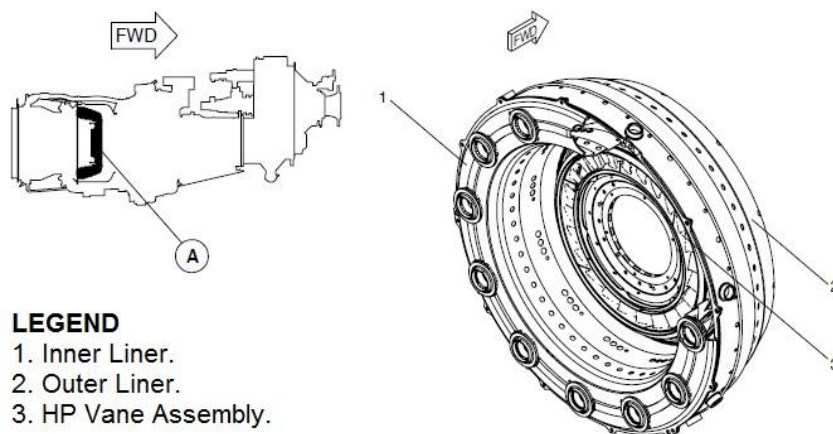


Figure 2.14 – Combustor. [34]

- **Power Turbine Section**

The Power Turbines Section, seen in **Figure 2.15**, consists of the Turbine Support Case, which is located between the Gas Generator Case and the exhaust nozzle. All the turbines are contained in the Turbine Support Case, namely, High Pressure (HP) Turbine, Low Pressure (LP) Turbine and the two-stage Power Turbines. [35]

The turbines extract kinetic energy from the expanding gases as the gases come from the Combustor and then convert this energy into shaft horsepower to drive the compressors and propeller. Hot expanding gases leaving the Combustion Section are directed towards the HP Turbine blades by the HP Turbine ring. After the HP Turbine the hot gases are directed towards the LP Turbine blades by the LP Turbine ring. The gases then travel across the Power Turbine vane rings and impinge on the Power Turbine blades. The LP and HP Turbines turn the LP and HP Compressors through their own respective shafts. The Power Turbines turn the propeller through the Power Turbine shaft and the RGB.

All three shafts are concentric and turn at independent speeds. At engine start, the starter/generator turns only the HP Compressor and HP Turbine. The HP Turbine rotates clockwise (pilot view) to a maximum speed of 31150 rpm (100%), the LP Turbine rotates counterclockwise to a maximum speed of 27000 rpm (100%), and the Power turbine rotates clockwise to a maximum speed of 17501 rpm (100%). [36]

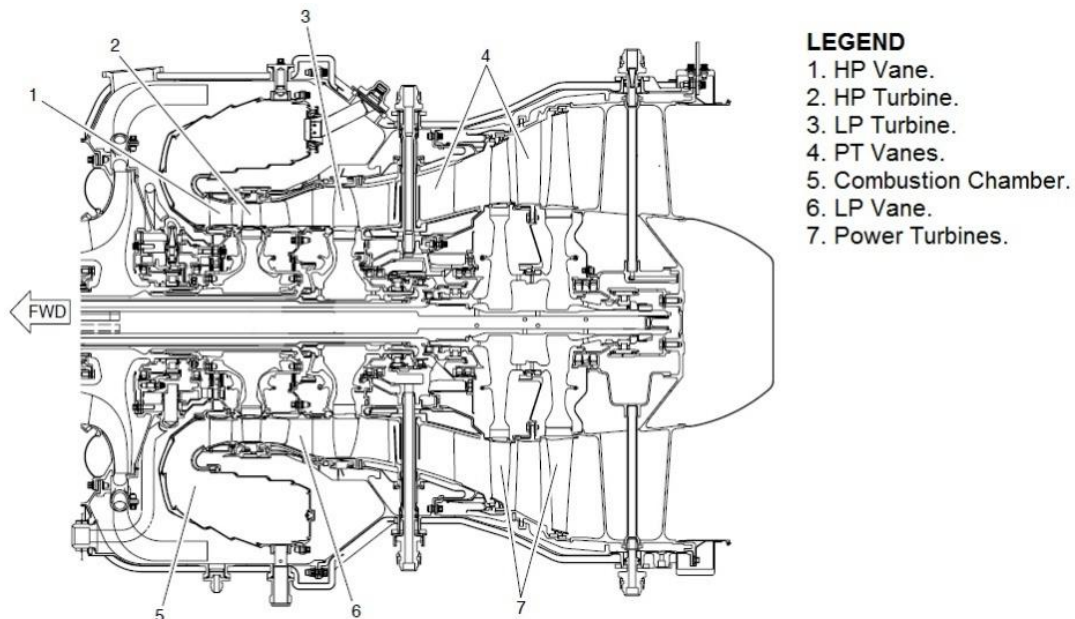


Figure 2.15 – Power Turbine Section. [37]

The Power Turbine Section functions very much like the compressor but with the reverse mechanism of energy transformation. Given the airfoil profile of both the vanes and blades, it is a reaction type turbine, in which the air flows through stationary guide vanes that change its direction and increases its velocity, as the decrease in pressure of the gas is accomplished by the convergent

shape of the passage between the rotating rotor blades. As the air flows across the rotor blades the gaseous energy is converted to mechanical energy with the sacrifice of velocity, temperature and pressure in order to rotate the turbine shaft, as seen in **Figure 2.16**.

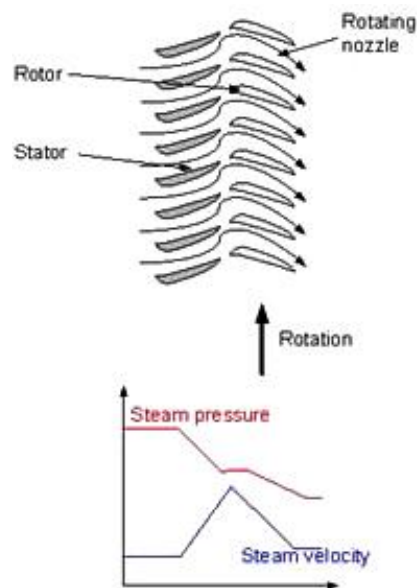


Figure 2.16 – Pressure and velocity in the flow of a reaction turbine. [38]

In the Power Turbine Section the blades and vanes have a gradually increasing span resulting in each stage having an increased flow area when compared to the previous. Thus, the difference in gas velocity is more equal across the whole turbine section since, if the flow area was not increased in this manner, the pressure difference would be across a particular stage, rather than through the whole turbine, resulting in a reduced amount of power recovered. [38]

○ **HP Components**

The HP components are the HP Vane Assembly and the HP Turbine. The purpose of the HP Vane Assembly is to direct the hot gases to the HP Turbine and change static pressure into velocity. It is made of 28 airfoils, seven segments of four airfoils each and the vanes are air-cooled, using showerhead cooling holes. The HP Turbine, shown in **Figure 2.17**, consists of a nickel alloy disc featuring 41 air cooled blades, the base material for the blades is a single-crystal nickel alloy and the cooling air is provided through showerhead, tip and platform cooling holes with trailing edge ejection. [36]

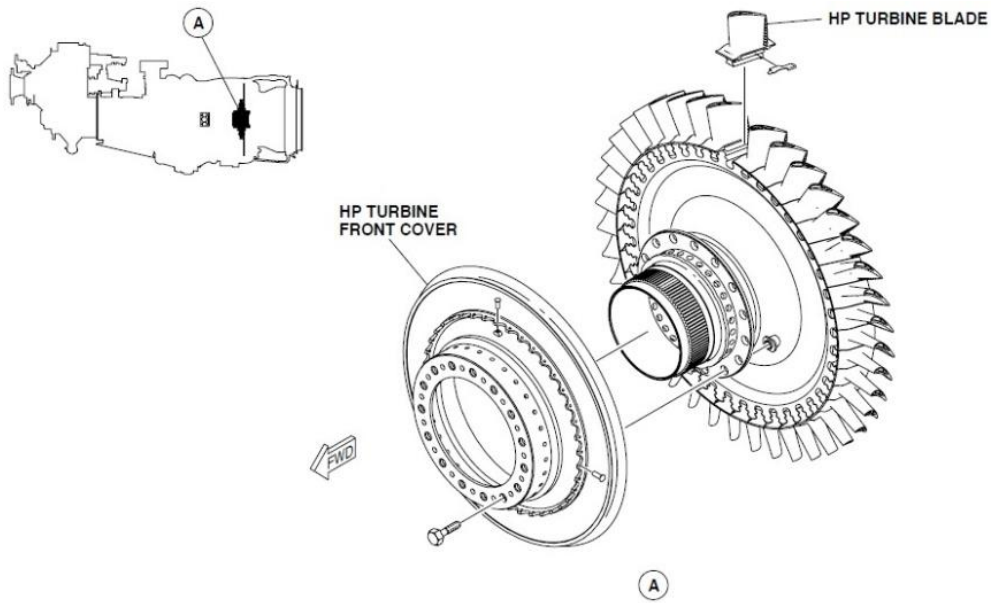


Figure 2.17 – HP Turbine. [39]

○ **LP Components**

The LP components are the LP Vane Assembly and the LP Turbine. The purpose of the LP Vane Assembly is the same stated for the HP Vane Assembly. The vane stage is also made of 28 airfoils, seven segments of four airfoils each, assembled into a squirrel cage outer assembly. The LP Turbine, shown in **Figure 2.18**, is made of nickel alloy and it consists of a disc featuring 41 air-cooled blades, the base material for the blades is a single crystal nickel alloy and the blades use trailing edge ejection for the cooling air. [36]

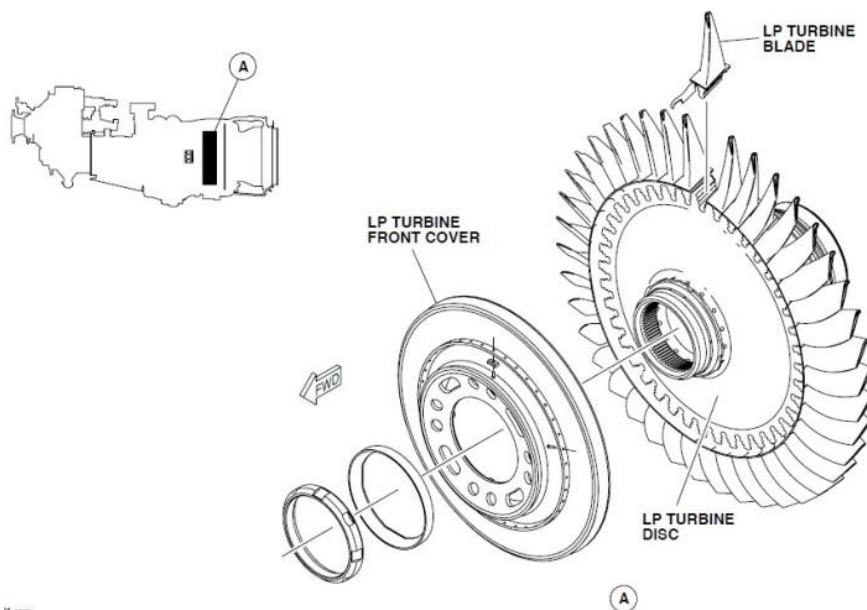


Figure 2.18 – LP Turbine. [40]

- **Power Turbines**

The purpose of the two-stage Power Turbines, shown in **Figure 2.19**, is to extract energy from the hot gases to turn the propeller through the RGB. The turbines consist of discs with blades that make up rotor assemblies, with a vane assembly mounted between the rotors. The rotor assemblies consist of 72 uncooled, shrouded blades secured to a disc through fir-tree serrations and rivets. The first stage blades are single crystal Nickel alloy and the second stage blades are Inconel alloy. Each disc is installed and removed separately thus making assembly and disassembly of the Power Turbine Section easier. [36]

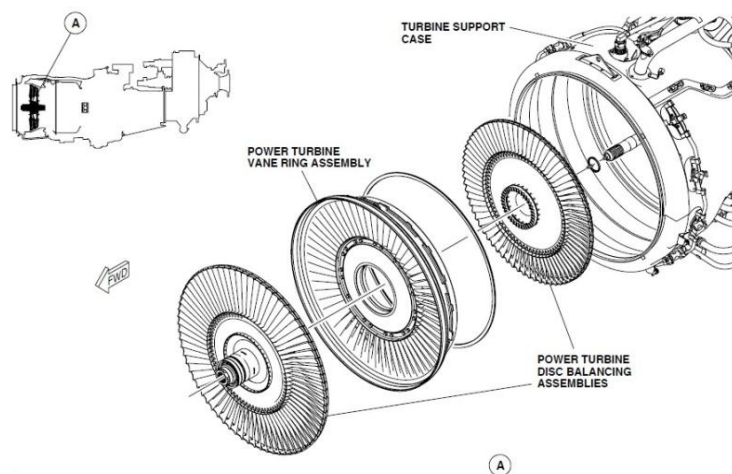


Figure 2.19 – Power Turbines. [41]

2.4. High Pressure Turbine (HPT) Blade

In most aircraft engine operations, the thermally most affected area is the hot section of the engine, i.e. the Combustion Section and the HP Turbine right after it, as can be seen in **Figure 2.21**.

Thus, the High Pressure Turbine (HPT) blades, an example of which can be seen in **Figure 2.20**, when compared to other hardware in the engine, are seen as one of the most important and sensitive components of the engine and the effects of the thermal and mechanical loads they endure on its overall performance and durability are of the utmost importance. [42]



Figure 2.20 – Example of an HPT blade. [43]

2.4.1. Function of HPT Blades

As seen above, the HPT blades are located in the Power Turbine Section, right after the Combustion Section, and are used to extract power from the exiting hot gas flow in order to, in this case, power the HP Compressor.

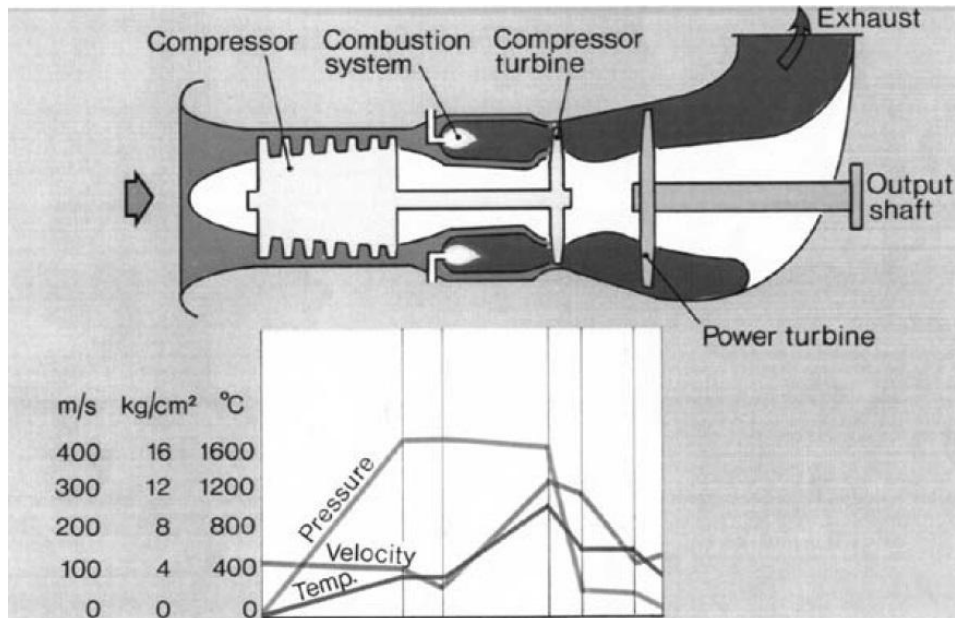


Figure 2.21 – Typical pressure, temperature and velocity profiles in a gas turbine engine. [44]

The turbine blades face the most aggressive conditions inside the engine, however, as with all other components, they must provide efficient performance, with minimal overhaul and repair costs. Thus, these blades are required to withstand not only the high pressure loads from the gas flow, as well as the mechanical centrifugal loads from their own rotation, but more importantly, the extremely high temperatures (the highest in the entire engine) of the gases exiting the Combustion Section and the thermal cycling derived by the nature of their operation. [4] [42]

With the increase, over the years, of the Turbine Inlet Temperatures (TIT) engines are able to achieve, demanded by the need of higher performances, since higher combustion temperatures will provide more efficiency to the engine, the development of the HPT blades has driven them to be as light, strong, durable and heat resistant as possible. These blades not only have to rotate at great speeds (31150 rpm at 100%, for the particular case of this study) [36] but also withstand temperatures of well above 920°C (maximum allowed transient ITT of 20 s during engine start). [45]

Depending on the engine, environment and operator, HPT blades will have variable hours of service before being replaced in the engine overhauls. In this particular case study, the original HPT blades averaged at between 1500 and 2000 hours of service, and the ones under study, their replacements, are expected to last twice as much.

Although the materials used, in most cases and also in this case, nickel based alloys, are made to be heat resistant, the extremely high temperatures in the engine will be well above the melting point of these materials and thus create the need for cooling mechanisms for the HPT blades. [4] [46]

The different conditions these blades have to endure also will either provide stresses that may accelerate the growth of cracks and other defects on the blade geometry or material, as well as exacerbate the effect of other damaging and wear inducing modes of degradation.

All these issues will be addressed in the next sections.

2.4.2. Common Failure Mechanisms

As with all parts of a machine, HPT blades have a finite lifespan, given the many degradation modes that, due to the aggressive conditions they operate under, will no doubt occur, deteriorating the material and compromising the usefulness of the part, making them one of the most replaced components in gas turbine engines overhauls.

These blades ability to withstand and resist the different types of degradation modes and failure mechanisms will therefore be a function of their material properties, design and operating environment, which are fixed by the engine's design and application and thus cannot be affected by the way the engine is maintained and operated. External factors may also affect the engines life consumption, such as manufacturing and material defects, build and maintenance errors, FOD and limit exceedances, all of which can, however, be reduced during maintenance, operation and engine manufacture, although this is quite difficult to achieve.

For HPT blades, the main damage will be caused by ingested materials, temperature of operation and, on rare occasions, mechanical mechanisms such as fatigue. [46] [47] [48] [49] [50]

- **Mechanical Fatigue**

As is to be expected from the demands of the aircraft operation, the HPT blades are subjected to applied stresses that are far from being steady, as loads tend to fluctuate in a random manner. Thus, mechanical fatigue is the process of crack initiation and growth (**Figure 2.22**) resulting from conditions of cyclic stress in which failure will occur at lower levels of stress than would be expected, when steady state loading is applied, and is one of the failure mechanisms that need to be taken into account when regarding this piece of hardware.

The fatigue life of the HPT blade will then be dependent upon and sensitive to a series of factors, ranging from choice of material, magnitude of the mean and cyclic stresses, materials production and processing, changes in grain size, alloying and non-metallic inclusions, random stress fluctuations, stress concentrations, surface finish, residual stresses and corrosive environments.

There are two types of mechanical fatigue that may be the cause of retirement of HPT blades, i.e. Low Cycle Fatigue (LCF) and High Cycle Fatigue (HCF). LCF will lead to failure in less than 10^5 cycles and HCF will do so after more than 10^7 cycles. It is important to note that rather than the number of times the cyclic load is applied, it is the amount of damage accumulated during each application of the load that will matter the most. This is because the differentiating factor between LCF and HCF will be the driver of the cyclic load, i.e. LCF will be mainly driven by pilot demands and

application of large loads and HCF will be driven mostly by sources of vibration and application of small loads.

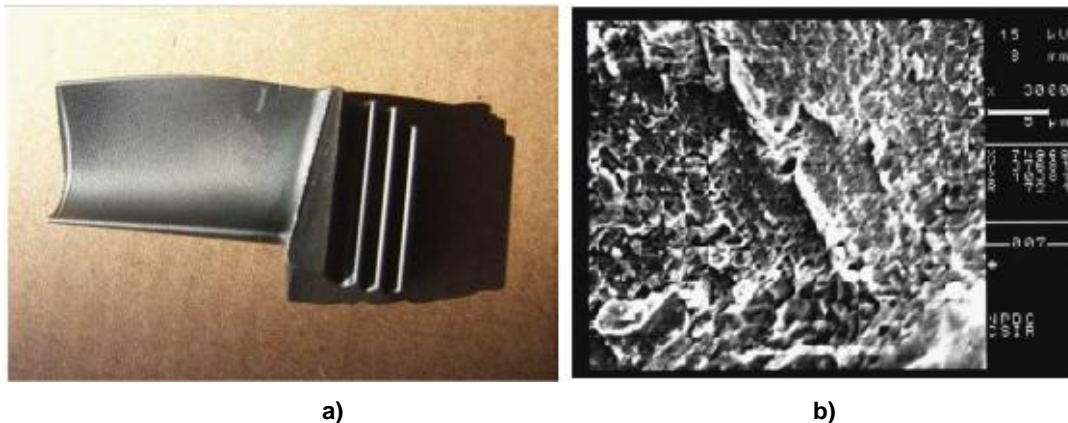


Figure 2.22 – a) Fatigue cracking found in trailing edge of blade (right of pencil mark); b) SEM image of crack surface showing striations. [47]

- **HCF**

As stated above, HCF will be caused by vibrations resulting from the application of small, high frequency, cyclic loads, in the case of the HPT blades, the rotation cycles they go through, e.g. blades rotating at 31150 rpm will equate to 1.86×10^6 cycles per operating hour, and will primarily be a function of the engine design.

By the definition of HCF, it would be expected that the HPT blades wouldn't last beyond two operating hours. However, modern gas turbine engines have had HCF virtually eliminated at the design stage, and without external initiation, it is the rarest of failure modes in HPT blades, although some HCF inducing mechanisms may be the cause of the rare instances in which it does occur.

Mistune or out of balance rotating components, engine configuration, i.e. the presence of upstream and downstream obstructions in the gas path that create perturbations in the flow, FOD or other geometrical damage, all may change the vibration characteristics of the component that can induce HCF, especially when it is compounded with LCF induced cracks. Under these conditions, components vibrate with high frequencies that can reach thousands of cycles per second, and hence exhaust its fatigue life after a short period of time.

- **LCF**

On the other hand, LCF is driven by much greater amplitude stress cycles with low frequency at the engine start up and shutdowns, as the HPT blades are subjected to fairly large centrifugal forces imposed by the rotational speed and are subjected to extremely high temperatures very quickly, the accumulated strain energy per reversal is much higher. This means that under such high loading, the plastic deformation around a concentration feature, such as a notch or scratch, where the LCF cracks are developed, will redistribute the stress to less damaging amplitude and leave the part under

residual compressive stress while it is stationary. This means that the component spends most of its life in the secondary, crack propagation phase of fatigue failure.

The LCF in gas turbines is thus characterized as loading cycles caused by variations on rotational speed, temperature distribution in the HPT blade and internal pressure in the engine, all due to throttle inputs.

- **Thermo-mechanical Fatigue (TMF)**

Closely connected to LCF, Thermo-mechanical Fatigue (TMF) failure is caused by the same loads that induce LCF as well as the cyclic thermal gradients that induce compressive and tensile cyclic loads, especially in the cooled HPT blades.

The same centrifugal forces and high temperatures mentioned above, are imposed very quickly when the engine is started up, which induces high levels of thermal stress, that are reduced when steady state is achieved and re-appear in reverse upon cool-down, making the blades go through a stress sequence with each change in temperature.

Using the example of an uncooled HPT blade, the quick rise in temperature upon engine start-up will heat the HPT blade's outer surface while taking much longer to heat its core, leading to excessive compressive forces and to plastic deformation of the material as a means to relieve the stress. Upon achieving steady state temperature in the core, the surface will experience tension due to the previous deformation and the centrifugal loads acting on the HPT blade. With the reduction of these centrifugal forces and surface temperature, the core's temperature reduction will be slower, causing contractions on the outer surface, which are opposed by the core, thus creating tension on the blade's surface, that remain even after shutdown and that affect the thinner sections of the blade, e. g. the leading and trailing edges, where the temperature gradients are quicker.

- **Creep**

Due to the fact that HPT blades operate at extremely high temperatures and great stresses, creep (**Figure 2.23 a**) becomes a natural consequence, being ultimately the life-limiting process for most of the blades exposed.

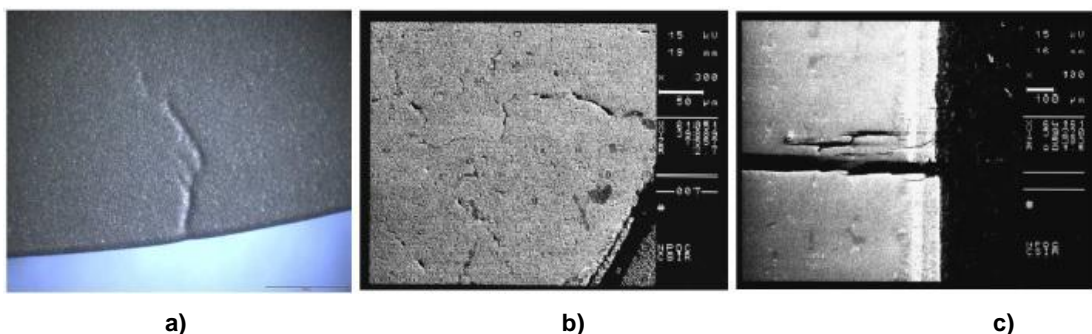


Figure 2.23 – a) Creep damage; b) Grain boundary separation; c) Appearance of creep cracking in a directionally solidified blade material. [47]

Creep is a time-dependent inelastic deformation of both metals and alloys and it occurs when these materials are under stress and subjected to temperatures typically above half of their melting point, leading to permanent deformation, i. e. the blades elongate in service, sometimes severely enough, although it is very rare, for their tips to contact with the non-rotating casing, making the replacement of both parts necessary, or the formation of voids (**Figure 2.23 b**) that may lead to either small cracks (**Figure 2.23 c**) or to the blade cracking right in half, an effect called stress rupture, an even rarer event, as creep in HPT blades is monitored and they are discarded and replaced once the accumulated strain reaches a pre-determined value.

The geometrical and dimensional changes that this mechanism will entice may reduce the aerodynamic efficiency of the turbine and lead to other failure modes by creating mechanisms inductive of vibration or fatigue.

The relationship between creep and fatigue mechanisms will be discussed later on.

- **Oxidation and Corrosion**

Operating in the hot section of the engine, HPT blades are subjected to the most aggressive environments, with extremely corrosive and oxidizing conditions. The air ingested usually contains sodium and chloride, mostly in the form of salt from marine environments, as well as sulfur, originated through pollution from industry, forest fires, volcanic activity and marine environments as well. Also, as a product of the gaseous combustion of the fuel, vanadium or even lead and bromine may be found.

These contaminants will attack the HPT blade's nickel based alloy at high temperatures (**Figure 2.24**) causing loss of material that can weaken the blade to a degree that it may fail under normal loading, due to its effect as a driver for both HCF and LCF failure, as well as its ability to cause reduction of the aerodynamic efficiency of the blade surface and cause blockages in the cooling passages with the corroded material. Even though corrosion can remove enough material to compromise the part all by itself, the main effect it has is in the compromise of the mechanical integrity of the part before it's even noticeable that corrosion is occurring, mostly through the phenomenon of corrosion fatigue, in which the effects of corrosion diminish the fatigue life of the blade by exacerbating the other mechanisms of fatigue.



Figure 2.24 – Sulphidation attack of a turbine blade. [47]

Oxidation will occur due to the high temperature exposure of the HPT blade's alloy material to oxygen, converting its metals into their oxides. Although the formation of oxide coatings may be beneficial as they reduce the formation of more oxides, these mostly fail to remain adherent, thus inciting the removal of material and exposing the base alloy to more and more oxidation cycles. This is of course detrimental to the blade because, as with corrosion, this will reduce the load bearing area of the part and may lead to premature fracture and damage due to fatigue loadings.

To prevent the effects of both oxidation and corrosion, the HPT blades will be protected with sophisticated coatings that will be further discussed in another section.

- **Erosion**

HPT blades are subjected to high pressured high temperature airflow that may carry hard particles that may cause damage in the form of erosion, as seen in **Figure 2.25**. Different from FOD, which will be discussed later, erosion is distinguished for the fact that each individual damage event can be considered inconsequential in terms of performance loss or reduction of mechanical strength, but if they accumulate in a particular area, their effect will be much more noticeable. This mechanism will mainly be responsible for the removal of material from the blade tips, increasing the tip clearance and thus reducing performance, from the leading edge and from the chord width, which reduces aerodynamic performance.

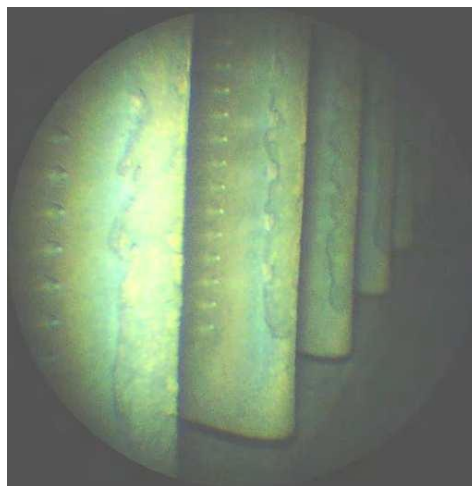


Figure 2.25 – Erosive wear of leading edges of rotor blades. [49]

Although more prevalent in the compressor section, in the case of HPT blades, erosion will be due to particles formed by FOD particles graded in the compressor sections, as these finer particles may be drawn into the cooling system, eroding the internal air-washed passages and creating the glassification of sand particles in the turbine that then block the cooling flows, or due to particles formed by combustion products such as hard carbon, as well as particles of ceramic material used for thermal coatings in the combustor, that are detached due to thermal shock. This mechanism will also be responsible for the removal of the thermal protection in the HPT blades, inducing the corrosion and oxidation mechanisms previously mentioned.

- **External Causes**

Apart from the mentioned mechanisms of failure, external causes may be responsible for component failure, either due to unpredictable modes of failure, such as FOD, manufacturing and material defects, as well as limit exceedances, and maintenance and build errors.

In the case of FOD, its main effect in the HPT blades will be the aforementioned erosion, as seen in **Figure 2.26**, that will occur as a result of the ingestion of the foreign object, be it objects left in intakes during maintenance, bird or ice ingestion, that can happen through many different ways, may it be jet efflux of another aircraft, thrown up by aircraft wheels, high winds, use of reverse thrust or inlet vortices.



Figure 2.26 – Scratches on protective coating conducive to corrosion on the leading edge of a turbine blade. [49]

Material and manufacturing defects are made up of the deviations from the predicted life of components that occur when these are either not compliant with their project drawings, creating a series of problems, e. g. differences in a sections dimension may imply and increase in the stress for a given load, or have poor manufacturing process control, that may create minor alterations in chemical or mechanical composition of the material of the part, altering its strength, fracture toughness and creep resistance; poorly performed surface conditioning, in which the different surface treatments, mostly applied with the goal of inhibiting crack initiation on the surface and extending the parts life, may be overdone, making the surface work hardened and brittle or more prone to cracking; and finally the existence of stress raisers, either inclusions in the metal melt or scratches due to machining, during manufacture, that cause stress contours to deviate from their design orientation, i. e. parallel to the direction of the load, and intensify at the tip of the feature, thus creating a high stress concentration and reducing the fatigue life of the part.

Limit exceedances that will affect the HPT blades will be related to absolute temperature, i. e. any exceedances of a temperature limit will lead to a faster consumption of component life, time at temperature, i. e. the longer the part is subjected to higher than prescribed temperatures, the more likely damage modes are to be engaged, and rotational speeds, i. e. engines are expected to survive

overspeeds to up to 122%, as they are engineered to not exceed such limit lest they incur in loads that will lead to faster consumption of fatigue and or creep life.

Maintenance and build errors will be one of the surest ways to reduce the life of an engine and the HPT blades, for instance either due to incorrect tolerances, incorrect clearances, incorrect torque loading, incorrect assembly or incorrect adjustment, all of these leading to component failure or reduced performance.

2.4.3. Materials

Given that the HPT blades operate at extremely high temperatures, the use of light alloys is not feasible for the engine operation, as they seldom provide the desired creep properties and usually have their melting point well below the operating temperature. Thus, the heavier nickel (Ni) base superalloys are used. [47]

The term “superalloy”, introduced after World War II, describes the groups of alloys developed for use in aircraft turbine engines with the ability to withstand the very aggressive environment of high temperatures and high stress, providing high performances, and the number of applications thus have expanded since then, from land-based and aircraft gas turbines to rocket engines, chemical and petroleum plants. [51]

Nickel is considered the most suitable basis for alloying given that it exhibits a high capacity for forming stable alloys without phase instability and, with chromium (Cr) additions, forms surface oxide films, both stable and protective, that restrict movement of both metallic elements in the outward direction and aggressive atmospheric elements, i. e. oxygen, nitrogen and sulfur, in an inward direction, also forming, with aluminum (Al) additions, surface layers highly oxidant-resistant at very high temperatures. These alloys can be either solid solution or precipitation strengthened, but only the latter is used for the hot sections of gas turbines engines due to its high temperature strength and good corrosion and creep resistance. [52] [53] [54]

- **Microstructure**

Most nickel-based superalloys have their alloying elements vary, i. e. up to 8% aluminum and titanium (Ti), 10-20% chromium, 5-10% cobalt (Co), small amounts of boron (B), zirconium (Zr) and carbon (C), as primary grain boundary elements, as well as molybdenum (Mo), niobium (Nb), tungsten (W), hafnium (Hf), rhenium (Re), ruthenium (Ru) and tantalum (Ta). The aluminum, titanium and tantalum will add strength to the alloy, forming the γ' – phase, as rhenium, tungsten and molybdenum add strengthening to the γ – phase. [51]

The major phases present in these alloys will be the previously mentioned gamma (γ) matrix, gamma prime (γ'), grain boundaries, as well as gamma double prime (γ''), carbides and topologically close-packed (TCP) phases.

a) The Gamma (γ) Matrix - Is a continuous matrix that is a face centered cubic (FCC) nonmagnetic austenitic phase that usually contains a high percentage of solid-solution elements such as cobalt, iron, chromium, molybdenum and tungsten. All nickel-based superalloys contain this phase as the matrix

b) Gamma Prime (γ') – This phase is the primary strengthening phase in nickel-based superalloys. This is a coherently precipitating phase with an ordered FCC crystal structure. This means that the crystal planes of the precipitate are in registry with the gamma matrix. This close match in the matrix/precipitate lattice parameter allows the gamma prime to precipitate homogeneously throughout the matrix and have long lasting stability. Gamma prime is also quite ductile and imparts strength to the matrix without lowering the fracture toughness of the alloy. Aluminum and titanium are major contributors and are added in amounts and mutual proportions to precipitate a high volume fraction in the matrix. This phase is required for high-temperature strength and creep resistance within the superalloy.

c) Gamma Double Prime (γ'') – In this phase nickel and niobium combine in the presence of iron to form body centered tetragonal (BCT), which are coherent with the gamma matrix, while including large mismatch strains. This phase provides very high strength at low intermediate temperatures, but is unstable at temperatures above about 650 °C. [1]

d) Grain Boundaries – A film of gamma prime can be found along the grain boundaries in stronger alloys and is produced by heat treatments and service exposure. This film is believed to improve rupture properties.

e) Carbides – When carbon is added in amounts of about 0.02 – 0.2 wt% it combines with reactive elements such as titanium, tantalum, hafnium and niobium to form metal carbides. During heat treatment and service these metal carbides tend to decompose and generate other carbides which tend to form grain boundaries. Carbides in solid-solutioned alloys may form after extended service exposures. These carbides all have a FCC crystal structure and tend to increase the rupture strength of the alloy at higher temperatures.

f) Topologically close-packed (TCP) type phases – These are plate-like or needle-like phases that are generally undesirable, brittle phases that are formed during heat treatment. The structures of these phases consist of close-packed atoms in layers with relatively large interatomic distances one below the other. The characteristic topology is generated by layers of close packed atoms being displaced from one another by sandwiched larger atoms. The resulting structure is called topologically close-packed (TCP), whereas the gamma prime phase is close-packed in all directions and called geometrically close-packed (GCP). Superalloys containing transition metals such as tantalum, niobium, chromium, tungsten and molybdenum are the most susceptible to the formation of TCP phases. TCP phases tend to cause lowered rupture strength and ductility. [51]

Further analysis of these phases behavior at high temperature will be done in a creep focused chapter.

- **Manufacturing Process**

Nickel-based superalloy HPT blades are built using a process called investment casting, a high precision low surface roughness casting method that uses sand and tetra ethyl silicate as a binding agent. This method is able to produce small parts with extremely complex geometry with very little need of finishing, albeit it is a hard and expensive process, with the need for strict control in all its stages, given that an earlier dimensional error will be increased through all further stages. [52]

The first stage is the production of the die for external shape for the wax pattern and the production of the die for the internal passage ceramic core. The produced parts accuracy is dependent upon the die, which should be preferably metallic, very polished and with great dimensional and shape accuracy. When producing the dies, all contractions and dilations of the materials must be taken into account in all the parts production stages, and their materials will be function of the batch to be produced.

In a second stage, the wax patterns are produced by injection of wax or polystyrene in the die and, for internally cooled parts, the ceramic core is placed inside the wax pattern prior to having the wax injected, and that then encapsulates the ceramic core. The wax should be able to melt at low temperatures, leave no residues on the die, not attack the die in which it is produced nor the coatings it will produce, be mechanically resistant enough as to not to get deformed and accurately reproduce all the die's details.

The third step is the manufacture of destructible tree models for assembly of a number of wax models, with a pouring cup, sprue and risers, avoiding any geometry defects that can cause any compromise of the pouring process.

The fourth stage is the creation of a two layer coating. The first fine grained refractory coating is applied to the destructible tree through the deposition of layers of slurry in one of two ways, either by dipping the model tree into the slurry until it is covered with a layer of sufficient thickness, or by projecting the slurry on the model tree, with a pistol, in order to coat it. After this, sand with a slightly larger grain is either projected with a pistol or by immersion on a fluidized bath, to facilitate the connection of the first layer to the subsequent layer. This first coating must then be dried until it attains enough strength for a second coating to be applied.

The creation of the second coating is made with an identical material to the first coating, with a coarser granulometry in order to provide stiffness, by placing the mold tree inside a box on a vibrating plate, as the sand is then applied and the plate set in motion.

In the fifth stage, the cast is then set in a oven with temperatures between 90 °C and 150 °C, causing the wax to melt and flow into a tray to be later reused, and then placed in a oven at higher temperatures (minimum 800 °C) in between 45 minutes to 2 hours in order to complete the setting process (hardening) of the ceramic material.

The sixth stage is then the casting process, in which the molten metal is poured into the cast, which is still hot in order to avoid thermal tensions and reduce the cooling speed of the produced parts. Strict control of the cooling speed has to exist in order for the desired alloy properties to be attained. This will be discussed in the next section.

After removing the cast shell from the casting furnace, it is then removed in a seventh stage from the raw castings through vibration or water jet.

The eighth stage consists of the removal of all the residual material and cutting of the parts, followed by the ninth stage, where all the finishing operations are done, through the removal of excess casting stock either through grinding, polishing or blasting, and the internal ceramic core for the internal cooling passages is leached out with a caustic solution.

The tenth and final stage of the process is the inspection and quality control of the produced parts to customer standard, through non-destructive means such as visual, radiography, ultrasonic, fluorescent penetration, dimensional gauging, grain etch and x-ray diffraction. [55] [56]

A simple schematic of these operations can be seen in **Figure 2.27**.

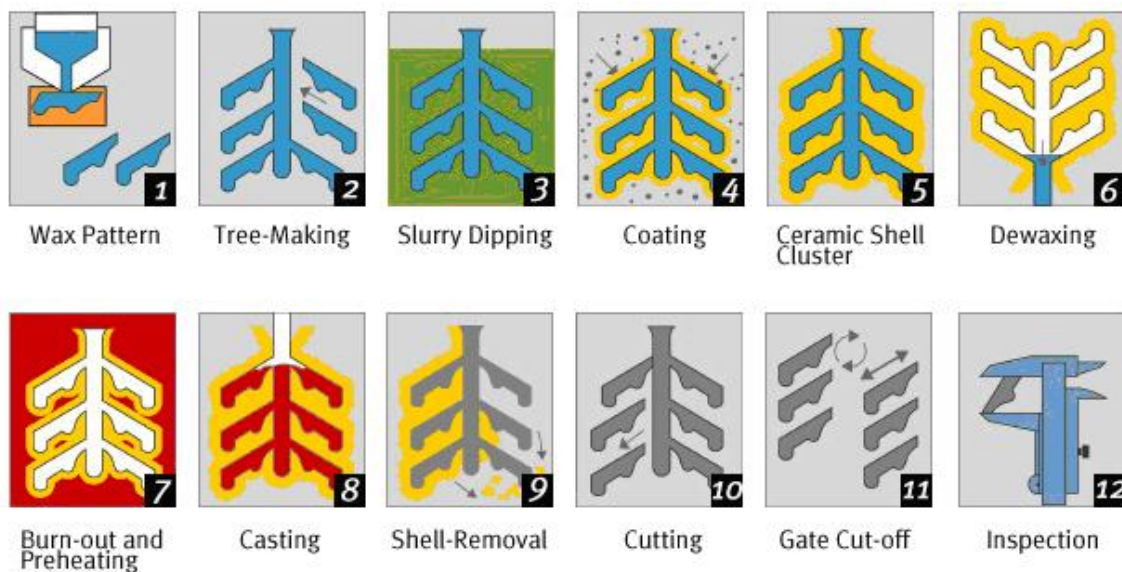


Figure 2.27 – Basic operations of the investment casting process. [55]

- **Grain Structure**

Given that HPT blades are subjected to great stresses generated by the high temperatures, high centrifugal loads and thermal cycling they experience, they need to be made to be resistant to the tendency of these stresses to accelerate the growth of all and any flaws or defects present in the material.

The need to improve on the material properties of creep and rupture strength led to the development of precipitation strengthening, mentioned above. During the solidification in the investment casting process, the critical part of the process, the alloy acquires its crystalline structure, which is a major determinant of the properties of the finished part, as undesirable grain sizes, shapes, and transition areas are responsible for premature cracking of the HPT blades. Thus the equiaxed process was developed to at least assure the uniformity of the grain structure along all their axes. At high temperatures, the part failure starts within and progresses through the grain boundaries instead of within the grains, thus the full strength of the crystal is not being used.

It was concluded that the strength of the alloy could be improved if the grain boundaries were to be aligned along the direction of the centrifugal stress, thus introducing the directional solidification process, although the grain boundaries would still remain the weak link in the HPT blades, and the need to eliminate them became evident.

Thus the single crystal process for the production of HPT blades was developed. In investment casting, the superalloy material is melted in a vacuum furnace before being retracted from the furnace in a controlled direction, as the front edge of the cast is cooled, and columnar grains start to grow parallel to the retraction. Using a helix shaped grain selector, only one grain is allowed to grow radially from the blade root, resulting in a structure with no grain boundaries aligned with the radial centrifugal stresses ($\langle 001 \rangle$ crystal direction). After the casting, the bottom part, the part with the columnar grains and the helix part (also called pigtail) are all removed by machining, as can be seen in **Figure 2.28**. The three different types of grain structures can be seen in **Figure 2.29**. [42] [51] [52] [53]

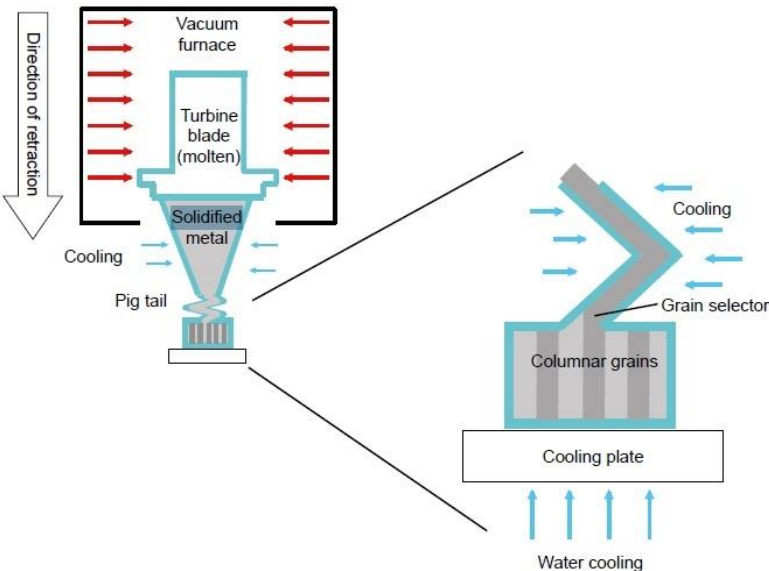


Figure 2.28 – Investment casting of single-crystal turbine blade. [57]

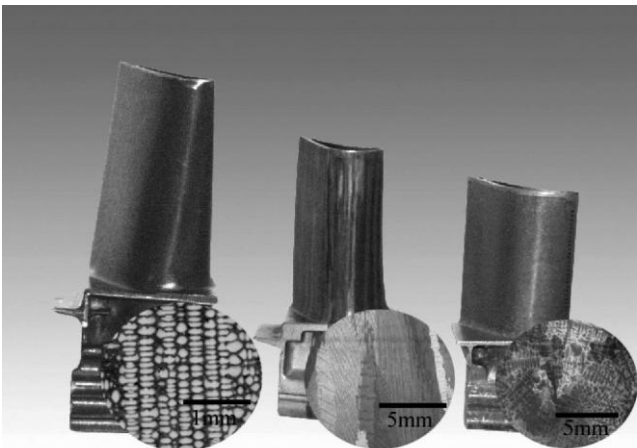


Figure 2.29 – Grain structures of single-crystal, directionally solidified, and conventionally cast turbine blades. [52]

2.4.4. Protection Modes and Cooling Schemes

HPT blades have to withstand extremely harsh working conditions and survive for long operating periods, normally at temperatures above their melting point. Thus, different ways of protecting these blades against both the heat and other damaging mechanisms must be employed, from cooling mechanisms that will help maintain the blade at a suitable working temperature, below their melting point, to coatings that will protect the blade against thermal, corrosion and oxidation damage.

- **Coatings**

Blade coatings are used as protection against corrosion, oxidation and mechanical property degradation, by providing surface elements that will form very protective and adherent oxide layers, thus protecting the underlying base material from attack, as well as from thermal fatigue from cyclic operation and, to a lesser degree, through their ability to withstand damage from light impacts without spalling to an unacceptable extent because of the resulting rise in the local metal temperatures. They also provide extra protection by enduring the operational conditions, thus protecting the blades by allowing the coating to be removed and reapplied on the same base metal.

When considering the “clean fuel” regime, oxidation is the main concern, and protection against it is improved by increasing the amount of aluminum in the outer region of the coating matrix. On the other hand, when considering higher temperatures and not so clean fuel, the main concern is corrosion.

Thus, the coating’s life is dependent upon its composition as it includes environmental and mechanical properties, its thickness, as it will provide better protection if thicker, albeit having lower thermal fatigue resistance as a consequence, and its defined thickness variation and coating defects.

When considering the modern HPT blades, there are three basic types of coatings, i.e. diffusion coatings, plasma sprayed coatings, and thermal barrier coatings. Diffusion coatings are created by enriching the surface layer of the blade with elements that protect against corrosion, mostly comprised of one or a combination of two of the following: aluminum, chromium, titanium, silicon, platinum, with a required thickness between 25-75 μm . The most common is the platinum aluminide (PtAl) coating, with the added platinum increasing the oxidation and corrosion resistance by increasing the activity of the aluminum in the coating, enabling a very protective and adherent Al_2O_3 (aluminide) scale to form on the surface.

Plasma sprayed coatings are mainly comprised of the MCrALY alloy, comprised of M (metal, either nickel or cobalt), about 20% chromium, about 10% aluminum and about 0.5% yttrium (Y). These coatings come in a wide range of compositions, tailored to the type of performance needed and the protection required against prevailing aggressive operational circumstances, usually have a 75-500 μm thickness, and can have other minor element additions such as platinum, hafnium, tantalum and zirconium (Zr), used to improve environmental resistance.

The thermal barrier coatings (TBC) usually have a thickness between 100-300 μm and are partially yttria-stabilized zirconia ceramic coating that can reduce metal temperatures by 50-150 $^{\circ}\text{C}$. Zirconia (ZrO_2) has a coefficient of thermal expansion that matches most turbine alloys, thus offering good thermal insulation, but since it has a phase change between ambient and turbine operating temperatures, it needs to be “alloyed” with about 8% yttria (Y_2O_3), and the coating’s properties can be widely varied through the selection of process parameters, from very dense, thin coatings, to very thick, high insulating coatings with controlled high porosity.

In most HPT blades, a combination of one of the first two types mentioned is applied on the blade surface followed by a second TBC layer, thus creating a coating system that thoroughly protects the blade as desired (**Figure 2.30**). [58] [59] [60]

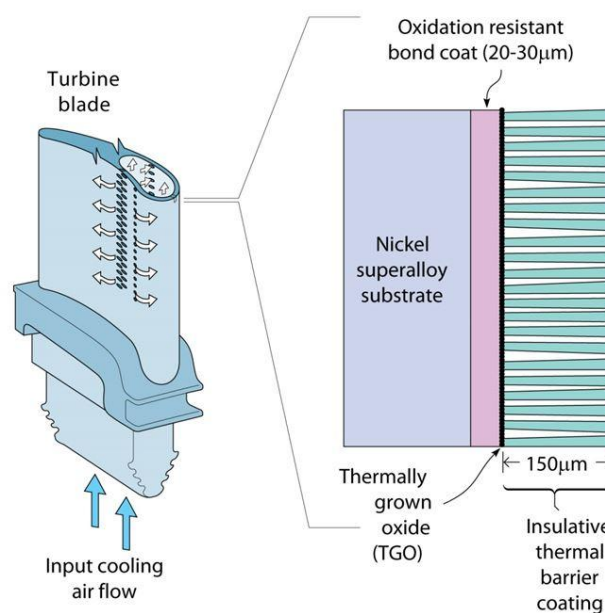


Figure 2.30 – schematic of a thermal barrier coating system. [60]

- **Blade Cooling**

Given that higher turbine inlet temperatures improve upon the thermal efficiency and power output, the HPT blades will be subjected to temperatures well above their alloy’s material melting point and thus, beside the thermal barrier coatings previously mentioned, will require cooling mechanisms in place to keep the material in operating conditions.

For the most part, the current generation of HPT blades uses a combination of cooling techniques as seen in **Figure 2.31**, with cooling air being bled from the compressor as different types of cooling are applied to the three main internal sections of the blade, the leading edge, the mid body and the trailing edge, as well as its surface.

The mid body is cooled through convection cooling, the most widely used cooling concept in present-day gas turbines, where the cooling air flows inside the turbine blade through the zigzagging multi flow cooling passage lined with the rib turbolators cast into the hardware typically on opposite

walls of these cooling passages that enhance the heat transfer, thus removing heat through the walls into the air flow.

For the leading edge, where the temperatures are much higher than in the midsection, the type of cooling technique used is called impingement cooling, an high intensity form of convection cooling in which the cooling air is blasted on the inner surface of the airfoil by high-velocity air jets, letting an higher amount of heat be transferred to the cooling air flow from the metal surface, allowing for the maintenance of more evened out temperatures in the blade surface as a whole.

As for the trailing edge, due to the need to maintain the narrowness of its section for aerodynamic and structural purposes, its opposing walls are connected through a pin-fin arrangement that acts as turbulator in which the impingement cooling flow passes, creating heat transfer much in the same way the rib turbulators act, in which the heat is transferred from both the smooth channel and wall as well as the numerous pins within the passage.

The surface of the blade, on the other hand, is cooled through a method called film cooling, in which the cooling flow passes from the internal cooling passages through a variety of holes, also known as cooling holes, to the external blade surface, forming an insulating layer of “film” between the hot gas stream and the blade walls. This reduces the amount of heat transferred from the main hot gas flow and the HPT blade surface wall given that the temperatures of the cooling air flow are lower than that of the mainstream gas.

All these cooling techniques, however, present a cost to the engine performance, given that the air flow used for cooling is bled from the compressor stages, and as it bypasses the combustor section, thus maintaining a much lower temperature, is removed from the core mass flow and thus is removed from the overall engine thrust. [4] [61] [62]

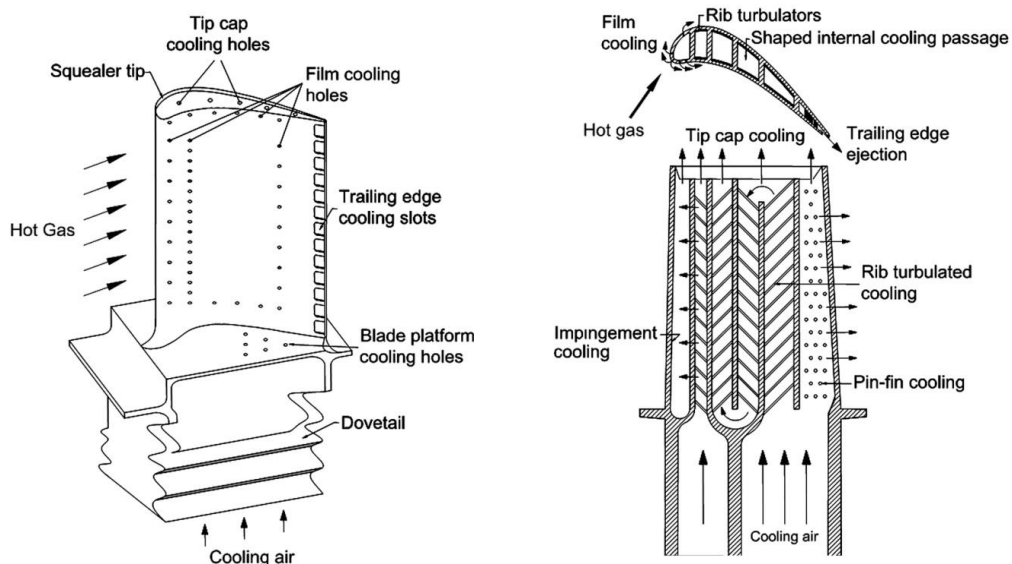


Figure 2.31 – Schematic of a modern gas turbine blade with common cooling techniques. [61]

2.5. Creep in Nickel-base Superalloy HPT Blades

As mentioned earlier, creep is one of the main life-conditioning failure mechanisms that act on HPT blades. When coupled with the effects of cyclic thermal and mechanical loads, the ensuing combination of effects acts as a mix of creep fatigue and TMF.

Given that creep is essentially determined by temperature, time, load acting on the part and its material properties, these factors will incur upon the part a deformation made up of both an elastic deformation and an inelastic, i.e. permanent, deformation, as a result of slipping that occurs in the crystal structure accompanied by flow of the grain boundary layer. [63] [64]

2.5.1. Creep Characteristics

High temperature creep is usually characterized as a function of stress at elevated temperature, expressed as strain vs. time in the creep curve shown in **Figure 2.32**:

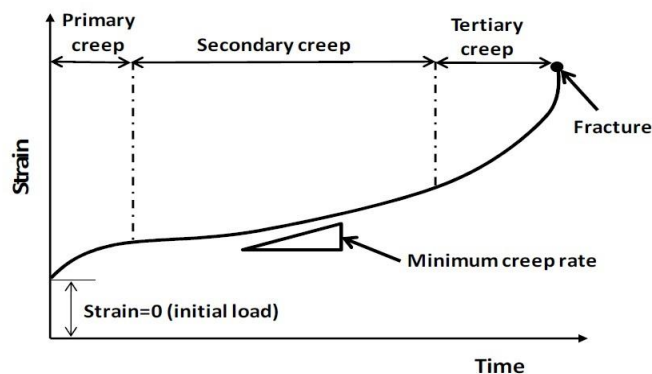


Figure 2.32 – Schematic of a creep curve exhibiting the three stages of creep. [65]

The creep behavior is modeled testing specimens at constant temperature and stress, using stress rupture data to determine the materials time to failure.

In the case of single crystal materials, at relatively low stress and high temperature, an instantaneous elastic and plastic strain upon loading is observed.

Following this first elongation, the first stage, i.e. primary creep is initiated, in which the strain rate decreases rapidly due to the development of dislocation structures within the microstructure, as they build up and material hardening processes tend to dominate, until a constant creep rate is achieved.

The second stage, secondary creep, is defined by the constant creep rate, where the strain rate is at a minimum, due to the establishment of balance between deformation and recovery mechanisms, comprising the longest portion of creep acting on the material, it defines the material's creep rate as a function of stress and temperature.

The third and final stage, tertiary creep, the strain rate increases rapidly due to internal damage accumulation within the material and microstructure, reducing the effective load-bearing cross-

sectional area until fracture or stress rupture occurs. The damage mechanisms in this stage will be addressed later on. [64] [65]

2.5.2. Creep Inducing Factors

As stated above, the main creep driving factors in HPT blades are temperature, stress, time and material properties, with special emphasis on temperature and stress.

In the case of temperature, its increase will lead to an increase of the primary and tertiary creep, thus reducing the duration of the secondary stage of creep, through the increase in the steady state's strain rate, reducing the overall life of the part. At temperatures $T > 0.4 T_m$, where T_m is the melting point temperature, dislocation, due to material diffusion, will be increased given the increase of atom mobility. Diffusion may also occur at lower temperatures, in specific areas, e.g. phase interfaces and grain boundaries.

The stress induced by the applied loads also has an immense effect on the creep rate, as with higher stresses, so will the creep rates be higher, as shown in **Figure 2.33**, in which we can see a reduction of the duration of both first and second stages of creep, as well as an increase in the steady state strain rate for the secondary creep, and a predominant third stage of creep. [64] [65]

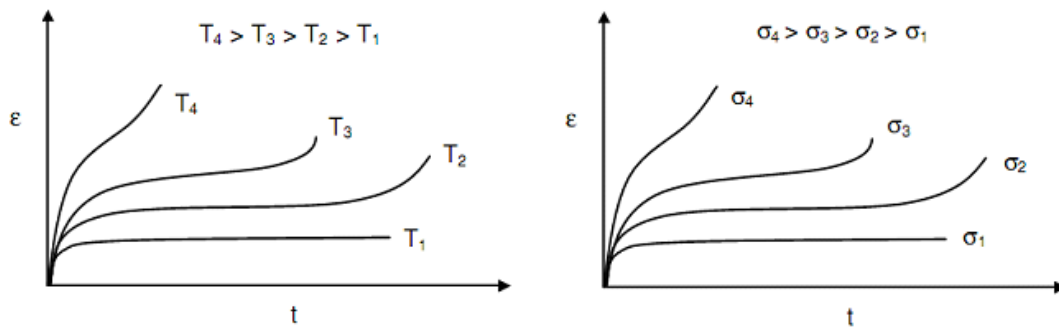


Figure 2.33 – Effect of temperature and stress on creep. [66]

2.5.3. Superalloy Microstructure

Apart from the previously mentioned drivers, in the case of single crystal materials, such as is the case of the nickel-base superalloys, the microstructure will be of great importance, as they are immensely complicated in that regard, with the presence of fine precipitates which provide high levels of resistance to creep. The precipitation of the previously mentioned γ' phase needs to be strictly controlled during the casting process in order to obtain a controlled size and morphology, a fine, ordered quasi-cubic precipitate, in the vicinity of 65% γ' , thus optimizing resistance to both diffusion creep at lower temperatures and power-law creep at higher temperatures.

The main mechanisms of creep damage for the single-crystal nickel-base superalloys will then be the coarsening of the γ/γ' -microstructure, precipitation of the TCP phases and growth of porosity,

which affect not only the creep lifetime of the part, as well as its mechanical properties such as yield stress and LCF life, this latter effect also called creep fatigue. [47] [57] [65] [67]

- **Loss of Coherency and Coarsening**

During primary creep at high temperatures, the main damage mechanisms are loss of interfacial coherency due to matrix glide and rafting of the γ/γ' -microstructure. Exposure to stress at high temperature makes the cubic particles (**Figure 2.34 a**) grow into plate-like rafts, perpendicularly to the applied stress, which results in widening of the γ -channels thus supporting matrix glide. These two processes create a γ/γ' -microstructure where the γ/γ' -interfaces are covered with dense dislocation networks (**Figure 2.34 b**). This rafted structure then results in a degraded performance against diffusion creep. If the exposure continues, the rafted structure further degrades, forming large particles with a quasi-spherical shape, and as the temperature increases, the γ' phase dissolves into the γ continuum and the particle eventually disappears, thus diminishing the overall creep strength of the material and leading to failure of the material.

Once the microstructure has been degraded by the exposure to high temperatures, if it is permitted to remain in service, e.g. the temperature exceedance goes undetected, the dissolved phase will re-precipitate, but, given that the temperature at normal operating conditions is lower than the temperature in the manufacture process, the material will not regain its original creep resistant properties (**Figure 2.34 c**).

When it comes to its effect on LCF, it is known that the occurrence of rafting if perpendicular to the load axis will significantly reduce its life, due to the propagation of fatigue cracks along the extended incoherent γ/γ' -interfaces of the rafts. Another effect of the rafting will be the reduction of the yield stress at low temperatures. [47] [52] [57] [68]

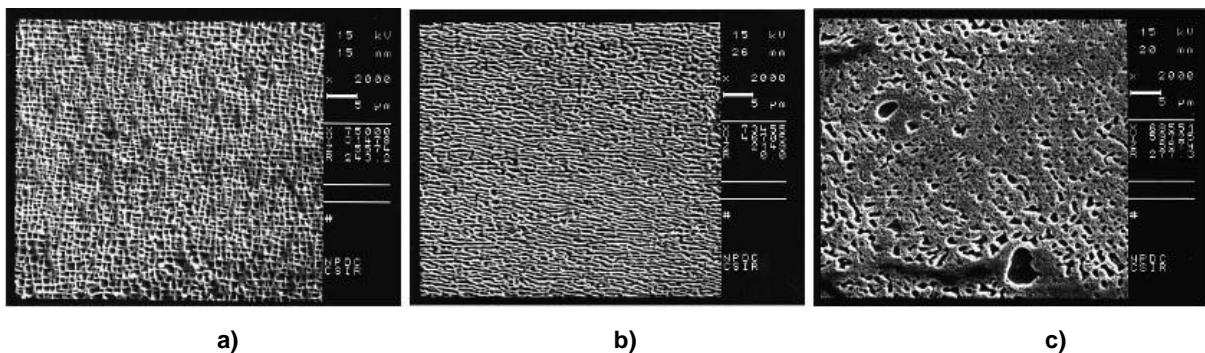


Figure 2.34 – a) Undamaged structure of γ' quasi-cuboids; b) rafted γ' resulting from exposure to stress at high temperature; c) re-precipitated γ' . [47]

- **Growth of Porosity**

Porosity growth is observed at high temperatures during long-term creep, when the diffusion of vacancies is quick and plays an important role in the deformation process. This increase is related to

the enlargement of pre-existing solidification and homogenization pores, along with nucleation of new deformation induced pores, as most of the dislocations move along the γ/γ' -interfaces perpendicular to the load axis and generate vacancies which condense on pores increasing their size or forming new pores (**Figure 2.35 a**). The porosity will grow faster during the first and third stages of creep, when dislocation movement is active, and slower in the second stage, when dislocation mobility is minimal.

The effect of porosity growth in the reduction of LCF life is clear, as it acts as a stress raiser inducing stress concentration near the pores, which results in alternating plastic strains leading to material embrittlement and nucleation of fatigue cracks (**Figure 2.35 b**). [57] [68]

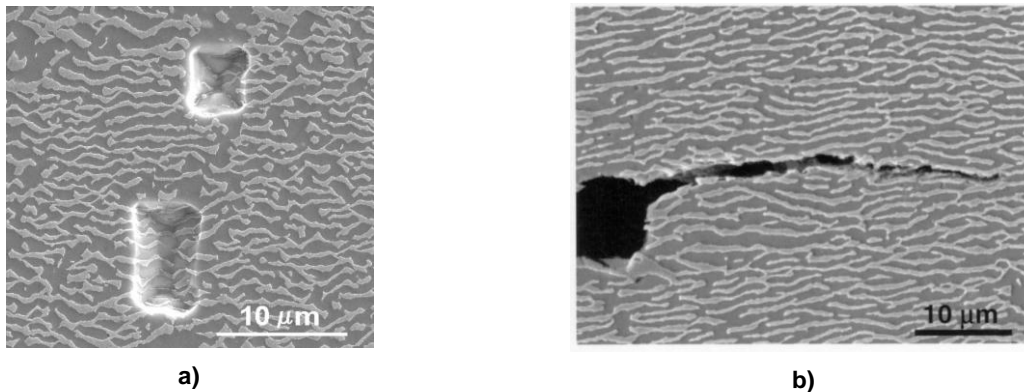


Figure 2.35 – a) Crystallographic pores; (b) Crack growth with nucleation at a pore and propagation along γ' -rafts. [68]

- **Precipitation of TCP Phases**

During the solidification of the TCP forming elements, they concentrate in the dendritic arms and this inhomogeneity persists even after homogenization, leading to, at higher temperatures, a supersaturation and precipitation of the TCP phases in the dendritic arms (**Figure 2.36**), leading to general strength reduction by depletion of refractory elements in the material around the TCPs.

The data about effects of TCP phases in LCF life is thus far contradictory and limited, and can be considered not critical for the HPT blades, although its morphology may be relevant, given that different TCP shapes might present either advantages or disadvantages for the materials mechanical properties, as well as the volume fraction of its precipitates. [57] [68]

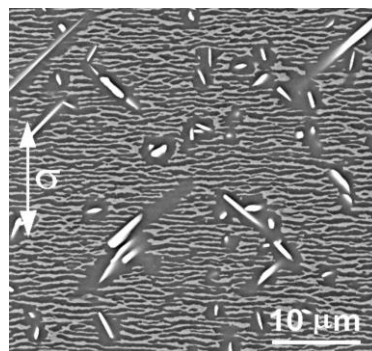


Figure 2.36 – Precipitation of TCP phases. [68]

3. Methodology

3.1. Problem Description

The PW150A, the engine under this study, seen in **Figure 3.1**, has been designed to perform at flight-cycle periods as low as one hour per cycle, i.e. time between engine start and shutdown. However, the nature of the company's operation requires the engine to perform at flight-cycle periods below the one hour mark, and that, combined with the corrosive nature of the marine environment in which the operation is conducted, has significant influence in the reduction of component life.



Figure 3.1 – PW150A engines of the Bombardier DHC8-400 aircraft in flight. [69]

As it has been discussed above, the life prediction and extension of critical engine components is the main engineering goal in aircraft design and maintenance. As with most engines, the components most susceptible to damage and failure are the HPT blades. This is the case for the regional airliner's operation under study, where it's been verified that, at the time of engine overhaul, the engine components that needed replacement were in fact the HPT blades, showing signs of increased wear after 1500 flight-hours. The new replacement HPT blades are now expected to have a life of around 3000 flight-hours.

When predicting the life of such a critical component of an aircraft gas turbine engine, it is important to have as much knowledge as possible about its operating conditions within engine, and study the variables that influence those conditions.

With the goal being the modeling of an HPT blade within this aircraft's engine and determination of its failure mechanisms, with special focus on creep, several flights of the four different aircraft were studied and the variations in Inter Turbine Temperature (ITT) and HPT rotation speed (NH) for each of the selected flights were obtained from the Flight Data Records (FDR), provided by the airline company. The modeling of the HPT blade itself was done through reverse engineering of a discarded damaged blade, also provided by the company.

3.2. Flight Data Record Processing

In order to obtain the operating conditions within the engine, mainly in the turbine inlet area, six different FDR's were analyzed and processed, with each of these consisting of the recording of about 25 flight-hours, in increments of one second, for various types of data (**Appendix A**), from which relevant data was extracted, as can be seen in **Table 3.1**.

Table 3.1 – Type of data collected from the FDR

| COUNTER | ALTcapt | CASrh | ENG1itt | ENG1nh | NAVlat | NAVlong |
|---------|---------------------|---------------------|---------------------------------------|----------------------------|----------|-----------|
| Time | Barometric altitude | Calibrated airspeed | Inter Turbine Temperature in Engine 1 | Rotation speed in Engine 1 | Latitude | Longitude |
| (s) | (m) | (knots) | (°C) | (%) | (°) | (°) |

Of the six FDR's, three of them were from one aircraft, the TRD, and the remaining three belonged to the other three aircraft in the fleet, the TRE, TRF and TRG, respectively.

Using the International Air Transport Association (IATA) airport codes, their respective locations in terms of latitude and longitude were determined, as can be seen in **Table 3.2**. Using that information and, considering that, at each airport, both the calibrated airspeed and NH would have to be zero, both the beginning and end of the flight cycles in each of the aircraft's Engine 1 were defined.

This was done using an algorithm specifying the location of the aircraft in one given airport, with an error of 0.5%. Thus, the different flight cycle periods and the routes flown by each of these aircraft were determined.

Table 3.2 – IATA airport codes and coordinates [70]

| Airport | IATA Code | Latitude (°) | Longitude (°) |
|---------------------------|-----------|--------------|---------------|
| Las Palmas (Gran Canaria) | LPA | 27,929972 | -15,387714 |
| Funchal (Madeira) | FNC | 32,696046 | -16,775745 |
| Ponta Delgada (S. Miguel) | PDL | 37,749432 | -25,710053 |
| Santa Maria | SMA | 36,974388 | -25,165534 |
| Terceira | TER | 38,754144 | -27,086997 |
| Horta (Faial) | HOR | 38,520222 | -28,716314 |
| Pico | PIX | 38,552648 | -28,443270 |
| São Jorge | SJZ | 38,665933 | -28,175612 |
| Graciosa | GRW | 39,092022 | -28,031858 |
| Flores | FLW | 39,456871 | -31,131377 |

Table 3.3 – Flight Routes for each aircraft

| Flight Route | Min. cycle period (min) | Max. cycle period (max) | Number of flights | TRD | TRE | TRF | TRG |
|--------------|-------------------------|-------------------------|-------------------|-----|-----|-----|-----|
| FNC-LPA | 70.23 | 82.1 | 6 | X | | X | X |
| LPA-FNC | 75.33 | 80.15 | 6 | X | | X | X |
| FNC-PDL | 116.42 | 124.02 | 6 | X | | X | X |
| PDL-FNC | 115.32 | 124.88 | 6 | X | | X | X |
| PDL-TER | 31.12 | 51.02 | 26 | X | X | X | X |
| TER-PDL | 29.72 | 46.2 | 30 | X | X | X | X |
| PDL-HOR | 51.08 | 58.1 | 6 | X | X | X | |
| HOR-PDL | 41.15 | 47.25 | 4 | X | X | | |
| PDL-PIX | 43.22 | 47.38 | 3 | X | | | X |
| PIX-PDL | 37.95 | 46.38 | 6 | X | X | X | X |
| PDL-FLW | 81.02 | 81.33 | 2 | | X | X | |
| FLW-PDL | 64.95 | 66.85 | 2 | | X | X | |
| PDL-SMA | 22.3 | 30.9 | 10 | X | X | X | X |
| SMA-PDL | 22.8 | 28.8 | 10 | X | X | X | X |
| PDL-SJZ | 48.33 | 48.85 | 2 | | X | | |
| TER-HOR | 29.33 | 36.92 | 11 | X | X | X | X |
| HOR-TER | 27.98 | 32.58 | 11 | X | X | X | X |
| TER-PIX | 24.57 | 33.4 | 13 | X | X | X | X |
| PIX-TER | 24.97 | 30.92 | 10 | X | | | X |
| TER-SJZ | 26.02 | 34.27 | 3 | X | | X | X |
| SJZ-TER | 22.55 | 24.5 | 5 | X | X | X | X |
| TER-GRW | 20.45 | 25.53 | 4 | X | X | X | |
| GRW-TER | 20.35 | 24.48 | 4 | X | X | X | |
| TER-FLW | 53.2 | 60.3 | 2 | X | | | |
| FLW-TER | 54.32 | 58.15 | 2 | X | | | |
| HOR-FLW | 40.97 | 44.87 | 3 | | X | X | |
| FLW-HOR | 37.45 | 42.17 | 3 | | X | X | |

From all the flights shown in **Table 3.3**, three were selected, and all their respective cycles in terms of ITT and NH were plotted for both engines. The flight routes were selected in order to represent the presumed to be most aggressive type of flight cycle for the engine, i.e. the shortest, SJZ-TER; the least aggressive, i.e. the longest, PDL-FNC; and the cycle whose time frame would most resemble the ideal flight cycle period, as defined by the engineering chief at the company, i.e. one hour cycle period, PDL-HOR. The selection criterion was focused not only on the cycle periods, but also in the amount of data available for each of the selected flight routes. Thus, routes with flight

cycle periods closer to the target timeframe were not used due to the small number of flights that would make us unable to do a proper description of the cycle in terms of both ITT and NH. The same criterion was applied to cycles with greater amounts of data whose difference in minimum and maximum cycle periods were deemed too large to be considered for the analysis, with exception of the PDL-FNC flight route, given that it was the longest available. As can be seen in **Table 3.3** and in **Figure 3.2** through **Figure 3.4**, the number of flights is between five and six, which gives us enough raw data for the following steps on the data processing.

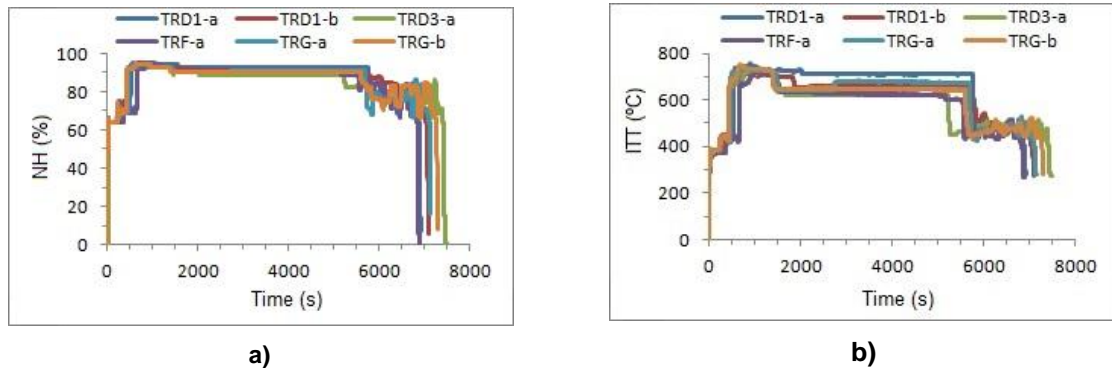


Figure 3.2 – Engine 1 flight cycle curves for PDL-FNC flight route for a) NH; b) ITT.

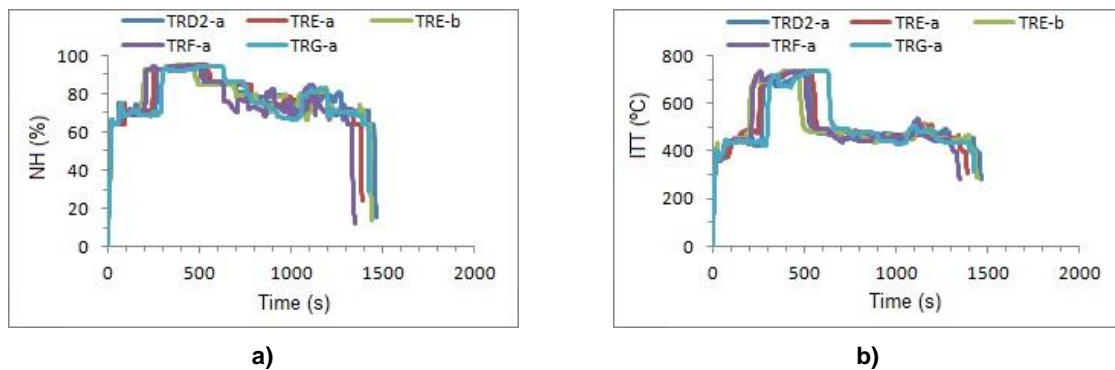


Figure 3.3 – Engine 1 flight cycle curves for SJZ-TER flight route for a) NH; b) ITT.

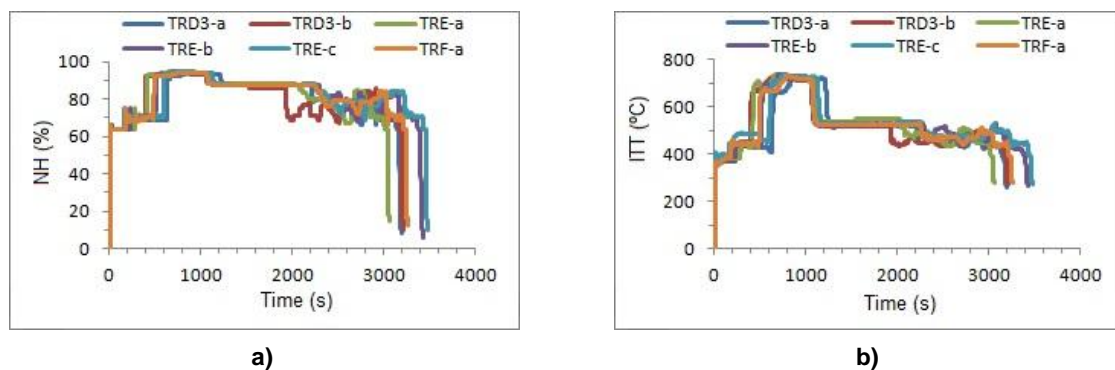


Figure 3.4 – Engine 1 flight cycle curves for PDL-HOR flight route for a) NH; b) ITT.

With the goal of describing both the temperature and the centrifugal force cycles that the HPT blades are subjected to, an average plot was defined for each of the data sets.

To characterize the temperatures the HPT blades are subjected to from the air incoming from the combustion chamber, the data of the Turbine Inlet Temperature (TIT) was necessary. However, the FDR does not provide this data, only providing ITT data, whose location was not defined in the available literature. Nonetheless, knowing that the highest allowable ITT for this engine is 920 °C for a transient state with a period no longer than 20 seconds [45], and that the usual operating temperature for blades with cooling systems applied is defined between 927.82 °C (1200 K) and 1027.85 °C (1300 K) [49], the maximum allowable temperature of 1027.85 °C was assumed. Subtracting the maximum allowable ITT, a temperature differential between the FDR's ITT and the assumed TIT of 107.85 °C was defined.

This temperature differential was then added to the averaged plots for each of the flight cycles selected, with the maximum flight cycle period for each case having been chosen. This created the need to compensate for the abrupt increase in the initial temperature that was averaged from all the ITT curves. Thus, the temperature was manually increased by increments of 10 °C until the temperature differential of 107.85 °C was attained and then applied to the rest of the averaged plot.

Given that the FDR ended when the engine is shut off, i.e. the NH dropped to zero, the cooling of the blades was not recorded. However, for the definition of the thermal cycle of the HPT blades, they needed to be cooled down to room temperature, which has been defined as being 20 °C. In order to accomplish this, the temperature at the end of the averaged flight cycle was reduced in increments of 1 °C/s, until the 20 °C temperature was attained in the surface. This temperature then needed to be maintained for an added period of 195 seconds, in order to allow for the overall temperature of the blade to be cooled to about 20 °C, as will be described in later sections of this chapter.

As for the characterization of the centrifugal force, the software used in the subsequent analysis, which will be described in further sections of this chapter, required the NH to be given in radians per second (rad/s). As seen in **Table 3.1**, the NH was given in terms of percentage (%) and as previously stated, the HPT blades rotate with a maximum speed of 31150 rpm (100%). Using **Equation 3.1**, for which the diameter of the HPT disc housing the blades was obtained in the following section of this chapter, the different speed (rad/s) vs time (s) plots for all the selected flight cycles were defined and an average plot to describe each of those cycles was obtained.

$$\omega_{HPT} = \frac{31150 \times NH \times 60}{\pi} \quad (3.1)$$

It should be noted that no data regarding pressure in the HPT section was available, and thus all studies conducted on the blades completely disregard the considerable effects of pressure in that section, and constitute one of the major simplifications that was made in this study.

This limitation is also the reason why, along with other issues to be discussed on the next section of this chapter, the cooling airflow and its temperature variation were not calculated nor considered in the study. In the specific case of the airflow temperature, the only data given was the exterior static air temperature (**Appendix A**), and from section **2.3.3.**, it is known that the air is bled into the cooling system from the 3rd stage of the axial compressor. Considering that the compression

ratio up to that point was not given in the literature nor was there enough data to make the calculations, defining this temperature variation wasn't possible.

Thus, the final plots for TIT and ω_{HPT} for the different flight routes under study can be seen in **Figure 3.5** through **Figure 3.7**.

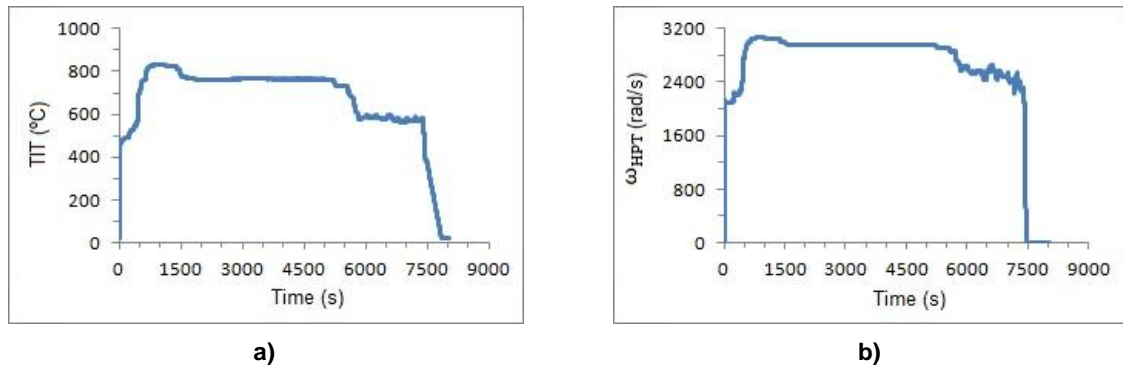


Figure 3.5 – PDL-FNC flight route's averaged cycles for a) TIT; b) ω_{HPT} .

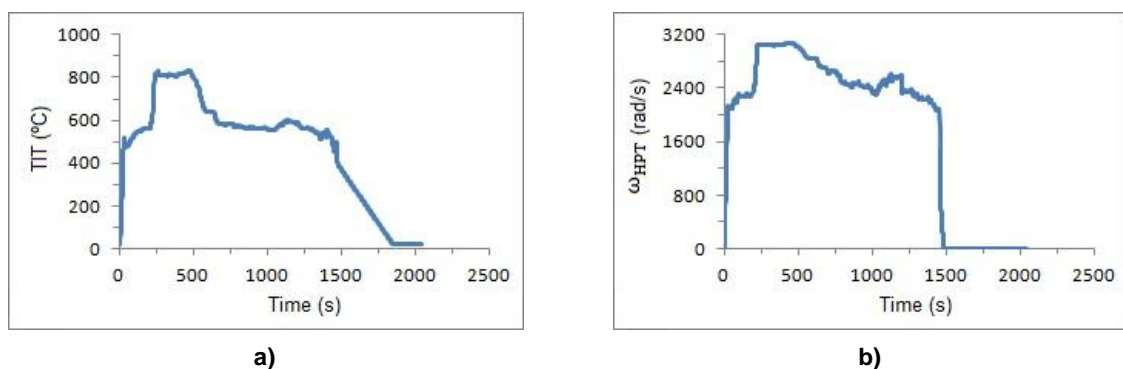


Figure 3.6 – SJZ-TER flight route's averaged cycles for a) TIT; b) ω_{HPT} .

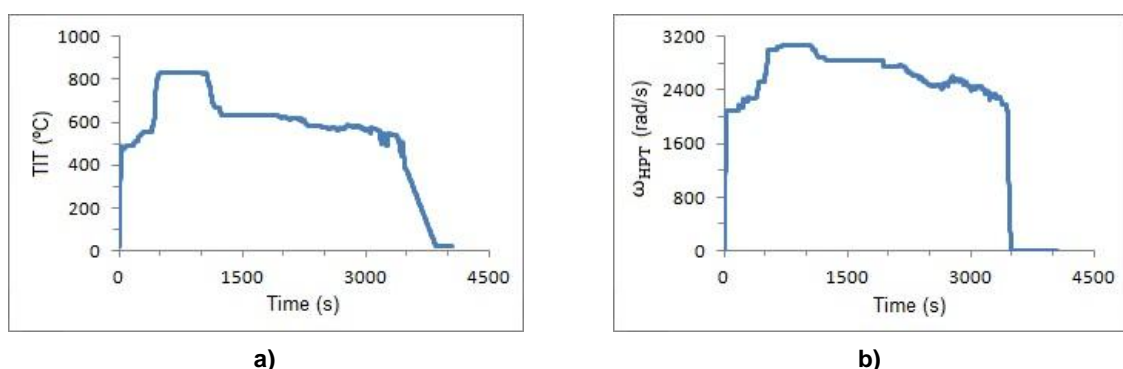


Figure 3.7 – PDL-HOR flight route's averaged cycles for a) TIT; b) ω_{HPT} .

In **Table 3.4** the different flight cycle period data extracted from the FDR for Engine 1 is shown, as well as the final flight cycle periods for each of the flight routes studied and the number of cycles needed for each route to reach the expected 3000 flight-hours lifetime.

Table 3.4 – Flight cycle periods and number of cycles for expected lifetime for Engine 1

| Flight Route | Min. cycle Period | Max. cycle Period | Cycle Period | Cycle Period w/ Cooling | Total Cycle Period | Cycles/3000h |
|----------------|-------------------|-------------------|--------------|-------------------------|--------------------|--------------|
| | (min) | (min) | (s) | (s) | (s) | |
| PDL-FNC | 115.32 | 124.88 | 7492 | 7855 | 8050 | 1342 |
| PDL-HOR | 51.08 | 58.1 | 3486 | 3859 | 4055 | 2664 |
| SJZ-TER | 22.55 | 24.5 | 1470 | 1854 | 2050 | 5269 |

3.3. Part Reverse Engineering and Modeling

3.3.1. Part Modeling

Considering both the geometric and material complexity of the HPT blades under study, efforts were made to obtain not only a precise 3D geometric drawing of the part but also the composition of its superalloy. To that end, the regional airline with whose collaboration this study was made was able to provide one discarded and damaged HPT blade, seen in **Figure 3.8**, from which most of the data needed was then reverse engineered.

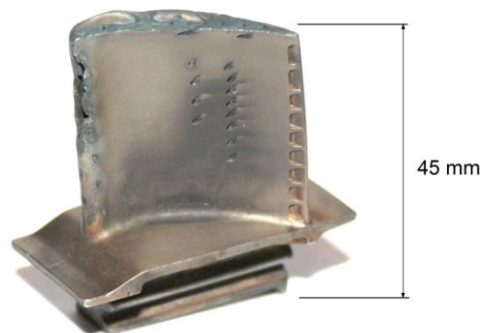


Figure 3.8 – HPT blade scrap.

One of the first steps was creating a 3D model of the part. Using a handheld, portable, self-positioning, real-time surfacing, 3D laser scanner, the Zscanner 700, whose specs can be seen in **Table 3.5**, a polygon mesh of the HPT blade's surface was created in the scanner's ZScan software.

Table 3.5 – Zscanner 700 specs [71]

| | |
|------------------------------|--|
| Weight | 0.98 kg |
| Dimensions | 160 x 260 x 210 mm |
| Sampling Speed | 18.000 measurements/s |
| Laser | Class II (eye safe) |
| Number of Cameras | 2 |
| XY accuracy | Up to 0.05 mm |
| Resolution | 0.1 mm in Z |
| ISO | 20 μm + 0.2 L / 1000 |
| Texture Resolution | 50 to 350 DPI |
| Texture Color | 24 bits (sRGB-calibrated) |
| Depth of Field | 30 cm |
| Exported File Formats | .DAE, .FBX, .MA, .OBJ, .PLY, .STL, .TXT, .WRL, .X3D, .X3DZ, .ZPR |
| Data Transfer | FireWire |
| Power Source | FireWire |

Although the equipment is well suited for the 3D mapping of large parts, the reduced dimensions of the HPT blade scrap made it difficult to correctly calibrate and obtain a proper 3D surface, thus several attempts were needed. The result was a considerably rough surface model, as can be seen in **Figure 3.9 a)** and **b)**, which was then saved in a .STL file as a polygon mesh of the surface.

That file was then used in the Solid Works 2014 Premium 3D modeling software where it was converted from the polygon mesh, **Figure 3.10 a)**, into an editable surface, **Figure 3.10 b)**.

Given the fact that only one scrap part was available, the limited information in the literature, the limited data provided by the FDR regarding the conditions in all the sections of interest, and finally, the limitations of the 3D scanning method used, obtaining a 3D model of the interior of the part, especially the cooling channels inside it, was also not possible. For this reason and the ones mentioned in the previous section, the behavior of the cooling air was not studied.

In light of these limitations, instead of creating a 3D model of a cooled HPT blade, a full blade design, i.e. with no cooling, was used for the rest of the analysis. Any results further obtained will thus have limited relation with the real life behavior of the part, given the simplifications used thus far.



Figure 3.9 – 3D surface mapping of the HPT blade scrap in the ZScan software.



Figure 3.10 – a) Polygon mesh of part surface; b) editable surface of part.

To achieve a proper 3D model, the polygon mesh in **Figure 3.10 a)** was used as a visual aid and, along with raw physical dimensional measurements of the blade, the 3D model was manually created in Solid Works 2014 Premium over the mesh, using the editable surface in **Figure 3.10 b)** as planar reference. The result can be seen in **Figure 3.11**.



Figure 3.11 – a) HPT blade 3D model a) with drawing edges; b) without drawing edges.

From the dimension highlighted in **Figure 3.12**, the width of the blade's base is $l = 16.9$ mm, and knowing that there are $N = 41$ blades in the HPT, a reference perimeter for the HPT disk was calculated using **Equation 3.2**:

$$P = l \cdot N = 693 \text{ mm} \quad (3.2)$$

Using this result and **Equation 3.3**, the radius of the HPT disk was defined, which was later used to calculate the centrifugal force applied to the HPT blades in each instant.

$$P = 2 \pi \times r \Leftrightarrow r = \frac{P}{2\pi} = 111 \text{ mm} \quad (3.3)$$

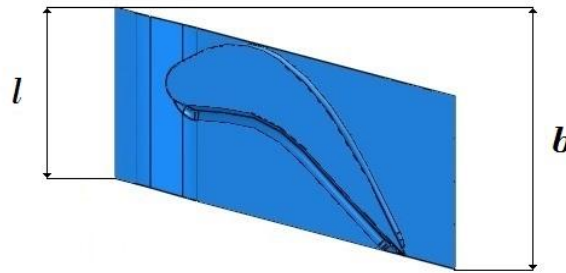


Figure 3.12 – HPT blade’s base width.

3.3.2. Superalloy Material Data and Composition

With the 3D model complete, the nature of the superalloy and its composition needed to be analyzed, in order to have a raw idea of which superalloy should be properly selected from the literature.

In a first step, the mass of the part was measured at a room temperature of 20 °C, and then again submerged in purified water, at the same temperature. With the data from **Table 3.6** and using **Equation 3.4**, the volume of water displaced (V) was obtained, and with **Equation 3.5**, a density value for the base superalloy (ρ_{HPT}) was defined. It is important to note that, since the part provided is a scrap, all information extracted from it serves only as reference, given the damage it had incurred and the possible presence of contaminant elements.

Table 3.6 – HPT blade weight measurements

| Temperature | Density Pure water | Mass HPT blade | Mass Submerged |
|-------------|----------------------|-----------------------|-----------------------|
| T | ρ_{H2O} | m_{HPT} | m_S |
| (°C) | (kg/m ³) | (kg) | (kg) |
| 20 | 998.2 | 42.1×10^{-3} | 37.2×10^{-3} |

$$V = \frac{m_{HPT} - m_S}{\rho_{H2O}} = 4.89 \times 10^{-6} \text{ m}^3 \quad (3.4)$$

$$\rho_{HPT} = \frac{m_{HPT}}{V} = 8605 \text{ kg/m}^3 \quad (3.5)$$

In order to analyze the chemical composition of three different sections of the HPT blade, as indicated in **Figure 3.13**, specified as Top, Body and Base, a surface Scanning Electron Microscopy (SEM) analysis was performed with the images being taken at 25.0 kVamp, as well as an Energy Dispersive Spectroscopy (EDS) mapping, both at the ICEMS/IST MicroLab using an FEG-SEM JSM7001F microscope and an Oxford INCA 205 EDS light element detector. The composition was determined through a semi-quantitative analysis and the results can be seen in **Table 3.7** through **Table 3.9**.

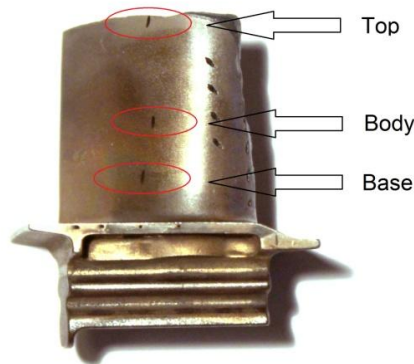


Figure 3.13 – HPT blade sections where SEM and EDS were performed.

From these results and from the literature, it can be seen that the HPT blade is made of a nickel-based alloy with the expected ratio of chromium and cobalt, typical of this type of superalloy. The varying concentration of both aluminum and platinum can easily be attributed to the base PtAl anti-corrosion coating usually found in these alloys, as well as the fact that the uncoated alloy is expected to present an appreciable amount of the former.

The absence of any of the ceramic elements, that would be expected as part of the TBC, i.e. the yttria-stabilized zirconia, is also explained given the fact that our sample is a scraped and damaged HPT blade, thus it is correct to assume the TBC layer, the outmost layer, has been completely removed.

Looking at each section specifically, the history of the damage the blade may have been subjected to can be inferred.

For instance, in the Top section, given the fact that it is the area where the most wear can be seen, Spectrum 1 and 3 shows the highest concentrations of aluminum, and smaller concentrations of platinum as well as nickel. This can be explained not only through the presence of the anti-corrosion coating, but also given the fact that most of the wear is visible in this section, as well as in the leading edge, where neither EDS nor SEM were performed. The lower amount of platinum can be attributed to

the nature of the aluminum oxide film that forms in the regions mentioned, as well as due to the nature of the EDS mapping, as the depth of penetration of the x-rays greatly influences the spectrum.

The same section, in Spectrum 2, shows what seems to be the actual superalloy's composition, as the amount of aluminum drops to expected levels and we see a fair amount of tantalum, expected in these types of alloys, and the nickel amount is closer to the real percentage expected in this material.

In the Body section, a higher concentration of iron contamination can be seen in Spectrum 1, and in Spectrum 2, given the reduction of the area selected, the iron percentage drops and we once more have an appreciable amount of anti-corrosion coating.

Finally, in the Base section, not only a noticeable concentration of the coating elements (aluminum and platinum) can be seen, that can be easily explained by the complete removal of the TBC coating during operation and the formation of the protective layers of aluminum oxide, as well as a percentage of iron, which can only be explained as a contaminant, either due to ingestion of exterior air or the degradation of upstream engine components.

Table 3.7 – EDS of Top section

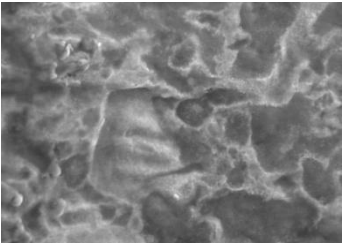
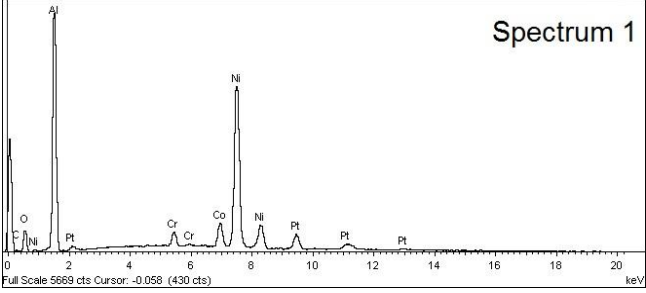
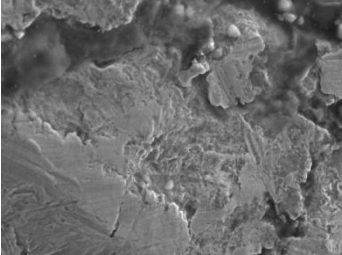
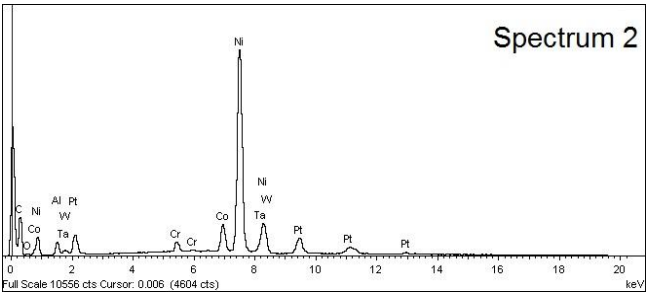
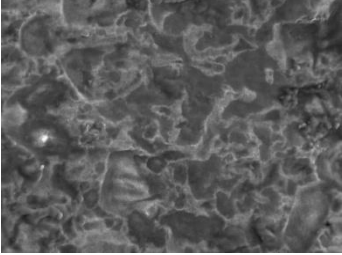
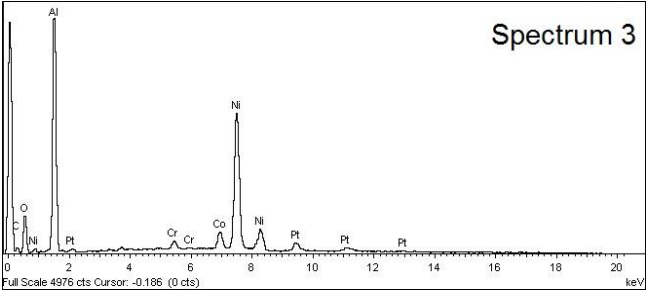
| Electron Image (SEM) | Spectrum (EDS) | Element | Wt % |
|---|--|----------------------------------|---|
|  <p>x 1000</p> |  <p>Spectrum 1</p> | Al Cr Co Ni Pt | 39.39 2.31 6.43 50.22 1.65 |
|  <p>x 900</p> |  <p>Spectrum 2</p> | Al Cr Co Ni Ta Pt | 3.36 1.99 8.68 74.87 2.27 8.84 |
|  <p>X 550</p> |  <p>Spectrum 3</p> | Al Cr Co Ni Pt | 43.57 1.51 5.27 48.10 1.55 |

Table 3.8 – EDS of Body section

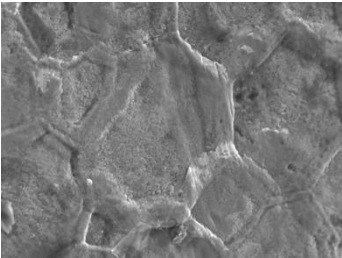
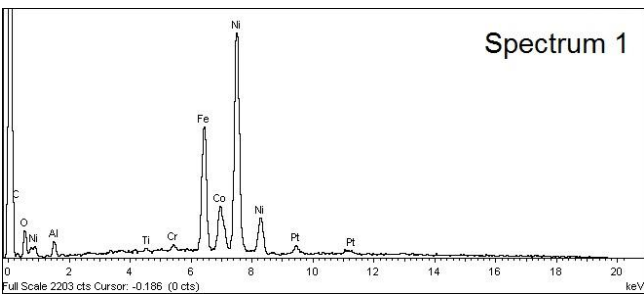
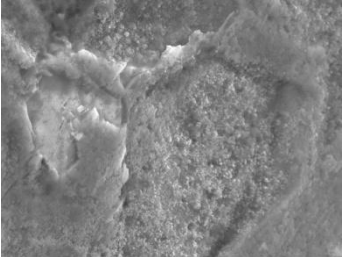
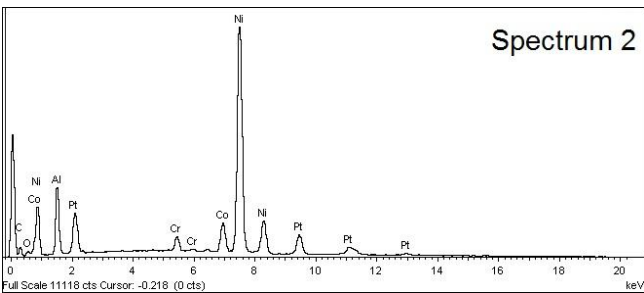
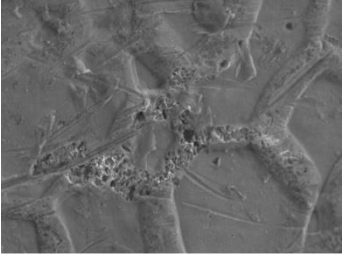
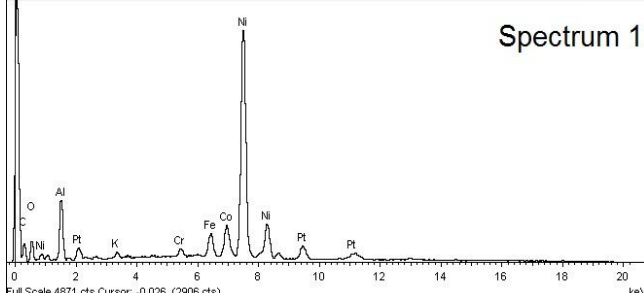
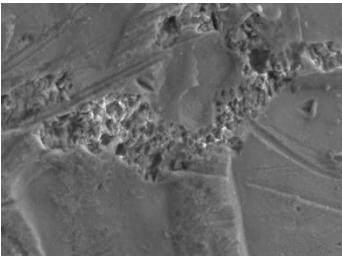
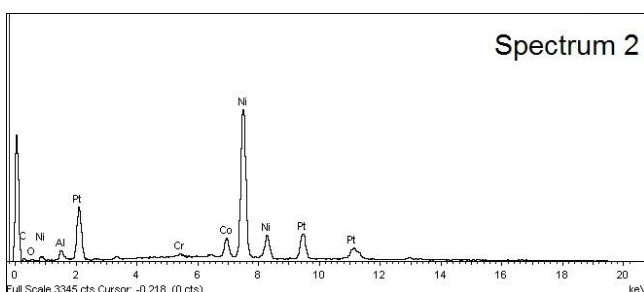
| Electron Image (SEM) | Spectrum (EDS) | Element | Wt % |
|---|--|---------|-------|
|  <p>x 550</p> |  <p>Spectrum 1</p> | Al | 3.25 |
| | | Ti | 0.45 |
| | | Cr | 0.75 |
| | | Fe | 22.04 |
| | | Co | 9.61 |
| | | Ni | 63.99 |
| | | Pt | 0.08 |
|  <p>x 2000</p> |  <p>Spectrum 2</p> | Al | 12.16 |
| | | Cr | 2.28 |
| | | Fe | 0.31 |
| | | Co | 7.34 |
| | | Ni | 64.42 |
| | | Pt | 13.49 |

Table 3.9 – EDS of Base section

| Electron Image (SEM) | Spectrum (EDS) | Element | Wt % |
|---|--|---------|-------|
|  <p>x 550</p> |  <p>Spectrum 1</p> | Al | 12.78 |
| | | Cr | 1.21 |
| | | Fe | 4.19 |
| | | Co | 7.81 |
| | | Ni | 69.23 |
| | | Pt | 4.78 |
|  <p>x 1000</p> |  <p>Spectrum 2</p> | Al | 2.53 |
| | | Cr | 0.59 |
| | | Co | 7.06 |
| | | Ni | 64.91 |
| | | Pt | 24.91 |

3.3.3. Superalloy Selection and Properties

From the previous section, the type of superalloy that should be found in the available literature is made clear and thus only two different superalloys were considered, the CMSX-4 and the TMS-75.

These are 2nd and 3rd generation nickel base single-crystal superalloys, respectively, and are specifically used for HPT blades. Only these were considered, not only for the specificity of their application to this part, but also because they were the only ones whose literature presented the properties required in this study. [72]

Table 3.10 – Chemical composition wt% [72]

| Element | Ni | Al | Co | Cr | Hf | Mo | Re | Ti | W | Ta |
|---------------|------|-----|------|-----|-----|-----|-----|-----|-----|-----|
| CMSX-4 | bal. | 5.6 | 9.0 | 6.5 | 0.1 | 0.6 | 3.0 | 1.0 | 6.0 | 6.5 |
| TMS-75 | bal. | 6.0 | 12.0 | 3.0 | 0.1 | 2.0 | 5.0 | - | 6.0 | 6.0 |

Looking at both compositions in the **Table 3.10**, some similarities may be seen. However, not only is the Co/Cr ratio completely different (4/1 and 3/2), but a higher presence of alloying elements in the TMS-75, the newest of the two, is noticeable with the exception of titanium, which is non-existent.

Due to this difference, along with the fact that the HPT blades under study are made of a more recent superalloy (as stated by the chief engineer of the collaborating company, they have been in service as of 2011), its nature as a 3rd generation superalloy, and its Co/Cr ratio being almost matched by the one measured in the previous section, the TMS-75 superalloy was chosen and its properties became the reference material for the remainder of this study.

It is important to take into account that the material density at room temperature obtained in the previous section is closer to that of the CMSX-4 than to the TMS-75. However, the nature of the alloy composition in this case was the deciding factor, as well as the knowledge that the discarded blade's measured density may not be the same as its original density, given the series of thermal cycles it has gone through.

The properties of the TMS-75 superalloy were presented in three forms: physical constants, plots and tables. The physical constants, Density and Mean Thermal Expansion Coefficient α , are given in **Table 3.12**; the plotted data, regarding the Young's Modulus, Thermal Conductivity and Specific Heat, can be seen in **Figure 3.14** through **Figure 3.16**; and the remaining information provided in the literature, regarding Tensile Strength and Creep Rupture Strength, is shown in **Table 3.13** and **Table 3.14**, respectively.

Table 3.11 – Temperature-dependent thermal and mechanical properties of the CMSX-4 superalloy [73]

| Temp. | Thermal Cond. | Density | Specific Heat Capacity | Young's Modulus along (100) | Shear Modulus | Poisson's ratio | Mean Thermal Expansion Coefficient | Yield Stress ($\epsilon_{pl}=0$) | Yield Stress ($\epsilon_{pl}=5\%$) |
|-------------|---|---------------------------------|--|-----------------------------|---------------|-----------------|------------------------------------|------------------------------------|--------------------------------------|
| T (°C) | k (W m ⁻¹ K ⁻¹) | ρ (kg m ⁻³) | C_p (J kg ⁻¹ K ⁻¹) | E (GPa) | G (GPa) | ν (-) | α (x10 ⁻⁶) | (MPa) | (MPa) |
| 20 | 8.65 | 8700 | 397 | 127.3 | 131.3 | 0.389 | 11.1 | 385.0 | 411.0 |
| 100 | 8.65 | 8665 | 415 | 125.0 | 128.7 | 0.391 | 11.8 | 384.0 | 409.0 |
| 200 | 10.1 | 8618 | 431 | 122.0 | 125.5 | 0.394 | 12.8 | 383.0 | 408.0 |
| 300 | 11.6 | 8572 | 445 | 118.0 | 121.9 | 0.395 | 13.7 | 382.0 | 406.0 |
| 400 | 13.4 | 8525 | 456 | 115.0 | 118.6 | 0.395 | 14.7 | 381.0 | 404.0 |
| 500 | 14.9 | 8479 | 466 | 111.0 | 114.3 | 0.395 | 15.6 | 380.0 | 402.0 |
| 600 | 16.8 | 8433 | 488 | 106.0 | 109.9 | 0.396 | 16.5 | 383.0 | 405.0 |
| 700 | 19.4 | 8387 | 532 | 101.0 | 107.1 | 0.398 | 17.4 | 406.0 | 427.0 |
| 800 | 20.6 | 8342 | 530 | 96.0 | 102.3 | 0.403 | 18.3 | 446.0 | 466.0 |
| 900 | 21.8 | 8296 | 540 | 90.2 | 99.0 | 0.41 | 19.2 | 346.0 | 365.0 |
| 1000 | 22.3 | 8251 | 550 | 82.7 | 93.7 | 0.42 | 20.1 | 269.0 | 286.0 |
| 1100 | 23.9 | 8206 | 560 | 75.1 | 88.3 | 0.43 | 21.0 | 165.0 | 181.0 |
| 1200 | 25.8 | 8161 | 570 | 67.6 | 82.9 | 0.44 | 21.8 | 63.7 | 77.5 |
| 1300 | 27.2 | 8116 | 580 | 60.1 | 77.5 | 0.45 | 22.7 | 27.6 | 39.9 |
| 1320 | 27.2 | 8107 | 580 | 58.6 | 76.4 | 0.452 | 19.5 | 20.4 | 32.4 |
| 1380 | 35.0 | 7754 | 675 | 54.0 | 73.2 | 0.458 | 18.6 | 20.4 | 31.4 |
| 2000 | 35.0 | 7754 | 675 | 54.0 | 73.2 | 0.458 | 12.9 | 20.4 | 31.4 |

Table 3.12 – Physical constants and thermal properties provided for TMS-75 superalloy [74]

| Temperature Range | Density | Mean Thermal Expansion Coefficient |
|-------------------|---------------------------------|------------------------------------|
| T (°C) | ρ (kg m ⁻³) | α (x10 ⁻⁶) |
| 20 - 200 | 8894 | 11.7 |

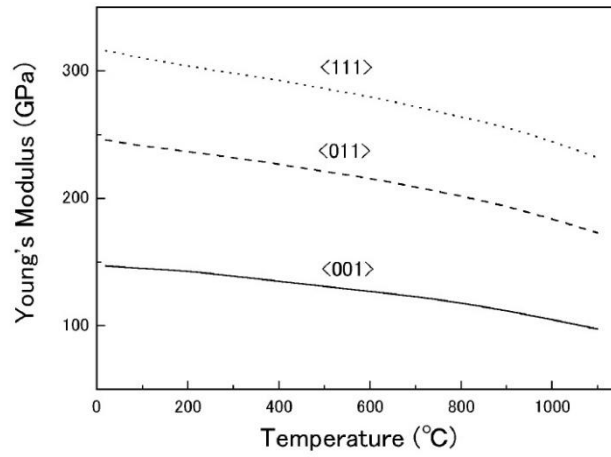


Figure 3.14 – Young's modulus obtained using rectangular parallelepiped resonance. [74]

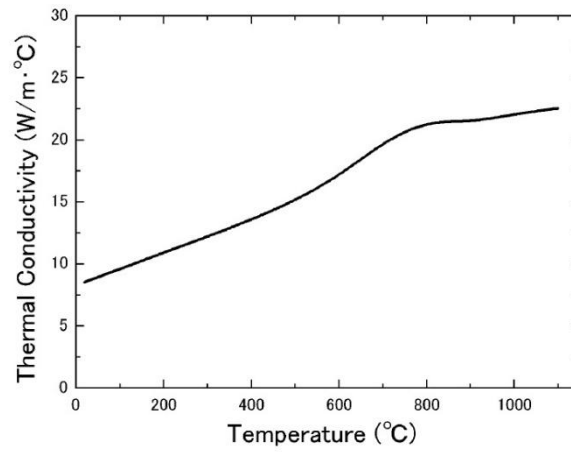


Figure 3.15 – Thermal conductivity obtained using the Laser-Flush Method. [74]

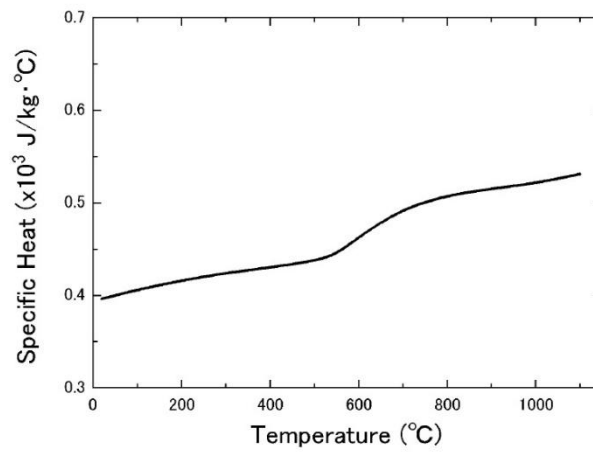


Figure 3.16 – Specific heat obtained using an adiabatic calorimeter (Nernst Method). [74]

Table 3.13 – Tensile strength provided for the TMS-75 superalloy [74]

| Temperature <i>T</i> °C (K) | 0.2% Proof Stress $\sigma_{0.2}$ (MPa) | UTS σ_{UTS} (MPa) | Elongation <i>e</i> (%) | Reduction of area (-) (%) |
|-----------------------------------|--|--------------------------------|-------------------------------|---------------------------------|
| 20 (293) | 850 | 898 | 7.0 | 14 |
| 550 (823) | 805 | 863 | 6.5 | 11 |
| 750 (1023) | 972 | 1287 | 7.7 | 9 |
| 850 (1123) | 893 | 1179 | 14 | 18 |
| 950 (1223) | 564 | 932 | 20 | 24 |
| 1050 (1323) | 513 | 717 | 16 | 41 |
| 1150 (1423) | 266 | 417 | - | - |

Table 3.14 – Creep rupture strength provided for the TMS-75 superalloy [74]

| Conditions | | Rupture life τ (h) | Elongation <i>e</i> (%) | Reduction of area (-) (%) |
|-----------------------------------|-----------------------------|-------------------------------|-------------------------------|---------------------------------|
| Temperature <i>T</i> °C (K) | Stress σ (MPa) | | | |
| 900 (1173) | 392 | 961 | 23.0 | 30.3 |
| 1100 (1373) | 137.2 | 227 | 14.0 | 26.2 |
| 1150 (1423) | 98 | 196 | 11.9 | 39.1 |

The plotted data, shown in **Figure 3.14** through **Figure 3.16**, had to be analyzed and shown in table form, in order to be later introduced into the material properties module of the FEM software, to be discussed in the next section. Using the student version of the AutoCAD 2012 modeling software, a 2D grid was created using the different plotted scales, and the approximate values of each plot for selected temperature values were obtained, as can be seen in **Table 3.15**.

In order to obtain the Poisson's Ratio, required by the FEM software, which was unavailable in any of the literature for the TMS-75 superalloy, an approximation had to be done. Considering the similarities between both alloys, the Poisson's Ratio evolution of the CMSX-4 superalloy in **Table 3.11** was plotted, and the plot was then adjusted to match the tabled values for the Young's Modulus of the TMS-75 superalloy, as can be seen in **Table 3.15**.

In a similar fashion, both the values of Density and of the Thermal Expansion Coefficient α , for the temperatures selected, were put into table form.

In **Table 3.16**, the Plastic strains were calculated using the Young's Modulus data of **Table 3.15** for each of the temperatures and stresses in **Table 3.13**, using **Equation 3.6**:

$$\varepsilon_{pl} = e - \frac{\sigma_{UTS}}{E} \quad (3.6)$$

Table 3.15 - Temperature-dependent thermal and mechanical properties of the TMS-75 superalloy

| Temp. | Thermal Conductivity | Density | Specific Heat Capacity | Young's Modulus along (001) | Poisson's ratio | Mean Thermal Expansion Coefficient |
|-------------|---|---------------------------------|--|-----------------------------|-----------------|------------------------------------|
| T (°C) | k (W m ⁻¹ K ⁻¹) | ρ (kg m ⁻³) | C_p (J kg ⁻¹ K ⁻¹) | E (MPa) | ν (-) | α (x10 ⁻⁶) |
| 20 | - | 8894 | - | - | - | 11.7 |
| 50 | 8.909 | 8880 | 401 | 145980 | 0.392925 | 11.7 |
| 100 | 9.563 | 8857 | 407 | 144650 | 0.3918 | 11.7 |
| 150 | 10.266 | 8833 | 412 | 143710 | 0.390925 | 11.7 |
| 200 | 10.928 | 8810 | 417 | 142560 | 0.3903 | 11.7 |
| 250 | 11.571 | 8787 | 421 | 140820 | 0.389925 | 12.3 |
| 300 | 12.225 | 8764 | 425 | 138800 | 0.3898 | 12.9 |
| 350 | 12.899 | 8741 | 428 | 136750 | 0.389925 | 13.4 |
| 400 | 13.624 | 8718 | 431 | 134630 | 0.3903 | 13.9 |
| 450 | 14.404 | 8695 | 435 | 132720 | 0.390925 | 14.4 |
| 500 | 15.240 | 8672 | 439 | 130740 | 0.3918 | 14.9 |
| 550 | 16.195 | 8649 | 448 | 128420 | 0.392925 | 15.3 |
| 600 | 17.301 | 8626 | 465 | 126610 | 0.3943 | 15.7 |
| 650 | 18.543 | 8603 | 480 | 124520 | 0.395925 | 16.1 |
| 700 | 19.764 | 8580 | 493 | 122560 | 0.3978 | 16.5 |
| 750 | 20.699 | 8557 | 502 | 119990 | 0.399925 | 16.8 |
| 800 | 21.293 | 8534 | 509 | 117340 | 0.4023 | 17.1 |
| 850 | 21.506 | 8512 | 513 | 114540 | 0.404925 | 17.4 |
| 900 | 21.594 | 8489 | 517 | 111340 | 0.4078 | 17.7 |
| 950 | 21.820 | 8466 | 520 | 107490 | 0.410925 | 17.9 |
| 1000 | 22.111 | 8444 | 524 | 104490 | 0.4143 | 18.1 |
| 1050 | 22.374 | 8421 | 528 | 100900 | 0.417925 | 18.3 |

Table 3.16 – Temperature and stress dependent plastic strain for the TMS-75 superalloy

| Temperature | 0.2% Proof Stress | Plastic Strain | UTS | Plastic Strain |
|---------------|-------------------------|------------------------|-------------------------|------------------------|
| T °C (K) | $\sigma_{0.2}$ (MPa) | ϵ_{pl} (-) | σ_{UTS} (MPa) | ϵ_{pl} (-) |
| 20 (293) | 850 | 0 | 898 | 0.06414988 |
| 550 (823) | 805 | 0 | 863 | 0.0587315 |
| 750 (1023) | 972 | 0 | 1287 | 0.06889932 |
| 850 (1123) | 893 | 0 | 1179 | 0.13220359 |
| 950 (1223) | 564 | 0 | 932 | 0.19477584 |
| 1050 (1323) | 513 | 0 | 717 | 0.15491575 |

Finally, the creep rupture strength data from **Table 3.14**, had to be defined in terms of a steady-state creep rate, as shown in **Equation 3.7**, as required by the FEM software:

$$\dot{\epsilon}_s = K_1 \sigma^n \quad (3.7)$$

where $\dot{\epsilon}_s$ is the creep or strain rate, K_1 is a temperature dependent material constant, σ is the applied stress and n is the creep stress exponent.

Given the fact that **Table 3.14** showed three different creep conditions and their respective results, three different, temperature dependent, steady-state creep rate equations were expected. Thus, **Equation 3.8** was used:

$$\dot{\epsilon}_s = K_2 \sigma^n \exp\left(-\frac{Q_c}{RT}\right) \quad (3.8)$$

where K_2 is a material constant, T is the temperature of the material, R is the ideal gas constant and Q_c is the activation energy for creep. Using the data for temperature, stress and calculating the strain rate from the data in **Table 3.14**, a system of three equations with three unknowns was solved with the linear version of **Equation 3.8**:

$$\ln(\dot{\epsilon}_s) = \ln(K_2) + n \ln(\sigma) - \frac{Q_c}{R} \frac{1}{T} \quad (3.9)$$

With the values for Q_c , n , and $\ln(K_2)$ solved in the system, **Equation 3.10** was used to define the three different material constants needed for the FEM software:

$$K_1 = K_2 \exp\left(-\frac{Q_c}{RT}\right) \quad (3.10)$$

The different values for K_1 and n for the different temperatures can be seen in **Table 3.17**:

Table 3.17 – Steady-state creep constants for the TMS-75 superalloy

| Temperature | Temp. dependant material constant | Material constant | Creep Stress Exponent | Creep Activation Energy |
|---------------|-----------------------------------|--------------------|-----------------------|---------------------------------|
| T °C (K) | K_1 (SI) | $\ln(K_2)$ (SI) | n (-) | Q_c (J mol ⁻¹) |
| 900 (1173) | 5.575×10^{-23} | -32.0985 | 1.754447 | 186685.5 |
| 1100 (1373) | 9.062×10^{-22} | -32.0985 | 1.754447 | 186685.5 |
| 1150 (1423) | 1.610×10^{-21} | -32.0985 | 1.754447 | 186685.5 |

3.4. Finite Element Modeling

In an effort to properly study the behavior of the HPT blade in terms of creep, Abaqus/CAE 6.13-1, a suite of powerful simulation programs based on the finite element method (FEM), was used to simulate the different flight cycles discussed in previous chapters.

With this software it was possible to perform the preprocessing (input file), i.e. create a model, assign it material properties and apply both loads and constraints, as well mesh the geometry, run the simulation (output file) and verify the results (visualization).

In a first approach, a simple geometrical shape, a rectangular block, was modeled and used to test the two different types of interrelated model, the thermal model, in which temperature distribution in the geometry from the thermal cycle is calculated, and the mechanical model, where the stresses and part displacement are calculated from the centrifugal load caused by the varying rotational speed, and the varying temperature distribution.

These tests then validated the method in which the blade model, obtained in section 3.3.1., was tested and whose results were then be analyzed and discussed on further chapters.

3.4.1. Rectangular Block Model

In order to test the methodology that would be later applied to the blade model obtained in section 3.3.1., a simple rectangular block was created in the Part Module, using the basic dimensions of the upper part of the HPT blade, i.e. the airfoil geometry, as can be seen in **Figure 3.17**:

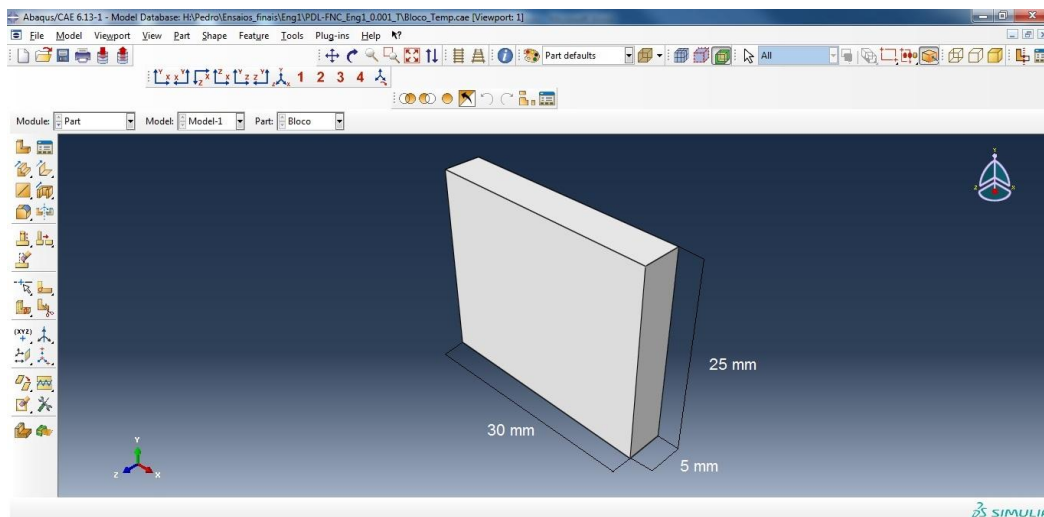


Figure 3.17 – Rectangular block created in the Part Module.

In this preliminary analysis, the cycle studied was the one referring to the flight-route PDL-FNC, and all the flight cycle periods used were based on the data in **Table 3.4**.

Using the Property Module, the properties obtained in section 3.3.3., as seen in **Table 3.15**, **Table 3.16** and **Table 3.17**, were listed and then, after creating a solid homogeneous section called S-

Bloco, for the properties and geometries of the part, these were all assembled in the Assembly Module.

- **Thermal Analysis**

Knowing the importance of the temperature distribution across the HPT blade and the way it affects the overall stress in it, a thermal analysis was conducted on the rectangular block model.

Using the Step Module, two steps were created, the Initial Step, automatically created by Abaqus CAE at the beginning of the analysis, and, for the thermal analysis, a transient heat-transfer operation step, in order to capture the changes in temperature at all points of the rectangular block model.

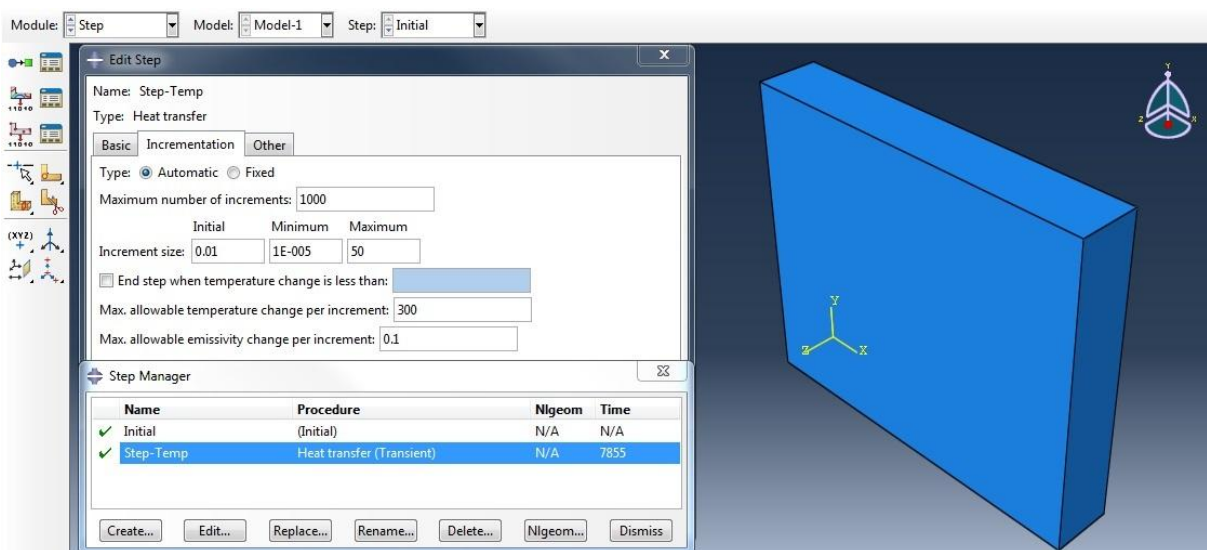


Figure 3.18 – Definition of analysis steps in the Step Module.

As can be seen in **Figure 3.18**, the second step, identified as Step-Temp, was set to last 7855 seconds, the cycle period with cooling set in **Table 3.4**, as opposed to the total cycle period, used in the blade model. This is because, as will be seen in the next chapter, after the cooling period, the difference between the surface and interior temperatures in the rectangular block model was low enough to forgo the 195 second extra cooling period. The incrementation shown in **Figure 3.18**, as well as the maximum allowable temperature change per increment, were chosen in accordance with the temperature behavior of the TIT plot in **Figure 3.5 a)**, and both initial and minimum time increments were chosen based on convention for this sort of analysis.

Using the Load Module, both thermal boundary conditions and prescribed fields were created to simulate the thermal loading on the model's surface. As seen in **Figure 3.19**, in the Initial Step, a predefined field was created on the entire part in order to define its initial temperature at 20 °C.

In order to simulate the temperature variation between the surface and the interior of the part, during the flight cycle, a boundary condition was created in the second step, as can be seen in **Figure 3.20**. The TIT plotted data was used and named Amp-Temp_Eng1_PDL-FNC, and, given the fact that

the air flow data was unknown, no heat transfer coefficients were used, and the surface temperatures in all the faces of the rectangular block, with the exception of its base which was considered to not be in contact with the hot gas flow, were made to vary along the TIT plot.

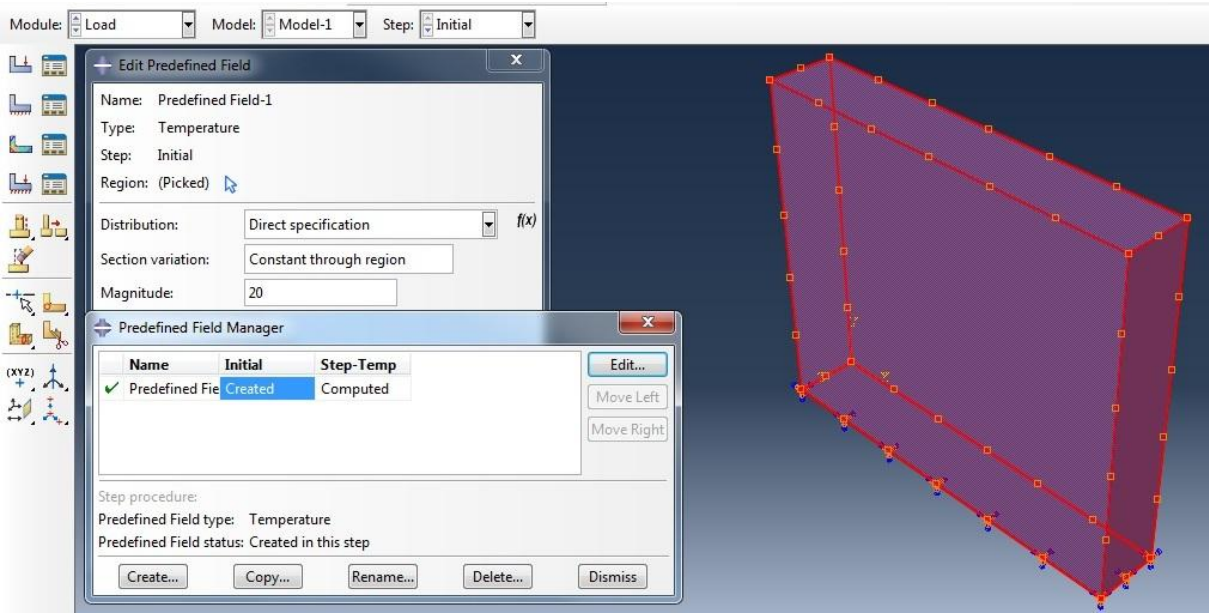


Figure 3.19 – Predefined field created using the Load Module.

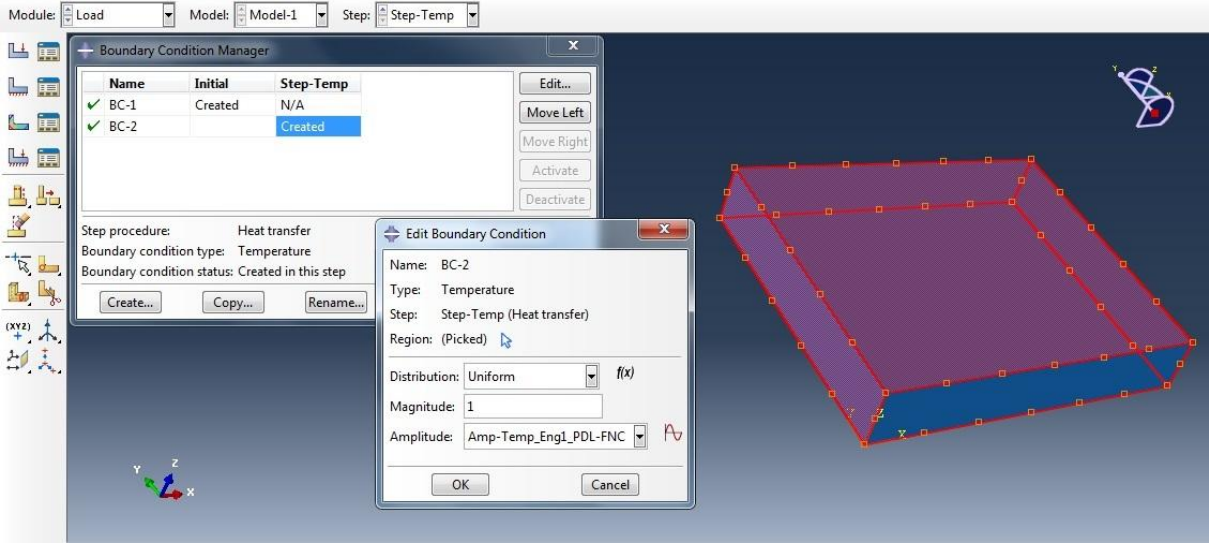


Figure 3.20 – Boundary condition applied on the surface of the rectangular block.

In the Mesh Module, the mesh size and element types were specified for this analysis. In a first instance, second order hexahedral (DC3D20: A 20-node quadratic heat transfer hexahedron) element for the rectangular block model was used. However, this element turned out not to be suitable for the analysis of the blade model, thus a second order tetrahedral (DC3D10: A 10-node quadratic heat transfer tetrahedron) element was used, given the need to have the same type of mesh in both the rectangular block and blade models in order to validate the methodology used.

Given its flexibility and applicability in the creation of meshes for parts with highly complicated geometrical shapes, the free meshing technique was used to automatically generate both the rectangular block and blade meshes.

As can be seen in **Figure 3.21**, the rectangular block was seeded with an approximate global size of 1 mm. The choice of this seed size was based mostly on computational limitations.

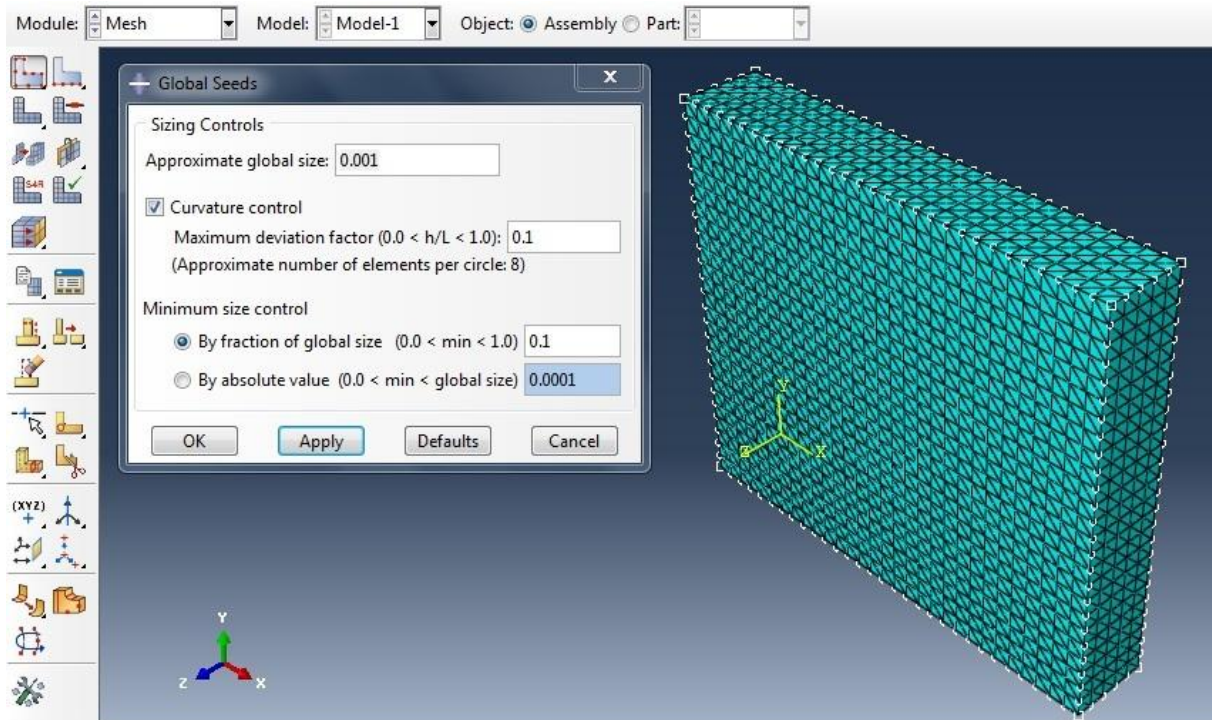


Figure 3.21 – Definition of seed size in the Mesh Module.

Finally, the simulation was conducted using the Job Module, where a job titled Job-TempB was ran, and the results obtained, seen in the Visualization Module, will be the subject of the result analysis chapter.

- **Mechanical Analysis**

Using the nodal temperature distributions obtained from the heat transfer analysis as well as the variation in rotational speed during the flight cycle, a mechanical analysis was conducted, where the centrifugal forces experienced by the blade which impose stress were studied, although the hot gas pressure influence and its effects on the mechanical behavior of the part were neglected, for the reasons explained earlier in this paper.

Following the same methodology as before, two different types of mechanical analysis were performed, a purely elastoplastic analysis, and an analysis considering the creep properties of the material.

- **Elastoplastic Analysis**

In the Step Module, instead of creating a transient heat-transfer operation step, the second step was created as a static, general step, with the same incrementation and duration for the second step used in the thermal analysis, and titled Step-Cent.

Using the Load Module, first the load applied on the part is defined, as seen in **Figure 3.22**, as a rotational body force to be applied to the entire rectangular block during the second step, with the rotation axis located 111 mm below the base, i.e. the HPT disc radius obtained in section 3.3.1., and centered along the 5 mm thickness of the rectangular block. This is a centrifugal load defined using the angular velocity plot obtained earlier, and is titled Amp-Cent_Eng1_PDL-FNC.

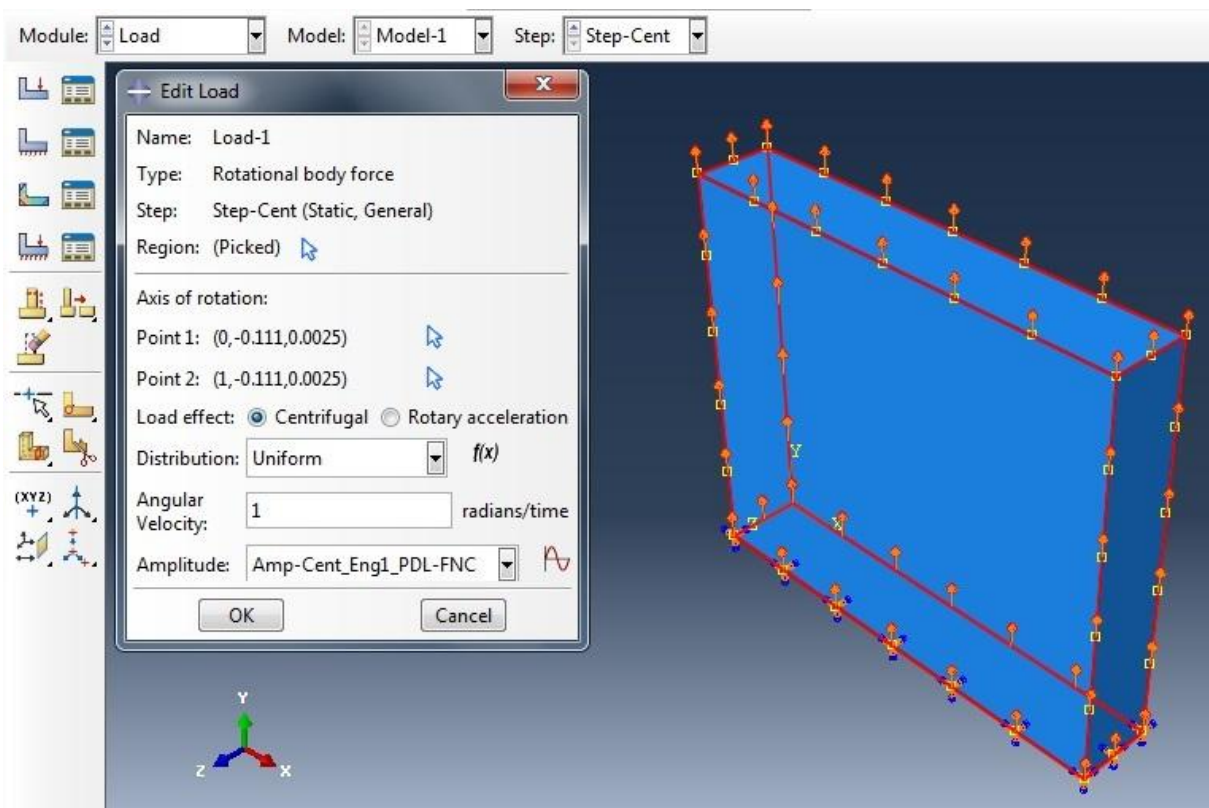


Figure 3.22 – Definition of centrifugal load using the Load Module.

Afterwards, the boundary conditions were defined in the initial step and propagated into the second step, as seen in **Figure 3.23**, where the base of the rectangular block was encastred.

As for the predefined fields, the initial step was exactly the same as in the thermal analysis, yet, in the second step, instead of creating a thermal boundary condition upon the rectangular block's surfaces, the temperatures of the thermal analysis were imported, as can be seen in **Figure 3.24**, from the Job-TempB results file.

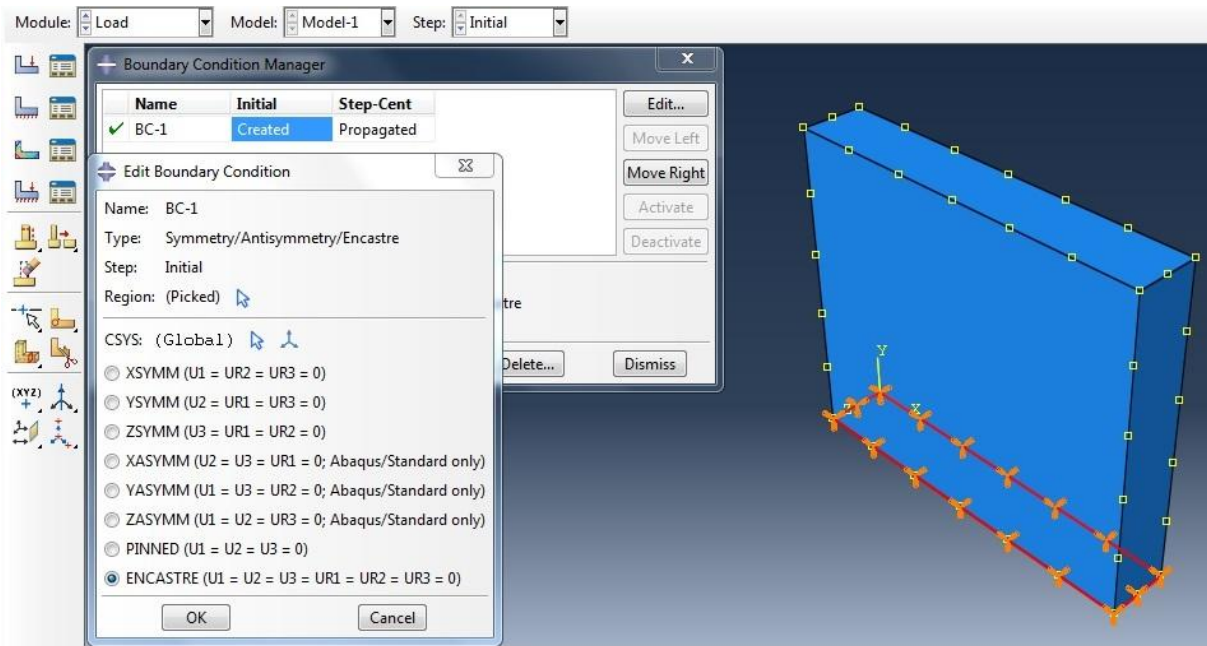


Figure 3.23 – Definition of boundary condition in the Load Module.

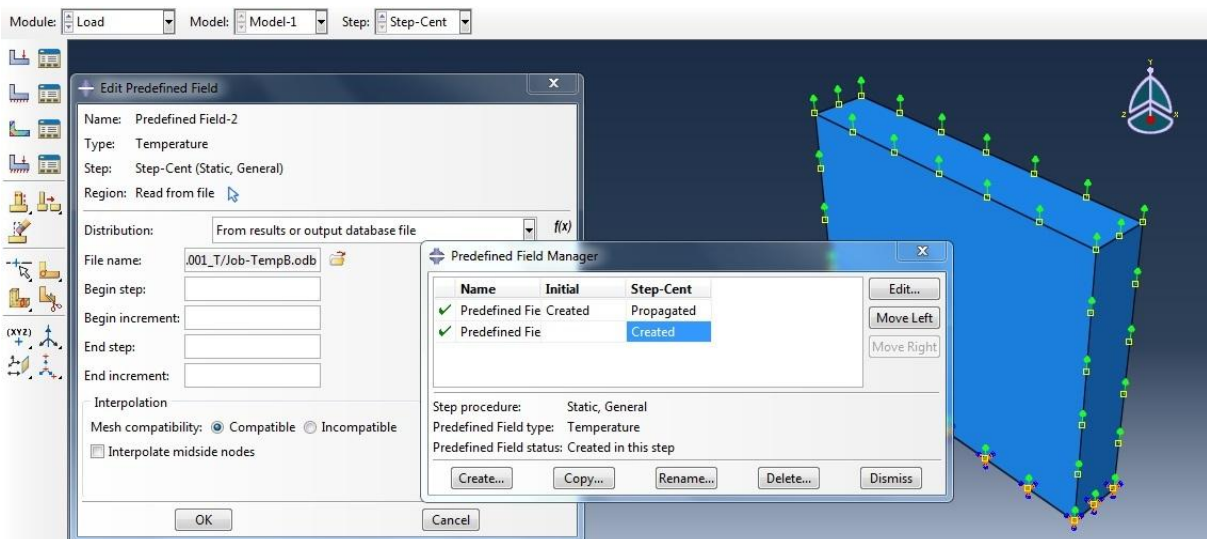


Figure 3.24 – Definition of Predefined Field-2 in Step-Cent.

Considering the need for compatibility expressed in **Figure 3.24**, in the Mesh Module, the part was meshed in exactly the same way, with the exception of the element, which was now a second order tetrahedral (DC3D10: A 10-node quadratic 3D stress tetrahedron) element.

Finally, the simulation was conducted using the Job Module, where a job entitled Job-CentB was ran, and the results obtained.

- **Creep Analysis**

The only difference between the creep analysis and the elastoplastic analysis was in the definition of the second step, where the static, general step was replaced by a visco step, where the creep properties were taken into account.

This time around, the analysis conducted in the Job Module was titled Job-CreepB.

- **Isothermal Analyses**

In order to evaluate the influence of the variation of temperature along the interior of the rectangular block, two different isothermal analyses were conducted, one within the elastoplastic analysis and the other in the creep analysis.

For both cases, the only difference was in the definition of the predefined field in the second step, using the Load Module. As can be seen in **Figure 3.25**, the TIT plotted data, Amp-Temp_Eng1_PDL-FNC, was used and applied to the entirety of the rectangular block, instead of being applied only to its outer surfaces. In this way, for both the inelastic as well as the creep analysis, the thermal analysis results were not used and the part was considered isothermal.

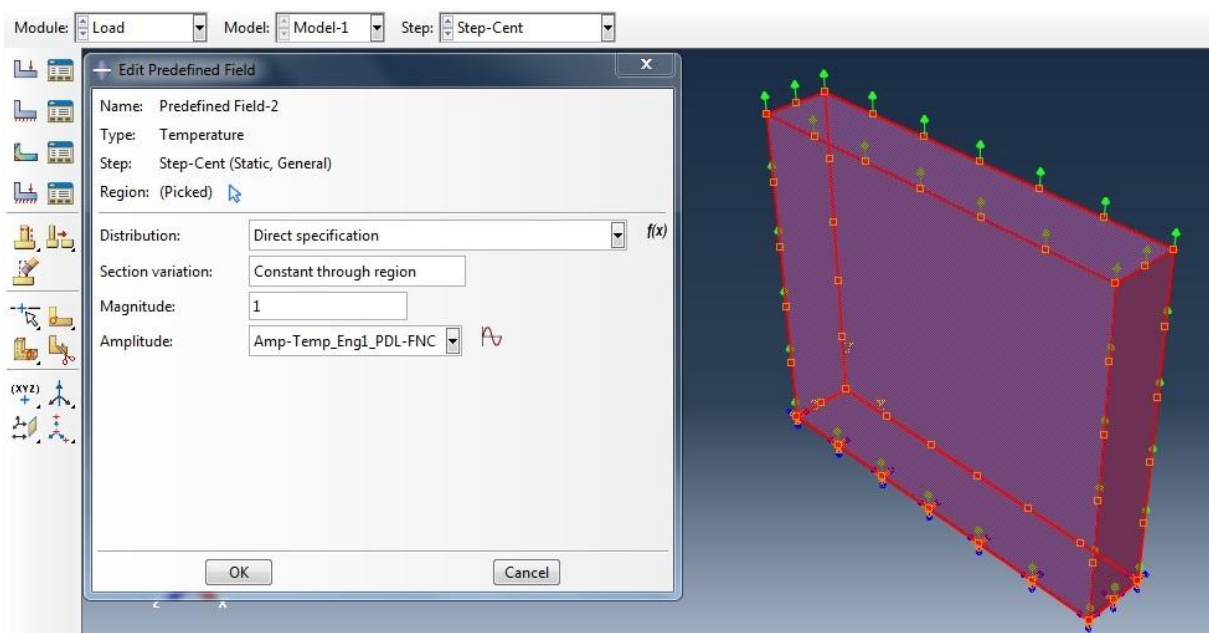


Figure 3.25 – Definition of predefined field for isothermal analyses in the Load Module.

3.4.2. Blade Model

Once the methodology in the previous section was deemed appropriate, the same analyses were performed on the blade model, with differences in some of the phases of the analysis.

In the Part Module, the blade model created in section 3.3.1. was imported as an .IGS as can be seen in **Figure 3.26 a**).

Using the Assembly Module, the part was repositioned in order for the axis of rotation to be properly placed when defining the centrifugal load in the Load Module, and a second coordinate system was introduced in order for the boundary conditions to be defined in the load module, as can be seen in **Figure 3.35 b)**.

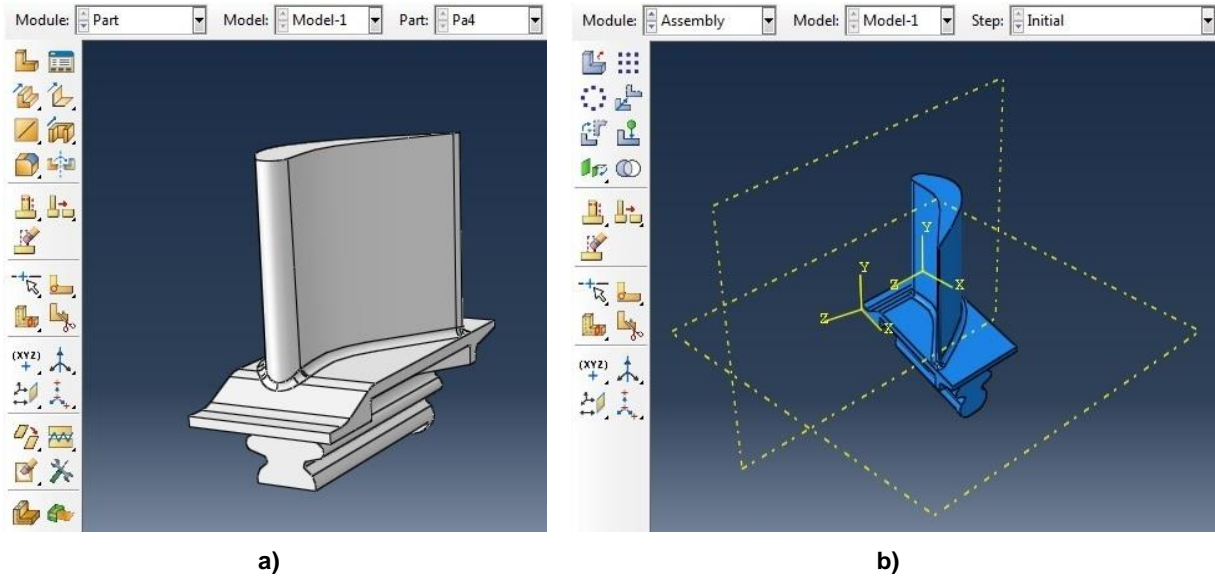


Figure 3.26 – a) Imported blade model; b) Repositioned blade model and secondary coordinate system.

- **Thermal Analysis**

As with the rectangular block model, in the thermal analysis of the blade model, two steps were created. However, this time, the second step was set to last 8050 seconds, the total cycle period set in **Table 3.4**. This is because, as will be seen in the next chapter, after the cooling period, the difference between the surface and interior temperatures in the blade model requires the 195 second extra cooling period in order for the whole part to be at approximately 20 °C.

In the Load Module, as was the case with the rectangular block model, in the initial step, a predefined field was created on the entire part in order to define its initial temperature at 20 °C.

In the second step, a boundary condition was created, and, as seen in **Figure 3.27**, on the surfaces in contact with the hot gas flow, and the same TIT plotted data was used and named Amp-Temp_Eng1_PDL-FNC.

When meshing the blade model in the Mesh Module, the same element and techniques applied in the rectangular block model were used, but, due to limitations of the free meshing technique for this specific geometry, the 1 mm seed used in the previous model couldn't be used, thus the seed size used was the one recommended for this part, i.e. 1.4 mm.

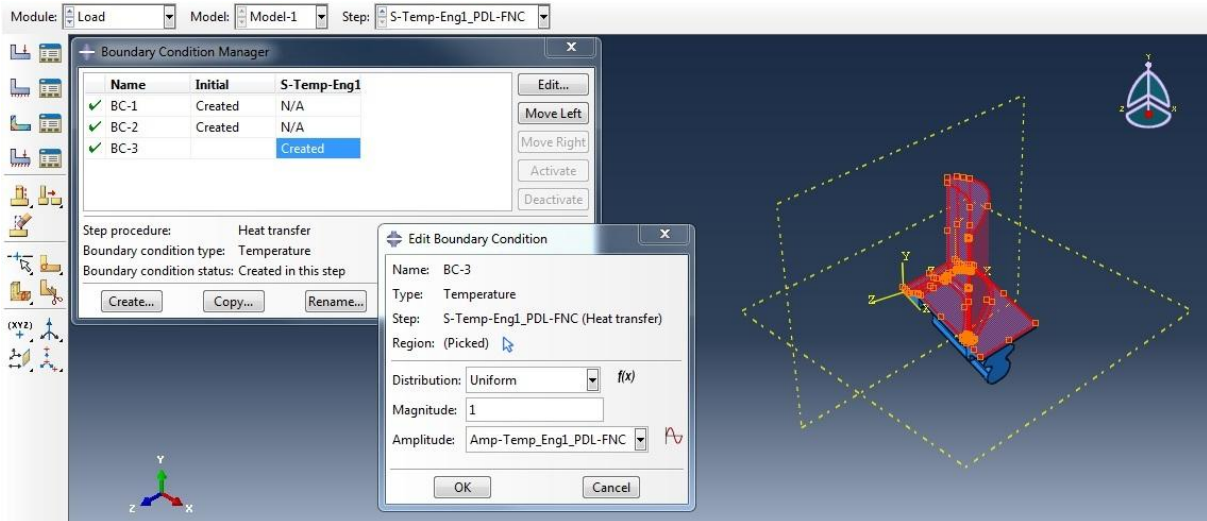


Figure 3.27 – Thermal boundary condition on surface of blade model.

- **Mechanical Analysis**

The methodology for the mechanical analysis, in all its four different facets, i.e. creep analysis, elastoplastic analysis, isothermal creep analysis and isothermal elastoplastic analysis, was basically the same applied to the rectangular block model, with the differences outlined below.

Following the same steps described in the rectangular block model, the steps created in the Step Module would only change in the sense that the second step was set to last 8050 seconds, the total cycle period.

Beyond that, the remainder variations regarding the methodology used before occurred in the definition of load and boundary conditions in the Load Module. As seen in **Figure 3.28**, the centrifugal load was the same as the one applied to the rectangular block model, yet, this time around, the location of the rotation axis was centered along the midpoint of the largest dimension shown in **Figure 3.12**, i.e. $b = 24.43$ mm.

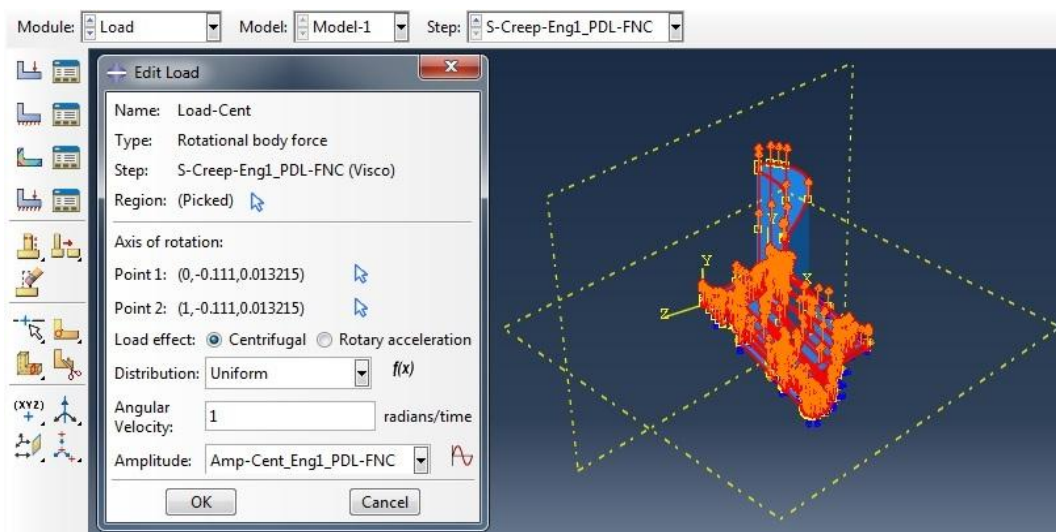


Figure 3.28 – Definition of centrifugal load using the Load Module.

Given the complexity of the part, four different boundary conditions had to be defined separately, in order to simulate the way the actual HPT blade is seated on the HPT disk as well as the way in which the blades are set against each other, as can be seen in **Figure 3.29** through **Figure 3.32**.

Finally, regarding the mesh, the same elements as the ones used in the rectangular block model were once again used, but the seed size was also changed from 1 mm to 1.4 mm, for the same reasons stated above.

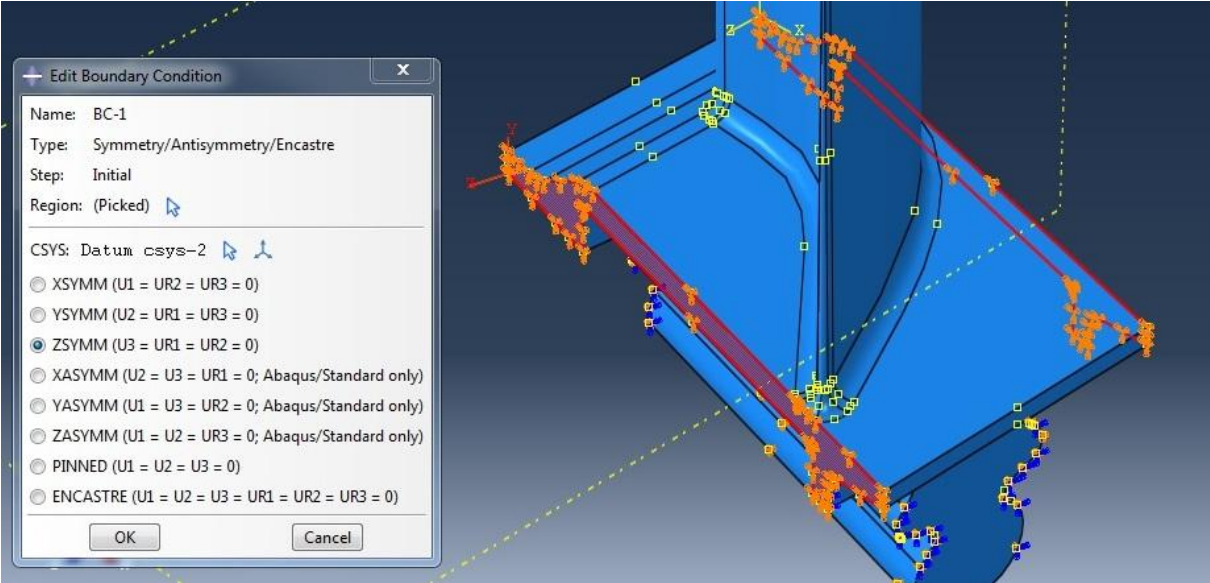


Figure 3.29 – Faces constrained normal to contact faces (ZZ axis).

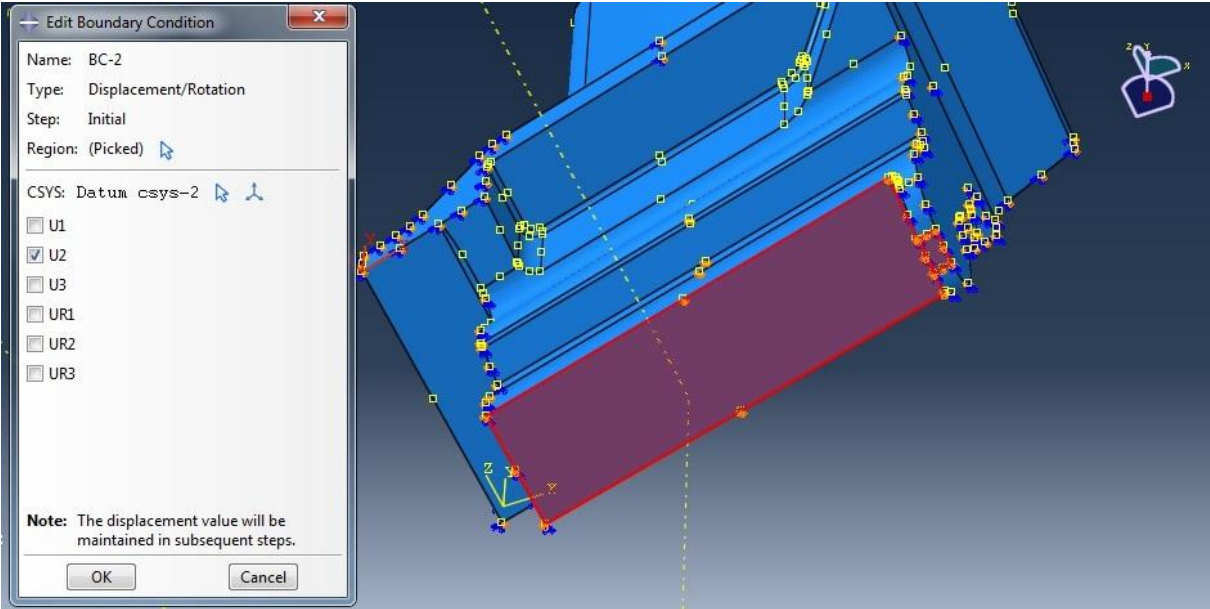


Figure 3.30 – Faces constrained normal to the vertical direction (YY axis).

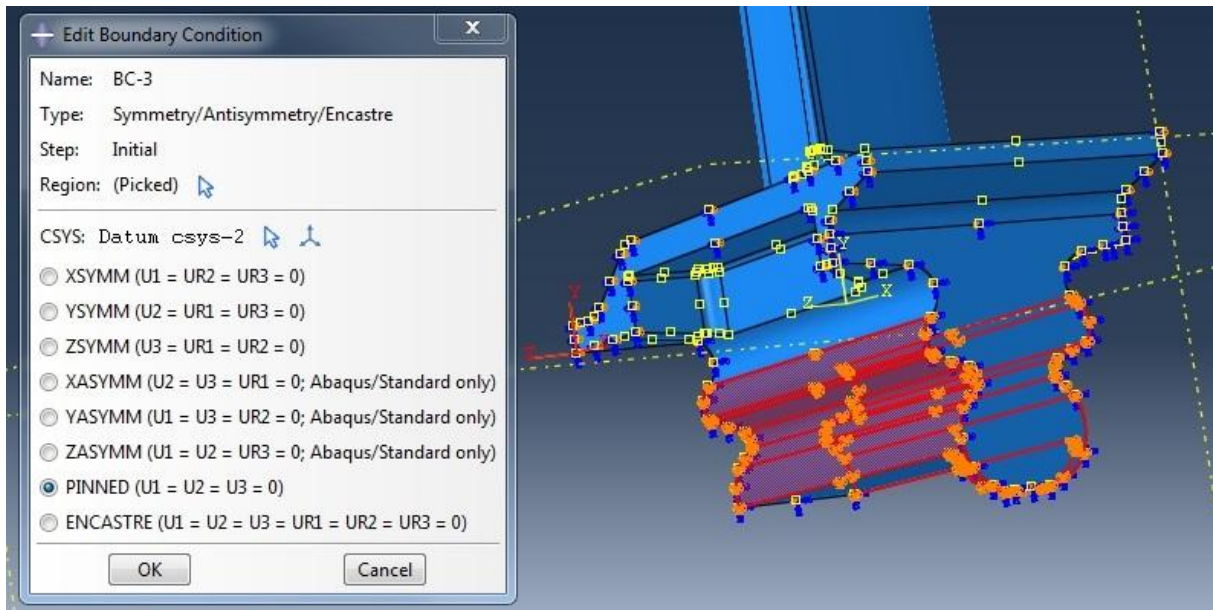


Figure 3.31 – Faces pinned along all directions.

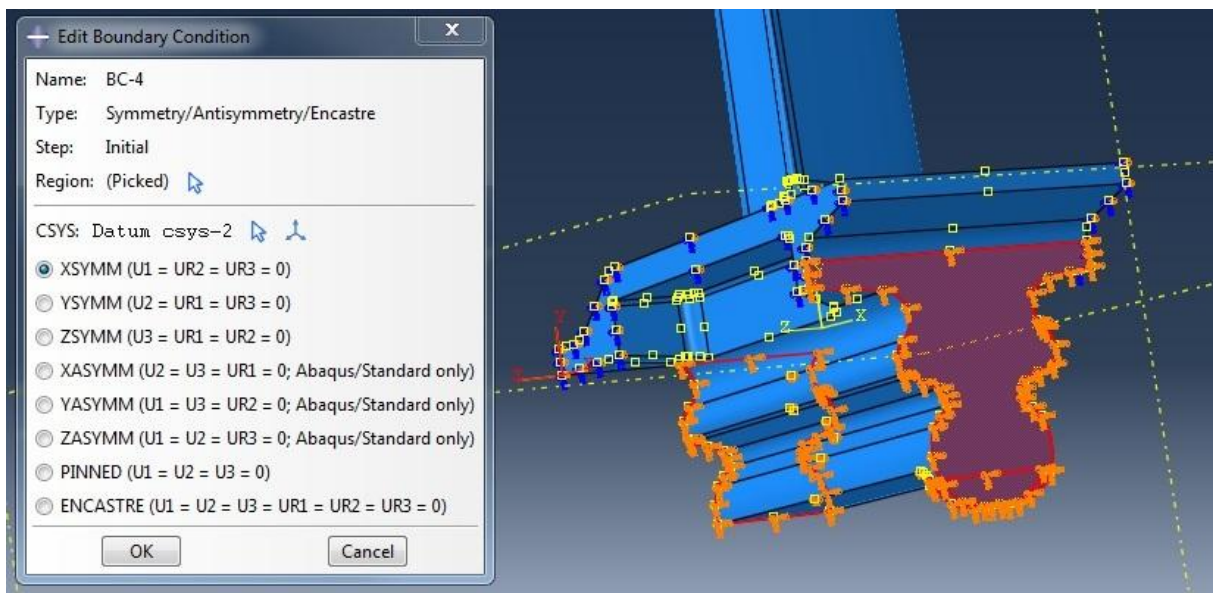


Figure 3.32 – Faces constrained along the axial direction (XX axis).

4. Results and Discussion

Following the methodology presented in the previous sections, several numerical experiments were conducted upon the rectangular block model as well as the blade model. For both models comparisons between the elastoplastic, creep, isothermal elastoplastic and isothermal creep analyses were performed.

In the blade model, the three different flight cycles presented in **Table 3.4** were studied and compared, and a simplified lifetime analysis was done in order to evaluate the displacement of the blade at selected points after the period of 3000 hours of service.

In order to analyze not only the mesh refinement as well as to extract clear results, both for the rectangular block and blade models, 7 nodes were chosen, as can be seen in **Figure 4.1**.

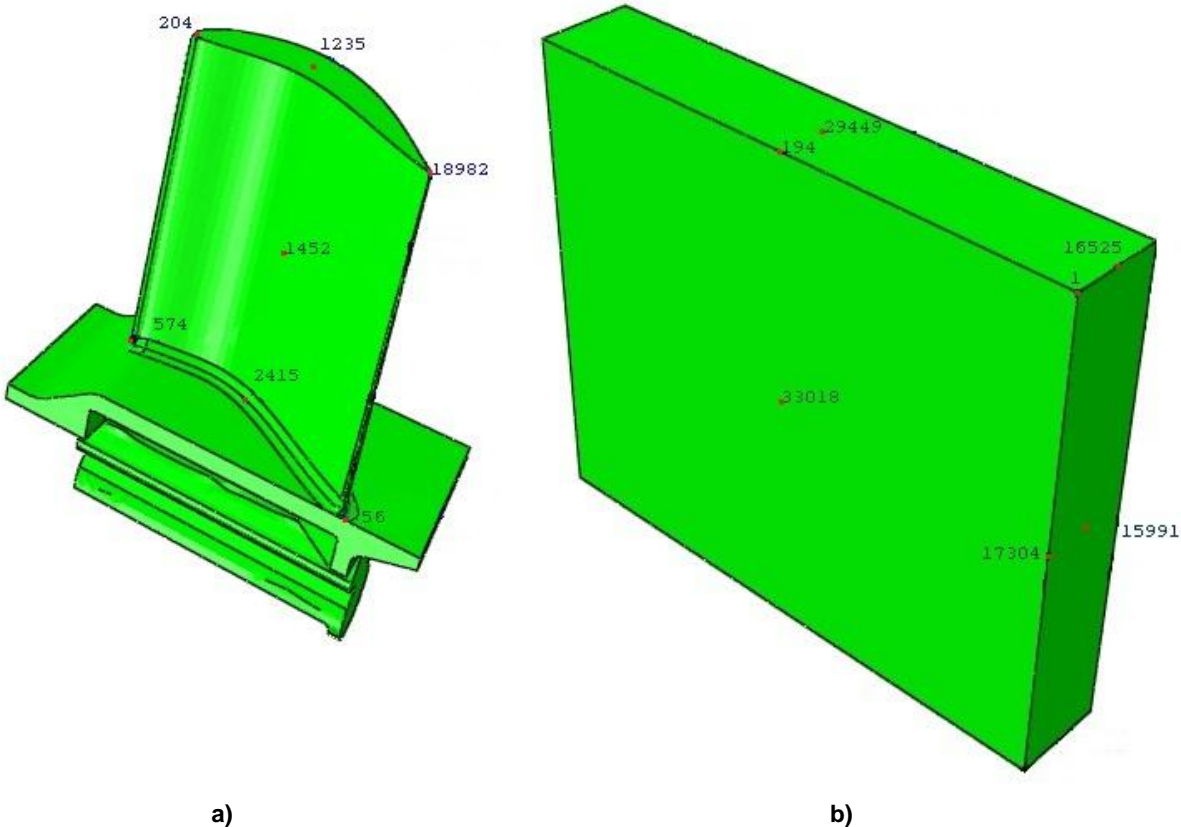


Figure 4.1 – Nodes selected for a) the blade model; b) the rectangular block model.

The study of the mesh and errors associated with the use of different sizes of mesh elements was conducted and can be seen in **Appendix B**.

4.1. Thermal Analysis Results

While conducting the different simulations, the first concern was the need to obtain a realistic behavior on the part of the material for both the rectangular block and blade models during the thermal analysis.

In the case of the rectangular block model, **Figure 4.2 a)** shows the distribution of temperature at the end of the PDL-FNC flight cycle, where the period considered is 7855 seconds, i.e. the cycle period with cooling. Considering that the 195 second stabilization period was not applied, the difference between the surface temperature, 20 °C, and the core temperature, at about 21.25 °C, was considered not particularly influential for the mechanical analyses conducted later, given the high temperature gradients experienced in this cycle and the low probability of the influence of 1 °C in the overall stress distribution.

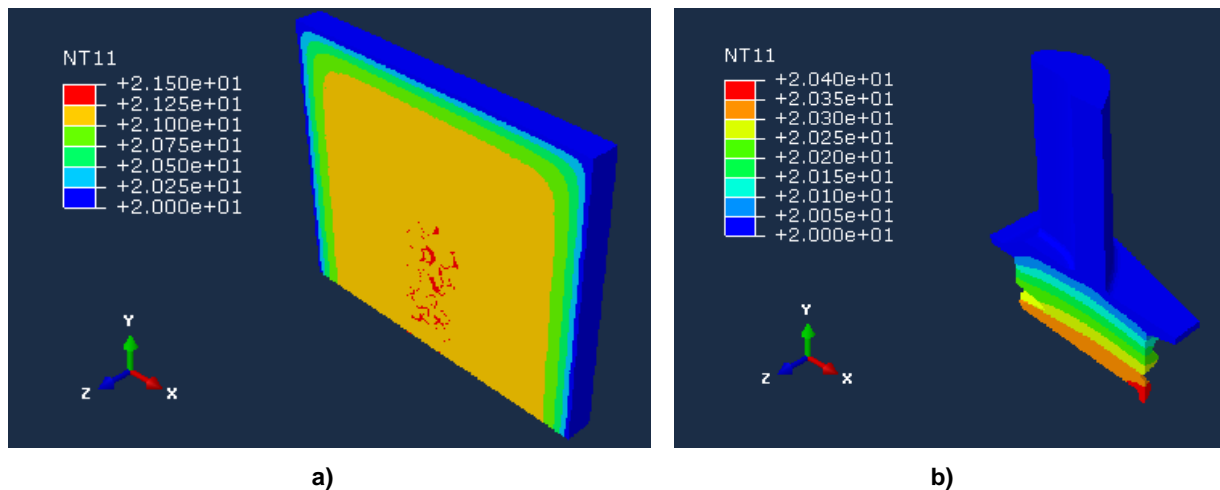


Figure 4.2 – Temperature distribution model with midsection cut along the XY plane for a) the rectangular block model; b) the blade model.

In the case of the blade model, the 195 second stabilization period was used due to need to best simulate reality as possible, i.e. to have the entire blade cooled to a temperature of 20 °C.

As can be seen in **Figure 4.2 b)**, the distribution of temperature at the end of PDL-FNC cycle is as expected. Nonetheless, there is still a small temperature gradient, also seen in the rectangular block model. This is because, for both models, when defining the boundary conditions simulating the interaction between the hot gas flow and the surface of the part, the surfaces not selected are automatically considered insulated by the software.

This, of course, is not representative of the reality, given that some blade surfaces interact with other blades, as well as with the HPT disk. However, given the complexity of establishing such interactions in terms of thermal conductivity, both between the blades base and the disk which was not modeled, the simplification was considered acceptable for the overall temperature distribution.

The temperature distribution during one PDL-FNC cycle for both the rectangular block and the blade model can be seen in more detail in **Appendix C**.

4.2. Analyses Comparison

Even considering the errors associated with using a coarser mesh with a seed size of 1mm for the rectangular block model, when comparing different results within the same type of mesh, consistency between different analyses' results is expected.

Thus, one of the first things studied was the influence of considering the part isothermal, as opposed to considering the temperature variation and distribution between the part's surface and core, as well as the difference between the part behavior when comparing elastoplastic to creep conditions. The results after a single PDL-FNC flight cycle for the different nodes as well as the overall distribution of vertical stress, displacement and strain can be seen in **Table 4.1** and **Figure 4.3** through **Figure 4.5**.

Table 4.1 – Nodal results for one PDL-FNC flight cycle.

| Analyses Results | Units | Node | | | | | | |
|---------------------------------|-------|---------|---------|---------|---------|---------|---------|---------|
| | | 33018 | 94 | 29449 | 1 | 16525 | 17304 | 15991 |
| Creep | | | | | | | | |
| S22 | (Pa) | 2.3E+7 | -1.2E+5 | 2 E+3 | 8.3E+4 | 3.5E+4 | -7.9E+7 | -8 E+7 |
| U2 | (m) | -5.7E-6 | -4.7E-6 | -4.7E-6 | 2.2E-7 | 1.9E-7 | 2.3E-6 | 2.3E-6 |
| E22 | (-) | -7.5E-6 | 1.1E-4 | 1.1E-4 | 6.9E-7 | 1.2E-6 | -4.3E-4 | -4.4E-4 |
| Isothermal creep | | | | | | | | |
| S22 | (Pa) | 2.1E+7 | -6E+4 | -8.1E04 | 1.4E+5 | 6.4E+4 | -8.1E+7 | -8.3E+7 |
| U2 | (m) | -6 E-6 | -5 E-06 | -5 E-06 | -2.4E-8 | -5.2E-8 | 2.2E-6 | 2.2E-6 |
| E22 | (-) | -1.5E-5 | 1.2E-4 | 1.2E-4 | 1.1E-6 | 2.7E-6 | -4.4E-4 | -4.6E-4 |
| Elastoplastic | | | | | | | | |
| S22 | (Pa) | 2 E+7 | -1.1E+5 | -6.8E+2 | 7.6E+4 | 2.9E+4 | -7 E+7 | -7.2E+7 |
| U2 | (m) | -6.8E-6 | -5.7E-6 | -5.7E-6 | -4.8E-7 | -5.1E-7 | 1.8E-6 | 1.8E-6 |
| E22 | (-) | -1.4E-5 | 1.3E-4 | 1.3E-4 | 6.4E-7 | 1.3E-6 | -4.8E-4 | -4.9E-4 |
| Isothermal elastoplastic | | | | | | | | |
| S22 | (Pa) | 1.8E+7 | -5 E+4 | -8.3E+4 | 1.4E+5 | 5.7E+4 | -7.2E+7 | -7.4E+7 |
| U2 | (m) | -7 E-6 | -6.0E-6 | -6 E-06 | -7.1E-7 | -7.4E-7 | 1.7E-6 | 1.6E-6 |
| E22 | (-) | -2.3E-5 | 1.3E-4 | 1.4E-4 | 1 E-06 | 2.8E-6 | -4.9E-4 | -5.1E-4 |

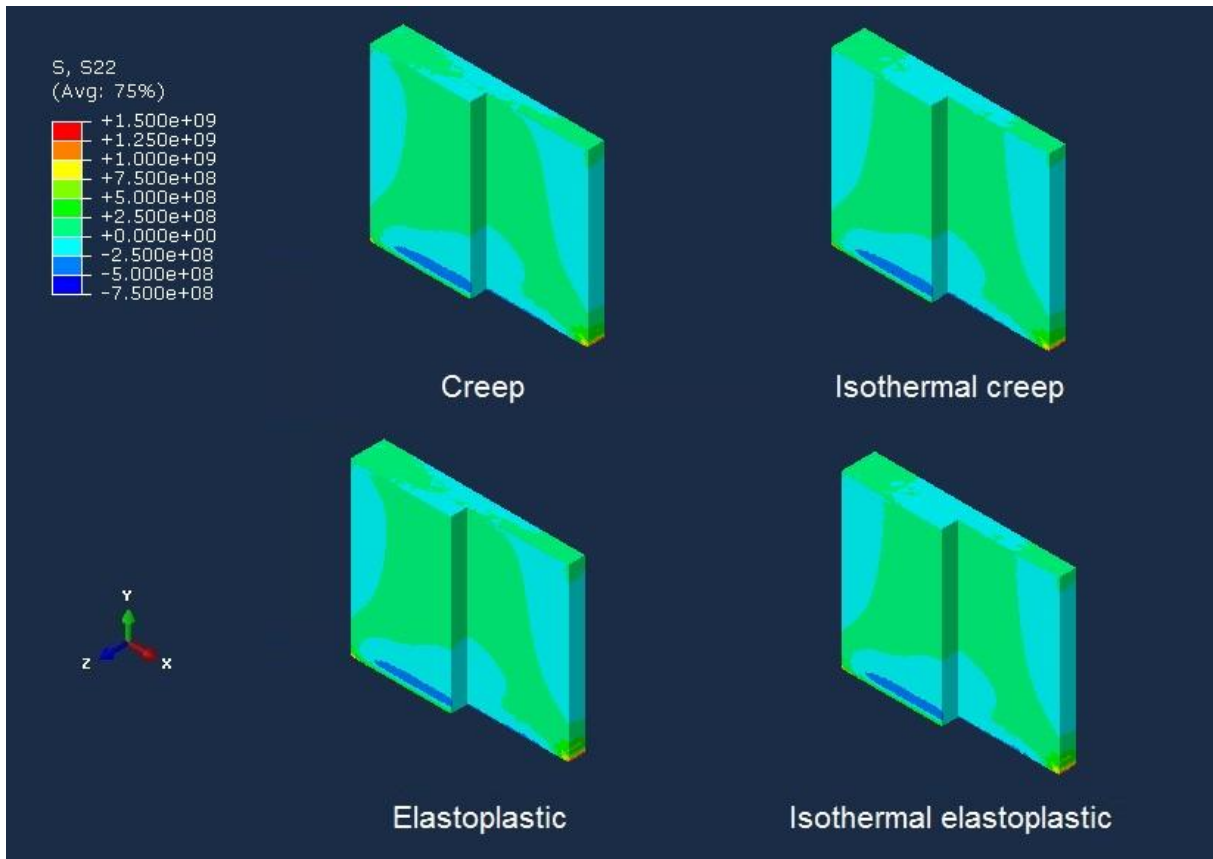


Figure 4.3 – Stress (S22) distribution for the four analyses performed.

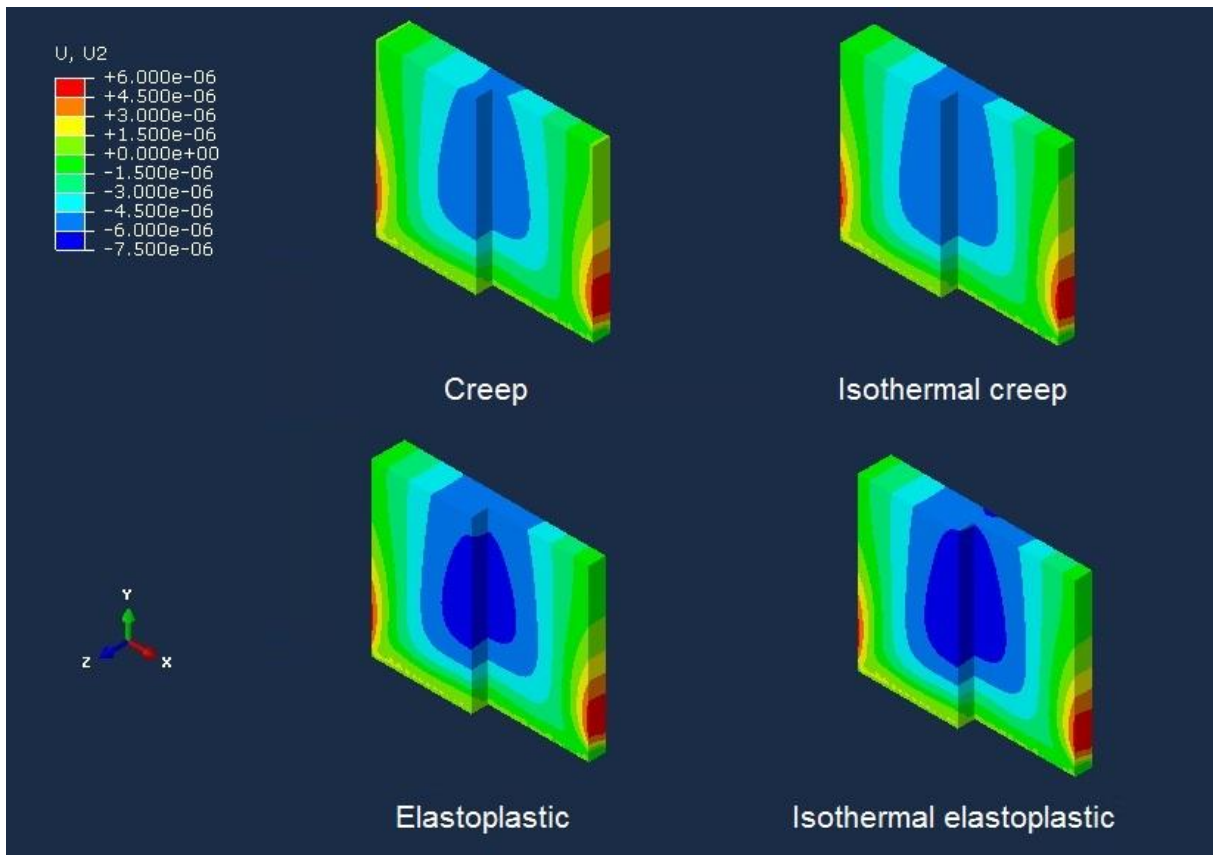


Figure 4.4 – Displacement (U2) distribution for the four analyses performed.

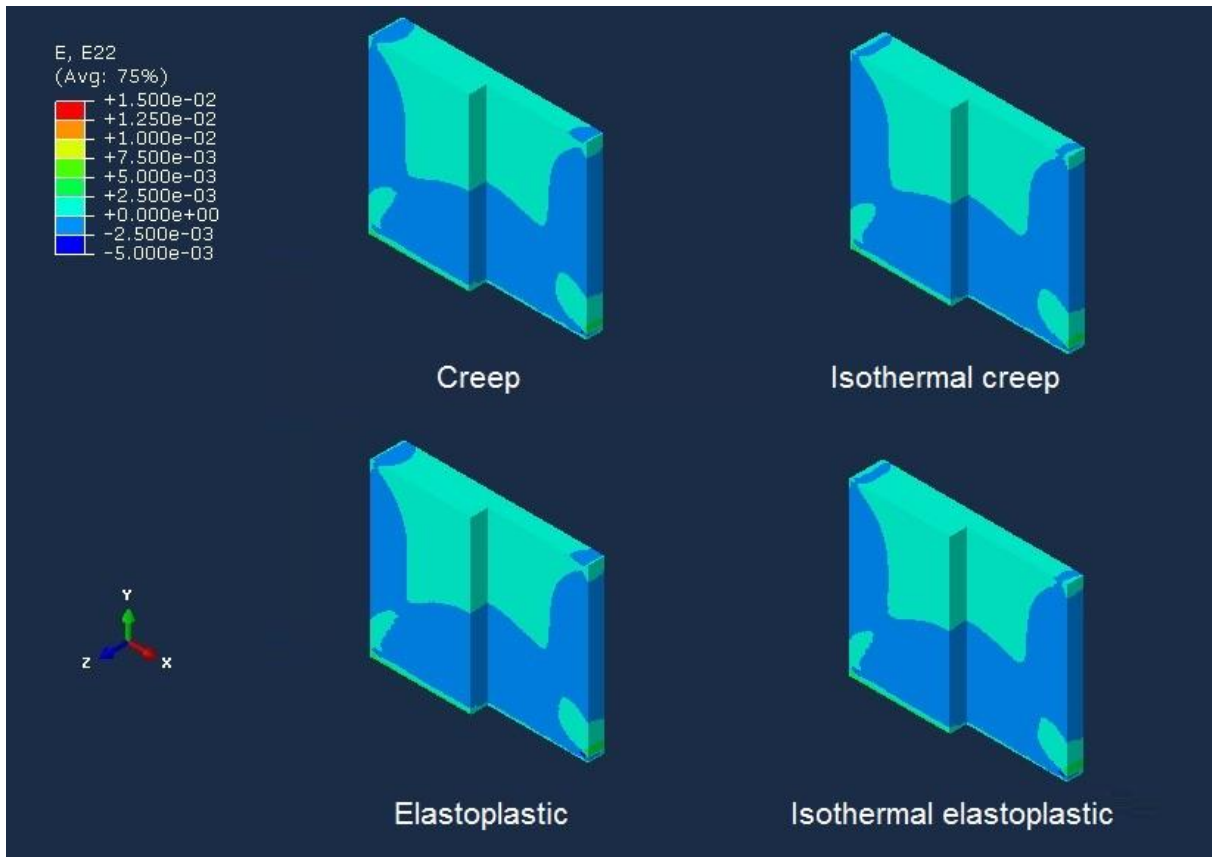


Figure 4.5 – Strain (E22) distribution for the four analyses performed.

As can be seen in **Table 4.1** and in **Figure 4.3** through **Figure 4.5**, the simulation of a flight cycle while disregarding the temperature distribution for one cycle yields slightly different overall distributions in terms of stress and strain. However, it shows more noticeable changes in terms of vertical displacement of the part. Considering that this analysis is made for only one cycle and that in reality the part is expected to perform between 1342 and 5269 cycles, this difference must be taken into account. Thus, the temperature distribution along the part must not be ignored, i.e. the part must not be considered isothermal.

A comparison between the elastoplastic and creep behavior for both the rectangular block and blade models was further studied in the next section. However, a simple look at the vertical displacement distribution in **Figure 4.4** can tell us that, adding up more and more cycles, this difference, along with the slight variations of overall stress and strain distributions, will increase greatly and quickly.

It is also important to note that, looking at **Table 4.1**, the differences in the node results, some greater than others, are telling of this trend.

4.3. Elastoplastic Analysis vs Creep Analysis

As mentioned in the previous section, the expected trend, in terms of results, was for there to be an increasing deviation between the results for creep and elastoplastic analyses as the number of

cycles increased. It has to be mentioned that the purpose of analyzing the parts behavior with a purely elastoplastic simulation, was to, above all else, help validate the creep model and the approach undertaken up to this point. Considering this, comparisons between these two analyses were performed for both the rectangular block and blade models.

For the rectangular block model, 10 PDL-FNC flight cycles were simulated in succession and the results for the distribution of S22, U2, and E22, can be seen below in **Figure 4.6** through **Figure 4.8**.

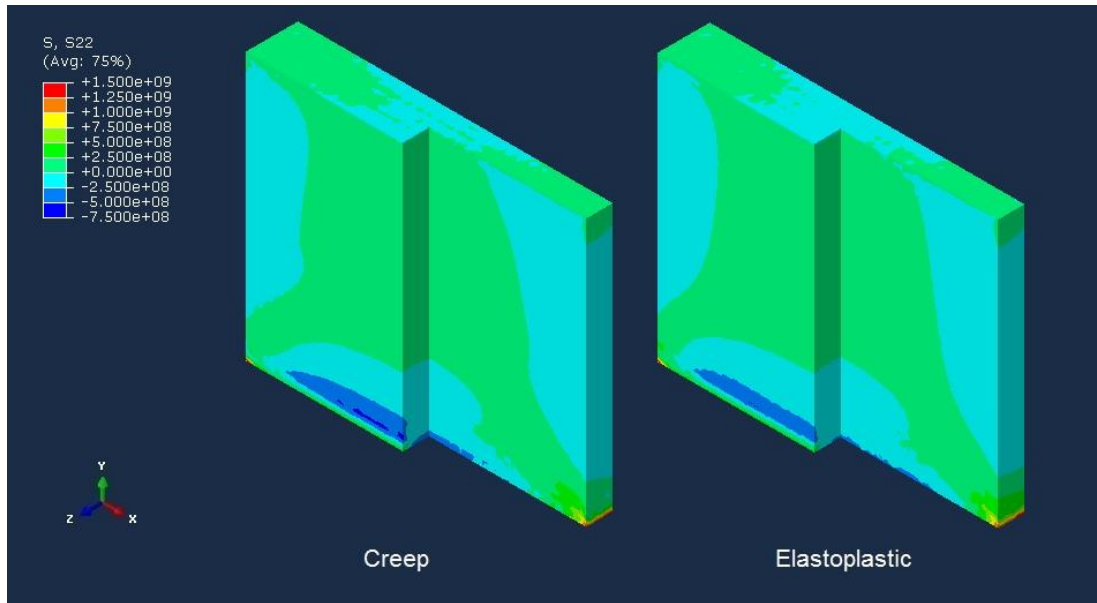


Figure 4.6 – Stress (S22) distribution after 10 PDL-FNC flight cycles.

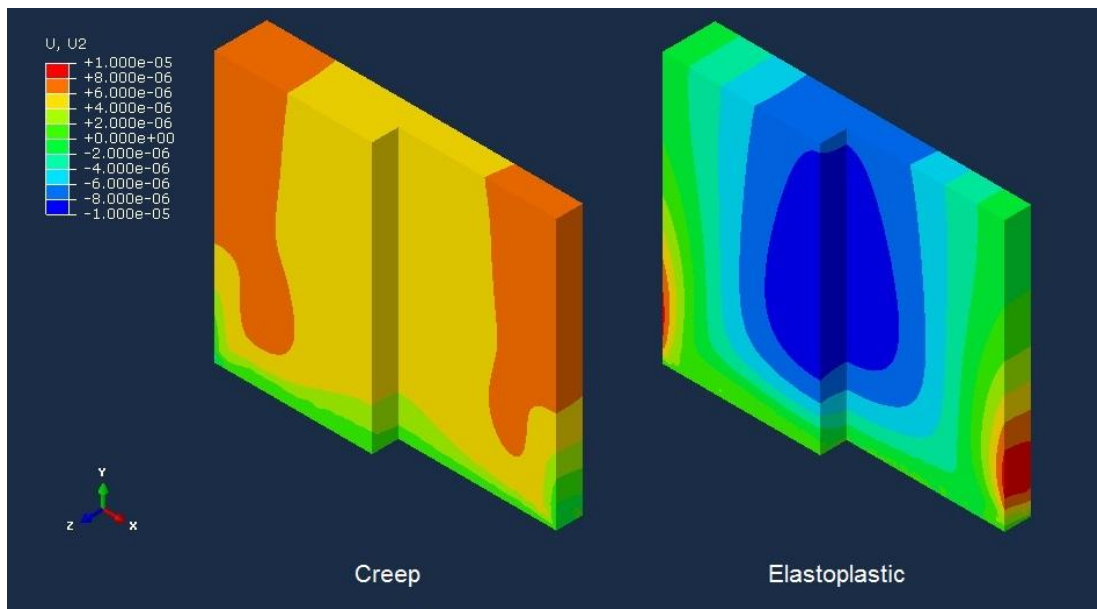


Figure 4.7 – Displacement (U2) distribution after 10 PDL-FNC flight cycles.

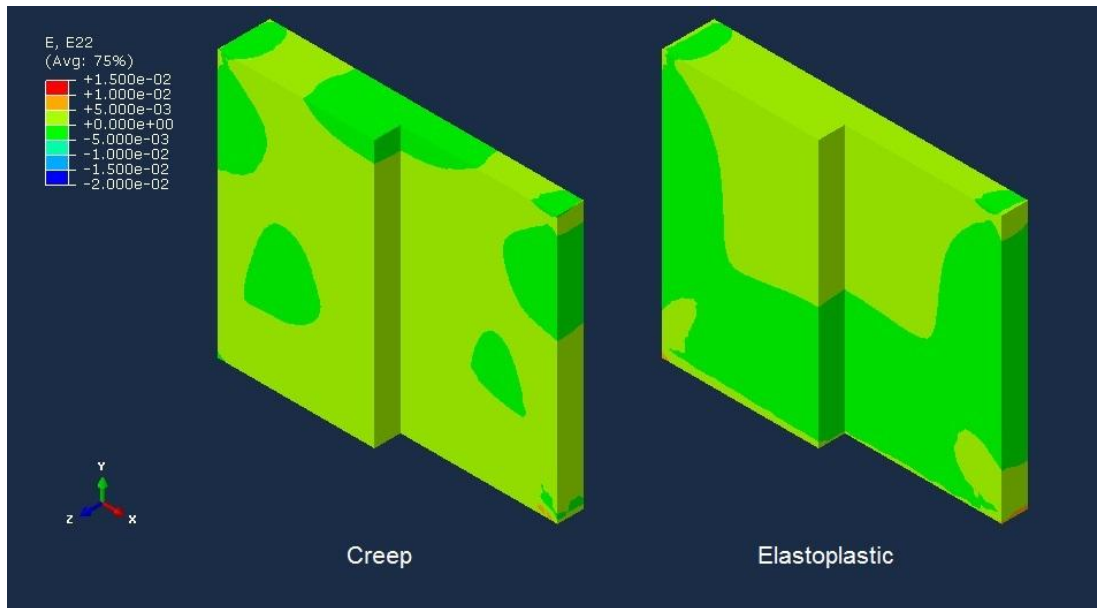


Figure 4.8 – Strain (E22) distribution after 10 PDL-FNC flight cycles.

As can be seen in **Figure 4.6** through **Figure 4.8**, although the differences in terms of S22 distribution are subtler when compared to the much more noticeable differences in both U2 and E22, they are still indicative of the greater amount of plasticity in the elastoplastic analysis, as opposed to the creep analysis, where some stress relaxation and increased deformation because of the presence of creep can be assumed.

As for the blade model, only 5 PDL-FNC flight cycles were able to be simulated in succession, the reasons why will be discussed later on in this section, and the results for the distribution of S22, U2, and E22, can be seen below in **Figure 4.9** through **Figure 4.11**.

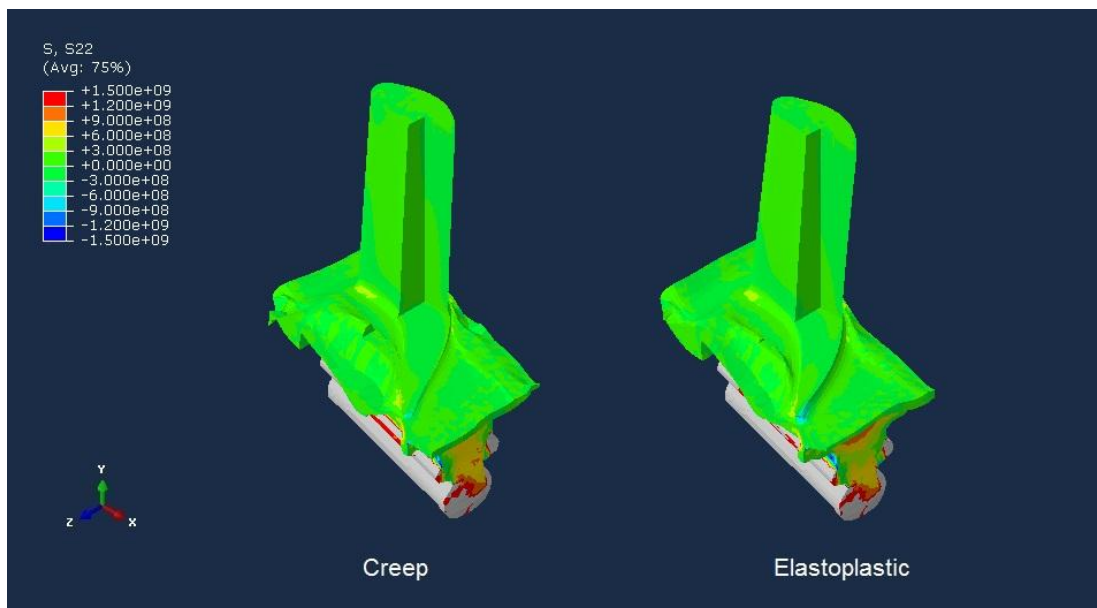


Figure 4.9 – Stress (S22) distribution after 5 PDL-FNC flight cycles.

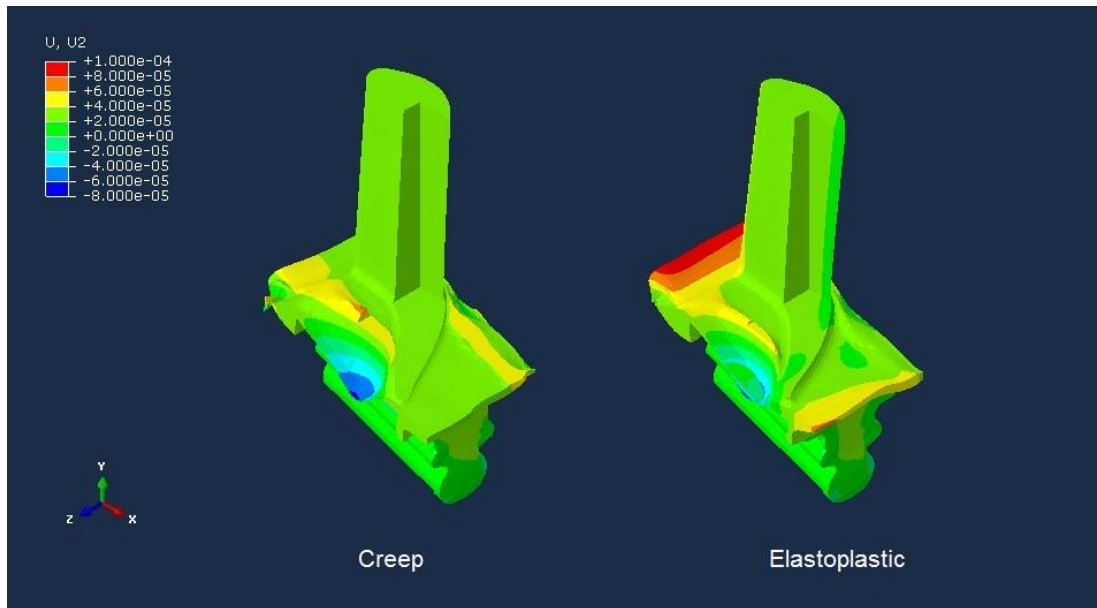


Figure 4.10 – Displacement (U2) distribution after 5 PDL-FNC flight cycles.

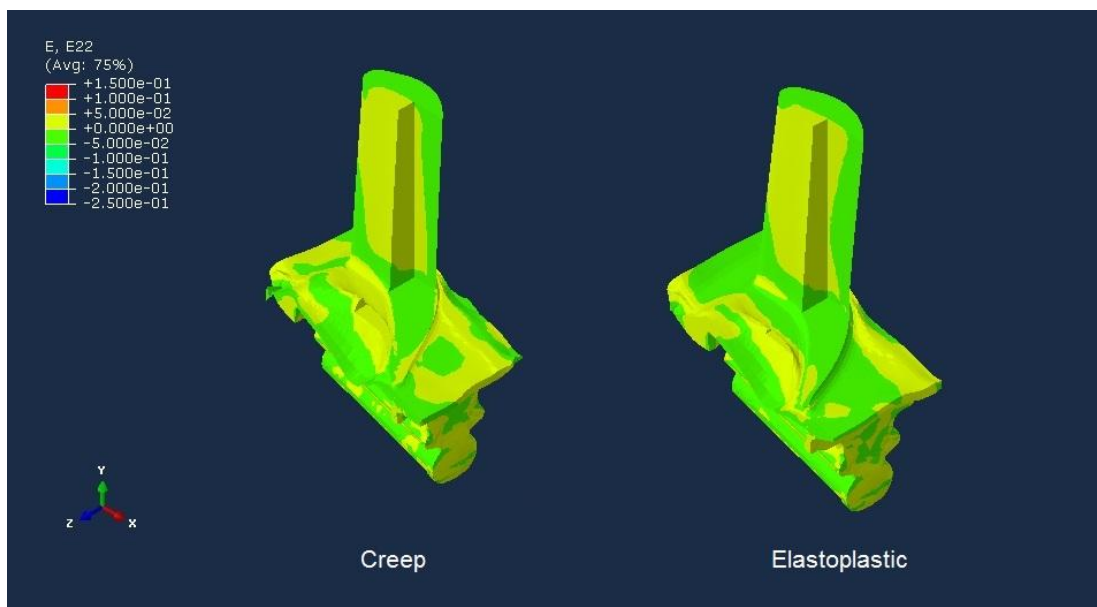


Figure 4.11 – Strain (E22) distribution after 5 PDL-FNC flight cycles.

In the case of the blade model, overall large differences in the distribution of stress, strain and displacement can be seen. As mentioned earlier, instead of running a simulation with 10 successive cycles, only 5 were ran, mainly due to the fact that, when running the elastoplastic analysis on the blade model, the software was unable to run further simulations beyond the fifth cycle due to convergence issues. Due to the onset of plasticity in the previous cycles, and considering that for temperatures between 750 and 850 °C, the ultimate tensile strength is between 1287 and 1179 MPa, respectively, as seen in **Figure 4.9**, it was reached during the fifth cycle. Although it does not influence the intended study, it is also important to note that the discoloration on the bottom of the HPT blade, i.e. where it connects to the HPT disk, stems from the problematic nature of the area, due to the constraints applied there and the software recognizing values of stress well above the material's

ultimate tensile strength, and should be viewed as a limitation in the model. This will be noticeable in the next section.

Thus, the methodology for the creep analysis with the blade model can be considered the best possible approximation to the behavior of a real HPT blade, within the available models presented.

4.4. Cycle Accumulation Analysis

Once the finer points of the creep analysis for the blade model were defined, the main goal now would be to analyze the number of cycles needed to get an overall perception of the vertical displacement of the HPT blade during service. Starting with 10 successive cycles for the PDL-FNC flight cycle, it was later realized that, by running 50 successive cycles, the first 10 were only descriptive of a transient phase of the overall trend of the parts stretching, as can be seen, for example for Node 204 in **Figure 4.12**.

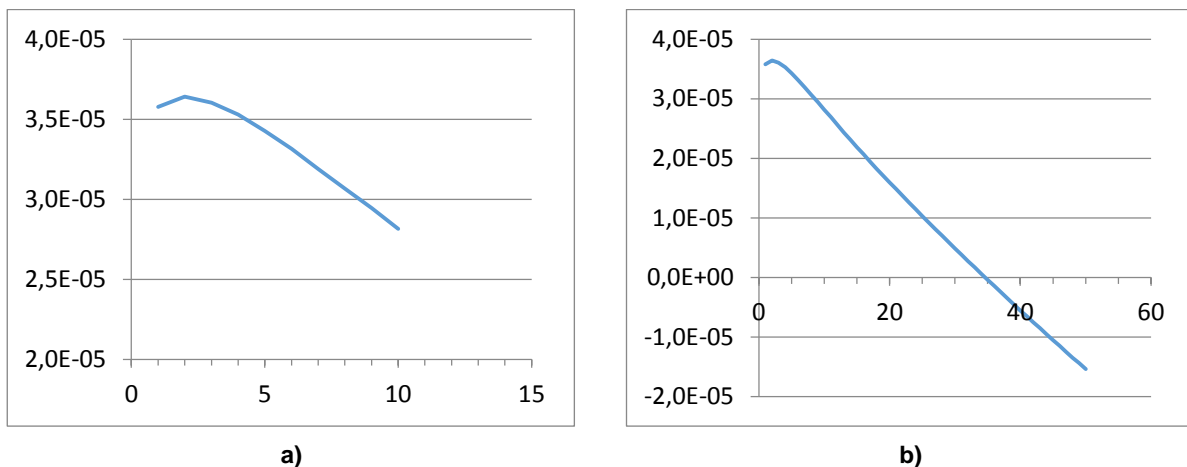


Figure 4.12 – Vertical displacement (U2) variation, in meters, of Node 204 for a) 10 cycles; b) 50 cycles.

The distribution of vertical stress, displacement, strain, and Von Mises stress, after running 50 successive cycles, can be seen in **Figure 4.13** through **Figure 4.16**, and the remaining distributions for all the other components of stress and strain, as well as the remaining two directions of displacement, all can be seen in **Appendix D**.

As can be seen in **Figure 4.13**, the highest concentration of vertical stress is, as expected, located in the bottom of the part, where it is connected to the HPT disk. In terms of displacement, **Figure 4.14** shows its highest concentration along the thinnest areas of the blade's base, especially considering that the hot gas pressure that would counteract this displacement is not present in this simulation. In **Figure 4.14**, the displacement of the trailing edge shown is in accordance with what's expected, although the retraction of the leading edge is not the behavior expected. This can mainly be explained due to the hollow nature of the real blade, whereas the model here used is a filled blade, and thus the comparison between real and simulated behavior can't easily be made. Looking at the vertical strain distribution in **Figure 4.15**, it's easy to see the areas where the transition between positive and negative values of strain helps explain the behavior mentioned before.

Finally, in **Figure 4.16**, we have the Von Mises stress, where the largest stresses are, as expected, on the bottom of the HPT blade.

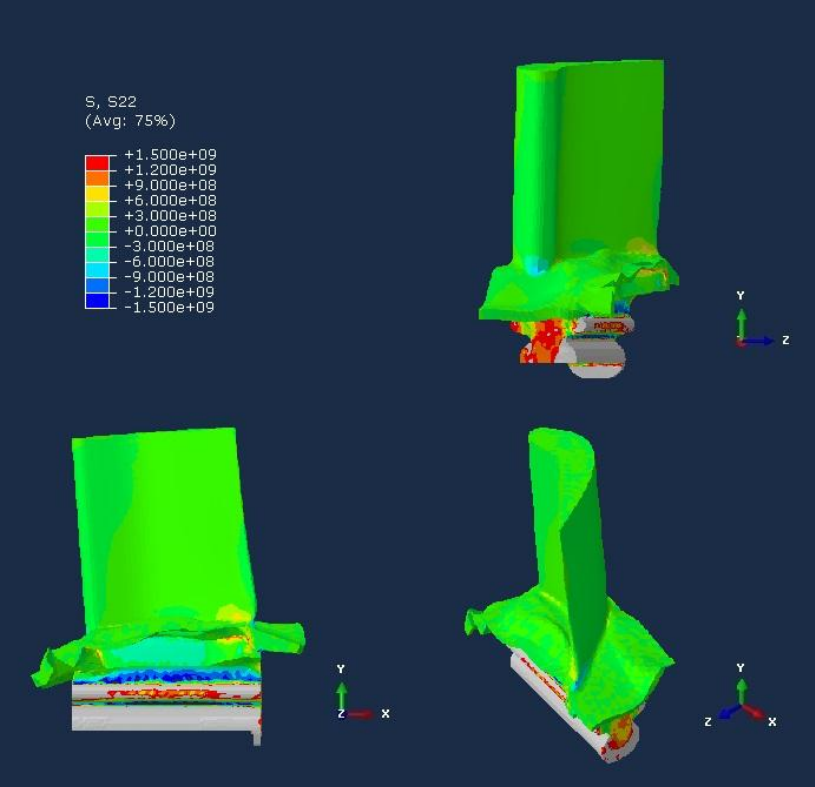


Figure 4.13 – Stress (S22) distribution after 50 PDL-FNC flight cycles.

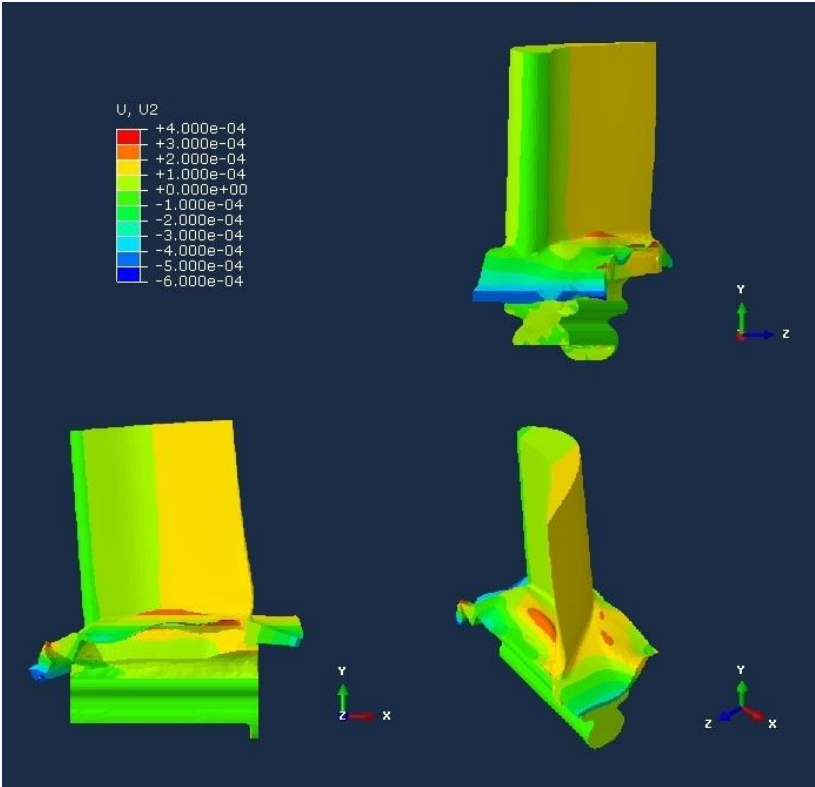


Figure 4.14 – Displacement (U2) distribution after 50 PDL-FNC flight cycles.

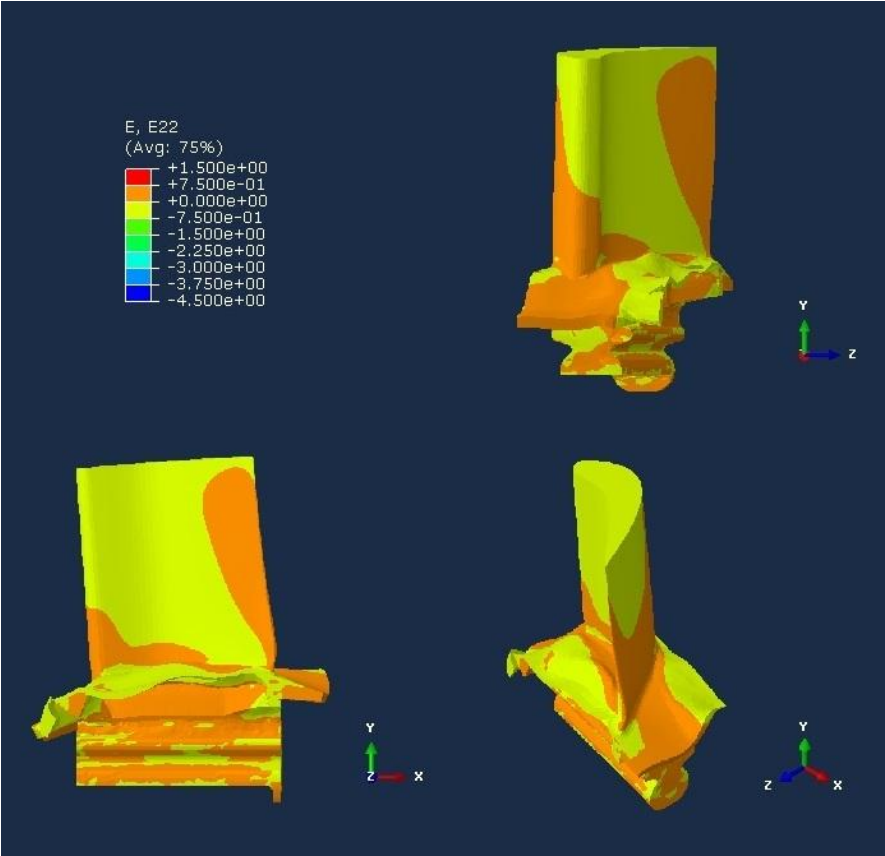


Figure 4.15 – Strain (E22) distribution after 50 PDL-FNC flight cycles.

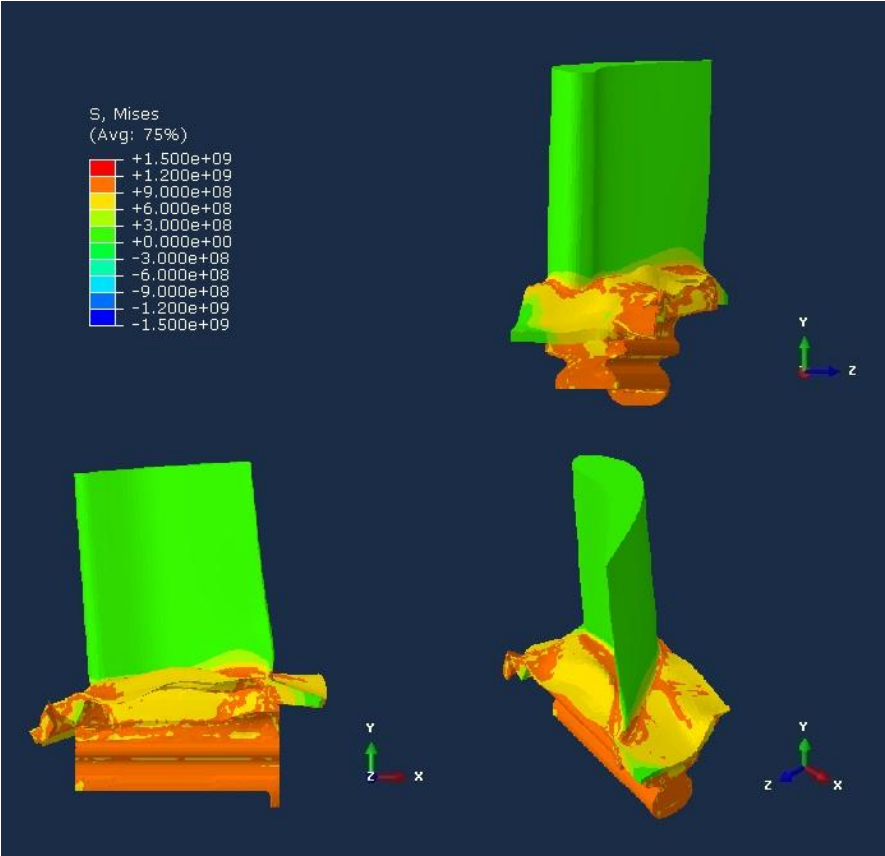


Figure 4.16 – Von Mises Stress (S_{VM}) distribution after 50 PDL-FNC flight cycles.

The same kind of simulation performed for the PDL-FNC flight cycle was also performed for both the PDL-HOR and SJZ-TER flight cycles, and the results after 50 successive cycles for each of the flight routes can be compared in **Figure 4.17**.

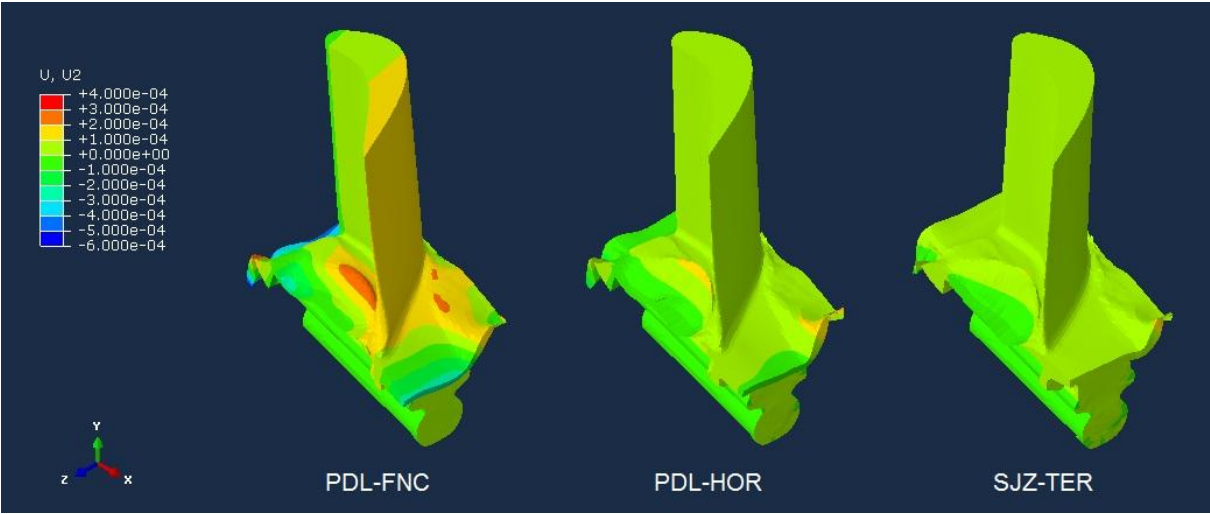


Figure 4.17 – Comparison between three different flight routes after 50 cycles.

For 50 successive flight cycles, the PDL-FNC route presents larger amounts of displacement, followed by the PDL-HOR route and finally the SJZ-TER route. This is, of course, expected, considering that the flight cycle period for each one of these cycles is 8050, 4055 and 2050 seconds, respectively. Even though the temperature and rotational speed plots may vary for the three different routes, creep is, above all, a function of time, and its effects are expected to be more noticeable for the longer overall time spent at high temperatures, during the fifty cycles.

However, given that the main goal of the study overall was to see the difference in creep behavior for these three flight cycles for a part lifetime of 3000 hours, different results may be expected when considering that, for the same time period, each of the flight cycles for the three different routes entails a different number of cycles, i.e. 1342, 2664 and 5269 cycles, for the PDL-FNC, PDL-HOR and SJZ-TER flight routes, respectively.

In order to have a base approximation of the expected blade displacement after the 3000 hours period for each to the routes, the vertical displacement results for the selected nodes in **Figure 4.1 a)** were obtained from the fifty cycle analysis. Knowing that, overall, the first ten cycles represented a transient period in the elongation trend, for the three different flight routes, using only the later forty cycle results, the linear equations for each of the seven node results were calculated, and the results for the three different flight routes and respective number of cycles were approximated for each node, as can be seen in **Table 4.2**.

In **Table 4.2** the larger values of displacement occur on the PDL-FNC flight route, followed, once more, by the PDL-HOR flight route and afterwards by the SJZ-TER flight route, with the exception of node 204, where the contraction is greater for the PDL-HOR flight route, and basically the same for both PDL-FNC and SJZ-TER flight routes; node 1235, where the SJZ-TER flight route

displays contraction as opposed to the stretching verified in other two flight routes; and finally node 574, where the contraction values are quite close for all three of the flight routes.

Table 4.2 – Nodal results for trend study of 3000 flight hours

| Flight Routes | Number of Cycles | Node | | | | | | |
|----------------|------------------|------------------|----------|----------|---------|---------|---------|----------|
| | | 18982 | 204 | 1235 | 1452 | 56 | 2415 | 574 |
| | | Displacement (m) | | | | | | |
| PDL-FNC | 1342 | 4.73E-3 | -1.41E-3 | 1.99E-3 | 2.25E-3 | 9.14E-4 | 2.12E-3 | -3.04E-3 |
| PDL-HOR | 2664 | 3.20E-3 | -1.89E-3 | 4.88E-4 | 8.94E-4 | 1.18E-3 | 9.09E-4 | -2.78E-3 |
| SJZ-TER | 5269 | 2.51E-3 | -1.48E-3 | -1.15E-4 | 4.27E-4 | 1.44E-3 | 4.65E-4 | -1.96E-3 |

This is, overall, somewhat expected given that, for the creep mechanism, all things being the same, time is the main factor, and, considering that the operating temperatures and rotation speeds are about the same for the three flight routes, even though the PDL-FNC flight cycle is experienced less times, it remains at operating conditions for a longer period of the 3000 hours, when compared to the two other cycles, and thus it experiences the greater values in terms of overall displacement. This effect, however, seems to be less pronounced in areas where contraction, instead of elongation, occurs. It is also important to note that the behavior in the three nodes on the top of the blade, nodes 18982, 204 and 1235, are very different, which, as stated earlier, comes as little to no surprise, given the behavior of the uncooled blade model and the vertical stresses evolving from compression stresses, in the leading edge, to traction stresses in the trailing edge, and that variation being a product of the different type of loading, both mechanical and thermal, in each of the three different flight routes.

5. Conclusion

The main goal of this study was the development of a numerical model that would allow for the analysis of the thermal and mechanical behavior of a HPT blade, with emphasis on creep. Numerous challenges were found, but these ended up providing not only a better understanding of the problem at hand, but also added more to the study itself. Thus, the results obtained were within what was expected of the creep behavior of the HPT blades.

The real operational data, from the FDR provided, proved to be very useful in making the thermal and mechanical cycle plotting and analysis as accurate as possible. The biggest issue with the data treatment was the isolation of each cycle within the original FDR files, a time-consuming task that, nevertheless, was made progressively faster with an increasingly better handling of the data treatment software that was used.

Due to the aircraft's recorder being shut-off right after landing, the cooling periods, needed to be taken into account in the plotting, had to be extrapolated. In the same sense, assumptions had to be made regarding the TIT. The use of references made it possible for such assumptions to be made with a comfortable degree of confidence, in the context of this work.

The lack of a 3D model of the HPT blade also necessitated an alternative solution. Thus, the blade scrap provided proved invaluable, both in the definition of the dimensions necessary for the cycle simulation and the creation of a suitable 3D model of the blade's surface. Although some difficulties arose during the scanning process, due to the small size of the scrap part, a suitable mesh was obtained and these issues didn't compromise the overall accuracy of the final model, making this a useful technique for reverse engineering of some characteristics of this type of part; provided the equipment is available.

In the same manner, the blade's material was selected through analysis of the scrap's composition and density. The density was shown not to be enough as a choosing factor, and the composition analysis was revealed to be better suited as a selection criterion. Although most of the properties were extracted from the references, not many of which were available, some of these properties also had to be assumed, with the knowledge of the expected behavior of a similar material. Once more, these assumptions were made with an acceptable degree of confidence, in the context of this work.

The choice of conducting trial simulations on the rectangular block model made it possible not only to compare isothermal models with thermal distribution models, but also between elastoplastic models and creep based models. It became clear that disregarding the temperature distribution along the part, i.e. making it isothermal, showed different results, and thus the thermal analysis was required to be performed before the mechanical analysis.

This proved to be very important in the definition of the simulations to later be performed on the more complex blade model. Nevertheless, comparison between elastoplastic and creep models was also performed on this model, which not only confirmed that the proper way to run a simulation of creep required a specific type of analysis (where creep data was needed), but also helped notice the software issues of overstress in the blade's bottom.

The overall behavior in terms of displacement in the blade models, after accumulation of the different flight cycles analyzed, was not the expected in some parts of the blade given some cases of contraction, slight as it may be, especially in the leading edge. As mentioned earlier, this seems to be an issue of the model and not a reflection of the blade's actual behavior. However, the trailing edge showed the behavior and dimension one would expect after each cycle, and the model was able to adequately integrate the temperature distribution variations with the mechanical loading.

Thus, this model provides a very rough yet useful way to look at the creep behavior of this type of part for real life flight conditions.

5.1. Future work

Although the 3000 hours lifetime study showed some interesting results in terms of creep, it must be taken into account, nonetheless, that this final trend study is a very rough approximation and that the creep analysis done for this work represents a good first step.

Several changes could be made, with more time and resources, to improve its accuracy as well as its ability to better resemble the behavior of a real HPT blade under flight conditions.

The knowledge of the real material properties, especially the creep equations for different temperatures, knowledge of pressure on the HPT, and a complete 3D model with cooling; all these additions to the model could yield more accurate results.

This extra data, along with better computational resources, could allow for the definition of thermal and mechanical loading cycles for all the flight routes performed by the aircraft.

Knowing the scheduled flights for these aircrafts, it would be possible to make predictions for the creep behavior of the HPT blades for different combinations of flight cycles, and thus a much more accurate prediction of the blade's creep behavior could be made prior to the usage of parts in service.

6. References

- [1] D. C. Nadeau, "The Development of a Thermal Model to Predict Corrosion Propensity on Internal Features of Turbine Airfoils," Rensselaer Polytechnic Institute, 2013.
- [2] R. A. L. D. Cláudio, "Previsão de Vida Fadiga/Fluência em Discos de Turbina de Turborreactores," 2001.
- [3] M. P. Boyce, "An Overview of Gas Turbines," in *Gas Turbine Engineering Handbook*, 2nd ed., Woburn, MA: Butterworth-Heinemann, 2002, pp. 9–15.
- [4] M. P. Boyce, "Axial-Flow Turbines," in *Gas Turbine Engineering Handbook*, 2nd ed., Woburn, MA: Butterworth-Heinemann, 2002, pp. 351–363.
- [5] T. Giampaolo, "Applications," in *Gas Turbine Handbook: Principles and Practice*, 4th ed., Lilburn, GA: The Fairmont Press, 2009, pp. 11–15.
- [6] M. P. Boyce, "Theoretical and Actual Cycle Analysis," in *Gas Turbine Engineering Handbook*, 2nd ed., Woburn, MA: Butterworth-Heinemann, 2002, pp. 58–62.
- [7] M. P. Boyce, "Theoretical and Actual Cycle Analysis," in *Gas Turbine Engineering Handbook*, 2nd ed., Woburn, MA: Butterworth-Heinemann, 2002, p. 59.
- [8] M. P. Boyce, "Theoretical and Actual Cycle Analysis," in *Gas Turbine Engineering Handbook*, 2nd ed., Woburn, MA: Butterworth-Heinemann, 2002, pp. 70–72.
- [9] M. P. Boyce, "Theoretical and Actual Cycle Analysis," in *Gas Turbine Engineering Handbook*, 2nd ed., Woburn, MA: Butterworth-Heinemann, 2002, p. 71.
- [10] T. Benson, "Types of Gas Turbines," NASA, 2014. [Online]. Available: <http://www.grc.nasa.gov/WWW/K-12/airplane/trbtyp.html>. [Accessed: 06-Aug-2014].
- [11] T. Benson, "Turbojet Engine," NASA, 2014. [Online]. Available: <http://www.grc.nasa.gov/WWW/K-12/airplane/aturbj.html>. [Accessed: 06-Aug-2014].
- [12] T. Benson, "Compressors," NASA, 2014. [Online]. Available: <http://www.grc.nasa.gov/WWW/K-12/airplane/compress.html>. [Accessed: 06-Aug-2014].
- [13] Emoscopes, "File:Turbojet operation- centrifugal flow.png," *Wikipedia*, 2005. [Online]. Available: http://en.wikipedia.org/wiki/Turbojet#/media/File:Turbojet_operation-_centrifugal_flow.png. [Accessed: 06-Aug-2014].
- [14] Emoscopes, "File:Turbojet operation- axial flow.png," *Wikipedia*, 2005. [Online]. Available: http://en.wikipedia.org/wiki/Turbojet#/media/File:Turbojet_operation-_axial_flow.png. [Accessed: 06-Aug-2014].
- [15] T. Benson, "Turbofan Engine," NASA, 2014. [Online]. Available: <http://www.grc.nasa.gov/WWW/K-12/airplane/aturbf.html>. [Accessed: 06-Aug-2014].
- [16] T. Benson, "Turbofan Thrust," NASA, 2014. [Online]. Available: <http://www.grc.nasa.gov/WWW/K-12/airplane/turbfan.html>. [Accessed: 06-Aug-2014].
- [17] 456FIS, "The Jet Engine," *The 456th Fighter Interceptor Squadron*, 2014. [Online]. Available: http://www.456fis.org/JET_ENGINS.htm. [Accessed: 06-Aug-2014].

- [18] K. Aainsqatsi, "File:Turbofan operation lbp.svg," *Wikipedia*, 2008. [Online]. Available: http://en.wikipedia.org/wiki/Turbofan#/media/File:Turbofan_operation_lbp.svg. [Accessed: 06-Aug-2014].
- [19] K. Aainsqatsi, "File:Turbofan operation.svg," *Wikipedia*, 2008. [Online]. Available: http://en.wikipedia.org/wiki/Turbofan#/media/File:Turbofan_operation.svg. [Accessed: 06-Aug-2014].
- [20] C. Riegler and C. Bichlmaier, "The Geared Turboprop Technology—Opportunities, Challenges and Readiness Status," in *1st CEAS European Air and Space Conference*, 2007.
- [21] T. Benson, "Turboprop Engine," *NASA*, 2014. [Online]. Available: <http://www.grc.nasa.gov/WWW/K-12/airplane/aturbp.html>. [Accessed: 06-Aug-2014].
- [22] Emoscopes, "File: Turboprop operation-en.svg," *Wikipedia*, 2009. [Online]. Available: http://en.wikipedia.org/wiki/Turboprop#/media/File:Turboprop_operation-en.svg. [Accessed: 06-Aug-2014].
- [23] Pratt & Whitney Canada, "PW150A," *Pratt & Whitney Canada*. [Online]. Available: <http://www.pwc.ca/en/engines/pw150a>. [Accessed: 07-Aug-2014].
- [24] Michael, "CBT and the Q400," *Mike's Flying*, 2012. [Online]. Available: <http://mikesflying.blogspot.pt/2012/08/cbt-and-q400.html>. [Accessed: 10-Aug-2014].
- [25] Bombardier, "Engine, General," *AIRCRAFT MAINTENANCE MANUAL – SYSTEM DESCRIPTION SECTION*. Bombardier, Montreal, Canada, pp. 2–18, 2008.
- [26] Bombardier, "Reduction Gear Box," *AIRCRAFT MAINTENANCE MANUAL – SYSTEM DESCRIPTION SECTION*. Bombardier, Montreal, Canada, pp. 2–8, 2008.
- [27] Bombardier, "Air Intake," *AIRCRAFT MAINTENANCE MANUAL – SYSTEM DESCRIPTION SECTION*. Bombardier, Montreal, Canada, pp. 2–4, 2008.
- [28] Bombardier, "Compressor Section," *AIRCRAFT MAINTENANCE MANUAL – SYSTEM DESCRIPTION SECTION*. Bombardier, Montreal, Canada, pp. 2–6, 2008.
- [29] Bombardier, "Low Pressure Compressor," *AIRCRAFT MAINTENANCE MANUAL – SYSTEM DESCRIPTION SECTION*. Bombardier, Montreal, Canada, pp. 2–6, 2009.
- [30] ExpertsMind IT Educational, "The axial flow compressor - aircraft engine, Other Engineering," *ExpertsMind.com*, 2012. [Online]. Available: <http://www.expertsmind.com/questions/the-axial-flow-compressor-aircraft-engine-30111555.aspx>. [Accessed: 07-Aug-2014].
- [31] Bombardier, "High Pressure Compressor," *AIRCRAFT MAINTENANCE MANUAL – SYSTEM DESCRIPTION SECTION*. Bombardier, Montreal, Canada, pp. 2–4, 2008.
- [32] B. Kala, "The centrifugal flow compressor," *Model aircraft*, 2011. [Online]. Available: <http://aeromodelbasic.blogspot.pt/2011/12/centrifugal-flow-compressor.html>. [Accessed: 07-Aug-2014].
- [33] Bombardier, "Combustion Section," *AIRCRAFT MAINTENANCE MANUAL – SYSTEM DESCRIPTION SECTION*. Bombardier, Montreal, Canada, pp. 2–4, 2008.
- [34] Bombardier, "High Pressure Combustor," *AIRCRAFT MAINTENANCE MANUAL – SYSTEM DESCRIPTION SECTION*. Bombardier, Montreal, Canada, pp. 2–4, 2011.

- [35] Bombardier, "Turbines," *AIRCRAFT MAINTENANCE MANUAL – SYSTEM DESCRIPTION SECTION*. Bombardier, Montreal, Canada, pp. 2–4, 2008.
- [36] Bombardier, "Power Turbines," *AIRCRAFT MAINTENANCE MANUAL – SYSTEM DESCRIPTION SECTION*. Bombardier, Montreal, Canada, pp. 2–8, 2008.
- [37] Bombardier, "Power Turbines," *AIRCRAFT MAINTENANCE MANUAL – SYSTEM DESCRIPTION SECTION*. Bombardier, Montreal, Canada, p. 4, 2008.
- [38] H. Prasad, "Comparison between Impulse and Reaction Steam Turbines," *Mechanical Engineering*. [Online]. Available: <http://mechanical-engineering-info.blogspot.pt/>. [Accessed: 08-Aug-2014].
- [39] Bombardier, "Power Turbines," *AIRCRAFT MAINTENANCE MANUAL – SYSTEM DESCRIPTION SECTION*. Bombardier, Montreal, Canada, p. 5, 2008.
- [40] Bombardier, "Power Turbines," *AIRCRAFT MAINTENANCE MANUAL – SYSTEM DESCRIPTION SECTION*. Bombardier, Montreal, Canada, p. 6, 2008.
- [41] Bombardier, "Power Turbines," *AIRCRAFT MAINTENANCE MANUAL – SYSTEM DESCRIPTION SECTION*. Bombardier, Montreal, Canada, p. 7, 2008.
- [42] T. Giampaolo, "Hardware," in *Gas Turbine Handbook: Principles and Practice*, 4th ed., Lilburn, GA: The Fairmont Press, 2009, pp. 27–35.
- [43] S. Darwin and D. Chiron, "ULTMAT Ultra High Temperature Materials for Turbines," *European Commission Research & Innovation Transport Projects*, 2004. [Online]. Available: http://ec.europa.eu/research/transport/projects/items/ultmat_en.htm. [Accessed: 10-Aug-2014].
- [44] T. Giampaolo, "Gas Turbine Systems Theory," in *Gas Turbine Handbook: Principles and Practice*, 4th ed., Lilburn, GA: The Fairmont Press, 2009, p. 52.
- [45] N. Goto, Y. Kusuki, S. Endo, N. Toyooka, Y. Shuto, and A. Matsuo, "AIRCRAFT SERIOUS INCIDENT INVESTIGATION REPORT," 2010.
- [46] C. Eady, "Chapter 4 - Modes of Gas Turbine Component Life Consumption," in *Recommended Practices For Monitoring Gas Turbine Engine Life Consumption*, 1 ed., M. Sapsard, Ed. France: RTO/NATO, 2000, pp. 4–1.
- [47] T. Carter, "Common failures in gas turbine blades," *Eng. Fail. Anal.*, vol. 12, no. 2, pp. 237–247, Apr. 2005.
- [48] A. Rybnikov, L. Getsov, and S. Leontiev, "Failure Analysis of Gas Turbine Blades," *Microsc. Microanal.*, vol. 11, no. S02, pp. 222–223, Aug. 2005.
- [49] J. Blachnio and W. I. Pawlak, "Damageability of Gas Turbine Blades – Evaluation of Exhaust Gas Temperature in Front of the Turbine Using a Non-Linear Observer," in *Advances in Gas Turbine Technology*, E. Benini, Ed. Rijeka, Croatia: InTech, 2011, pp. 435–464.
- [50] Y. Assoul, S. Benbelaid, V. Sijacki-Zeravcic, G. Bakic, and M. Dukic, "Life Estimation of First Stage High Pressure Gas Turbine Blades," *Sci. Tech. Rev.*, vol. 58, no. 2, pp. 8–13, 2008.
- [51] R. Bowman, "Superalloys: A Primer and History," *The Minerals, Metals & Materials Society's 9th International Symposium on Superalloys*, 2000. [Online]. Available: <http://www.tms.org/meetings/specialty/superalloys2000/superalloyshistory.html>. [Accessed: 15-Aug-2014].

- [52] T. M. Pollock and S. Tin, "Nickel-Based Superalloys for Advanced Turbine Engines: Chemistry, Microstructure and Properties," *Journal of Propulsion and Power*, vol. 22, no. 2. pp. 361–374, 2006.
- [53] H. Harada, "High Temperature Materials for Gas Turbines : The Present and Future," in *Proceedings of the International Gas Turbine Congress*, 2003, pp. 1–9.
- [54] P. Caron and T. Khan, "Evolution of Ni-based superalloys for single crystal gas turbine blade applications," *Aerosp. Sci. Technol.*, vol. 3, no. 8, pp. 513–523, 1999.
- [55] Dongying Dyne Casting Co., "Lost Wax Process," *Dyne-casting.com*, 2010. [Online]. Available: <http://www.dyne-casting.com/lost-wax-process.htm>. [Accessed: 17-Aug-2014].
- [56] I. Pires, "Fundição de Metais - Parte 1," *Polymer Processing and Casting - Support Material*, 2013. [Online]. Available: https://fenix.tecnico.ulisboa.pt/downloadFile/3779580063371/fundicao_parte1.pdf. [Accessed: 16-Aug-2014].
- [57] M. Segersäll, "Nickel-Based Single-Crystal Superalloys : the crystal orientation influence on high temperature properties," Linköping University, 2013.
- [58] C. A. Estrada, "New Technology Used in Gas Turbine Blade Materials .," *Sci. Tech. Año XIII*, no. 36, pp. 297–301, 2007.
- [59] P. W. Schilke, "Advanced Gas Turbine Materials and Coatings," *GE Energy*. 2004.
- [60] Wadley Research Group, "High Temperature Coatings," *Virginia.edu*, 2013. [Online]. Available: <http://www.virginia.edu/ms/research/wadley/high-temp.html>. [Accessed: 20-Aug-2014].
- [61] J. Han, "Recent Studies in Turbine Blade Cooling," *Int. J. Rotating Mach.*, vol. 10, no. 6, pp. 443–457, 2004.
- [62] D. G. Bogard and K. A. Thole, "Gas Turbine Film Cooling," *J. Propuls. Power*, vol. 21, no. 6, p. 24, 2005.
- [63] X. Wu, "Life Prediction of Gas Turbine Materials," in *Gas Turbines*, G. Injeti, Ed. 2010.
- [64] S. Tin, "Modeling of Creep," in *ASM Handbook*, vol. 22A, D. U. Furrer and S. L. Semiatin, Eds. ASM International, 2009, pp. 400–407.
- [65] S. Eshati, "AN EVALUATION OF OPERATION AND CREEP LIFE OF STATIONARY GAS TURBINE ENGINE," CRANFIELD UNIVERSITY SCHOOL OF ENGINEERING, 2012.
- [66] ExpertsMind IT Educational, "Effect of Temperature and Stress on Creep," *ExpertsMind.com*, 2012. [Online]. Available: <http://www.expertsmind.com/topic/material-problems-at-elevated-temperatures/effect-of-temperature-and-stress-919147.aspx>. [Accessed: 10-Sep-2014].
- [67] M. K. Samal and S. Ghosh, "Evaluation of creep deformation and mechanical properties of nickel-based superalloys through fe analysis based on crystal plasticity models," in *Procedia Engineering*, 2013, vol. 55, pp. 342–347.
- [68] A. Epishin, T. Link, H. Klingelhöffer, B. Fedelich, and P. Portella, "Creep damage of single-crystal nickel base superalloys: Mechanisms and effect on low cycle fatigue," *Mater. High Temp.*, vol. 27, no. 1, pp. 53–59, 2010.
- [69] S. Saevdal, "De Havilland Canada Aircraft," *719skvadron.no*, 2013. [Online]. Available: <http://www.719skvadron.no/dhc6/dhc-history.htm>. [Accessed: 19-Oct-2014].

- [70] Fubra Limited, "World Airport Codes," *World-airport-codes.com*. [Online]. Available: <https://www.world-airport-codes.com/>. [Accessed: 15-Jul-2014].
- [71] Z Corporation, "ZScanner Product Line," *ZScanner*. Z Corporation, Burlington, MA, pp. 241–264, 2009.
- [72] R. C. Reed, T. Tao, and N. Warnken, "Alloys-By-Design: Application to nickel-based single crystal superalloys," *Acta Mater.*, vol. 57, no. 19, pp. 5898–5913, 2009.
- [73] D. Dye, K. T. Conlon, P. D. Lee, R. B. Rogge, and R. C. Reed, "Welding of Single Crystal Superalloy CMSX-4: Experiments and Modeling," in *Superalloys 2004 (Tenth International Symposium)*, 2004, pp. 485–491.
- [74] N. I. F. M. Science(NIMS), "Third Generation Nickel Base Single Crystal Superalloy Tms-75 (Tmd-103)," *Mater. Sci.*, vol. 5, no. 1, pp. 5–10, 2006.

Appendix

Appendix A – Example excerpt from original Flight Data Record file provided by the airline company

| COUNTER | ALTcapt | CASrh | ENG1itt | ENG1nh | ENG1nl | ENG1torque | ENG2itt | ENG2nh | ENG2nl | ENG2torque | NAVlat | NAVlong | SATrh | TIME |
|---------|---------|-------|---------|--------|--------|------------|---------|--------|--------|------------|------------|-------------|-------|------|
| 498.000 | 100 | 0 | 435 | 71 | 54 | 4 | 432 | 72 | 54 | 4 | 38.770.723 | -27.101.878 | 18.2 | 558 |
| 499.000 | 96 | 0 | 434 | 71 | 54 | 4 | 432 | 72 | 54 | 4 | 38.770.723 | -27.101.878 | 18.0 | 558 |
| 500.000 | 96 | 31 | 434 | 71 | 54 | 4 | 431 | 72 | 54 | 4 | 38.770.723 | -27.101.878 | 18.0 | 562 |
| 501.000 | 106 | 31 | 433 | 71 | 54 | 4 | 432 | 72 | 54 | 5 | 38.770.723 | -27.101.878 | 18.0 | 562 |
| 502.000 | 106 | 0 | 433 | 72 | 54 | 7 | 433 | 72 | 55 | 9 | 38.770.723 | -27.101.878 | 18.0 | 562 |
| 503.000 | 102 | 34 | 439 | 75 | 59 | 13 | 442 | 76 | 61 | 16 | 38.770.723 | -27.101.878 | 18.0 | 562 |
| 504.000 | 106 | 30 | 453 | 80 | 69 | 26 | 459 | 82 | 72 | 33 | 38.770.723 | -27.101.878 | 18.0 | 566 |
| 505.000 | 104 | 33 | 473 | 86 | 79 | 46 | 478 | 87 | 81 | 50 | 38.770.723 | -27.101.878 | 18.0 | 566 |
| 506.000 | 108 | 41 | 488 | 89 | 84 | 59 | 491 | 89 | 85 | 63 | 38.770.723 | -27.100.504 | 18.0 | 566 |
| 507.000 | 110 | 50 | 508 | 90 | 86 | 69 | 508 | 91 | 87 | 72 | 38.770.723 | -27.100.504 | 18.0 | 566 |
| 508.000 | 114 | 56 | 545 | 91 | 88 | 78 | 543 | 92 | 88 | 79 | 38.770.723 | -27.100.504 | 18.0 | 570 |
| 509.000 | 122 | 61 | 573 | 92 | 89 | 81 | 565 | 92 | 89 | 81 | 38.770.723 | -27.100.504 | 17.7 | 570 |
| 510.000 | 118 | 67 | 591 | 92 | 89 | 81 | 581 | 92 | 89 | 81 | 38.769.350 | -27.100.504 | 17.7 | 570 |
| 511.000 | 190 | 76 | 604 | 92 | 89 | 82 | 595 | 92 | 89 | 81 | 38.769.350 | -27.100.504 | 17.5 | 570 |
| 512.000 | 128 | 77 | 615 | 92 | 89 | 81 | 605 | 92 | 89 | 81 | 38.769.350 | -27.100.504 | 17.5 | 574 |
| 513.000 | 130 | 78 | 624 | 92 | 89 | 82 | 613 | 92 | 89 | 82 | 38.769.350 | -27.100.504 | 17.5 | 574 |
| 514.000 | 130 | 87 | 632 | 92 | 89 | 81 | 622 | 92 | 89 | 81 | 38.769.350 | -27.099.131 | 17.5 | 574 |
| 515.000 | 136 | 97 | 638 | 92 | 89 | 81 | 628 | 92 | 89 | 81 | 38.769.350 | -27.099.131 | 17.2 | 574 |

Appendix B – Mesh convergence and errors

Both for the rectangular block and blade models, two mesh refinements were conducted in order to ascertain which would yield the most accurate results. For both models, three different seed sizes were used, i.e. 1 mm, 0.75 mm and 0.6 mm for the rectangular block model, and 1.4 mm, 1.2 mm and 0.75 mm for the blade model. In both cases, the finest meshes were the most difficult to run, and no finer mesh would be acceptable, due to memory restraints on the part of the computer used. Also, the finer meshes demanded far more extended periods to run the different simulations, which, was an unacceptable constraint. This is the main reason why the recommended 1.4 mm and 1 mm seed sizes were the ones used for the blade and rectangular block models, respectively.

Because of the limitations mentioned earlier, choosing to use the seed sizes mentioned created the need to calculate the errors associated with using the least fine mesh and the one in between, using as reference the finest possible mesh used. For the rectangular block and blade model, a single cycle's results for vertical displacement (U2), vertical stress (S22) and vertical strain (E22) were extracted from the three less problematic nodes selected for the creep analysis, and the errors are shown in **Table A1** and **Table A2**. The U2 errors for the remaining nodes are shown in **Table A3** for the blade model, and **Table A4** for the rectangular block model, where the four different types of analysis are considered.

The errors vary from node to node, and a reduction of the error in certain nodes, as the seed size grows smaller, can be clearly seen. However, given the relatively small error in terms of displacement on the blade model, the results obtained using the seed size of 1.4 mm, i.e. the coarser mesh, can still be considered acceptable.

It is important to also note that, for the rectangular block model, the errors for displacement in node 1 and node 16525 for the creep analysis, are greater for the coarser meshes in relation to the finer mesh, mainly due to their nature as interception nodes, and the importance of this error can be understated, given that the importance of the displacement was focused mainly on the blade model, and the rectangular block model was mainly used to compare different types of analyses.

Table A1 – Creep analysis associated error for 0,75 mm seed size for the blade model.

| Analysis Results | Seed Size (mm) | Node | | |
|-------------------|----------------|-----------|------|-----|
| | | 1452 | 2415 | 574 |
| | | Error (%) | | |
| Stress (S22) | 1.4 | 2 | 17 | 2 |
| | 1.2 | 1 | 2 | 3 |
| Displacement (U2) | 1.4 | 11 | 10 | 2 |
| | 1.2 | 7 | 6 | 2 |
| Strain (E22) | 1.4 | 3 | 22 | 3 |
| | 1.2 | 4 | 16 | 13 |

Table A2 – Creep analysis associated error with 0,6 mm seed size for the rectangular block model.

| Analyses Results | Seed Size | Node | | |
|-------------------|-----------|-----------|-------|-------|
| | | 194 | 17304 | 15991 |
| | (mm) | Error (%) | | |
| Stress (S22) | 1 | 81 | 5 | 4 |
| | 0.75 | 42 | 4 | 4 |
| Displacement (U2) | 1 | 2 | 18 | 17 |
| | 0.75 | 0 | 9 | 8 |
| Strain (E22) | 1 | 2 | 5 | 5 |
| | 0.75 | 0 | 3 | 3 |

Table A3 – Displacement (U2) error associated with 0,75 mm seed size for the blade model.

| Analysis Results | Seed Size | Node | | | | | | |
|-------------------|-----------|-----------|-----|------|------|----|------|-----|
| | | 18982 | 204 | 1235 | 1452 | 56 | 2415 | 574 |
| | (mm) | Error (%) | | | | | | |
| Displacement (U2) | 1.4 | 53 | 3 | 0 | 11 | 29 | 10 | 2 |
| | 1.2 | 33 | 2 | 1 | 7 | 9 | 6 | 2 |

Table A4 – Displacement (U2) error associated with 0,6 mm seed size for the rectangular block model.

| Analysis | Seed Size | Node | | | | | | |
|--------------------------|-----------|-----------|-----|-------|-----|-------|-------|-------|
| | | 33018 | 194 | 29449 | 1 | 16525 | 17304 | 15991 |
| | (mm) | Error (%) | | | | | | |
| Creep | 1 | 1 | 2 | 2 | 766 | 1241 | 18 | 17 |
| | 0.75 | 0 | 0 | 0 | 173 | 192 | 9 | 8 |
| Isothermal Creep | 1 | 2 | 2 | 2 | 90 | 79 | 21 | 20 |
| | 0.75 | 0 | 0 | 0 | 23 | 15 | 11 | 10 |
| Elastoplastic | 1 | 1 | 2 | 2 | 31 | 29 | 29 | 29 |
| | 0.75 | 0 | 0 | 0 | 7 | 5 | 15 | 14 |
| Isothermal Elastoplastic | 1 | 1 | 2 | 2 | 24 | 22 | 33 | 32 |
| | 0.75 | 0 | 0 | 0 | 6 | 4 | 17 | 16 |

Appendix C – Temperature distribution on the thermal model

The temperature distribution in specific instants of the thermal model for both the rectangular block and blade models during the PDL-FNC flight cycle can be seen in **Figure A1** through **Figure A9**.

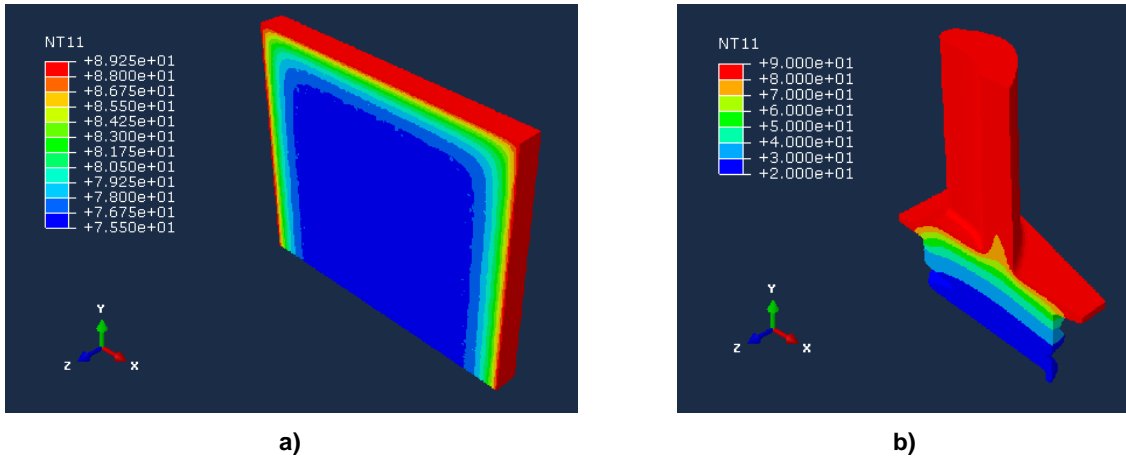


Figure A1 – Temperature distribution at 10 seconds for a) rectangular block model; b) blade model.

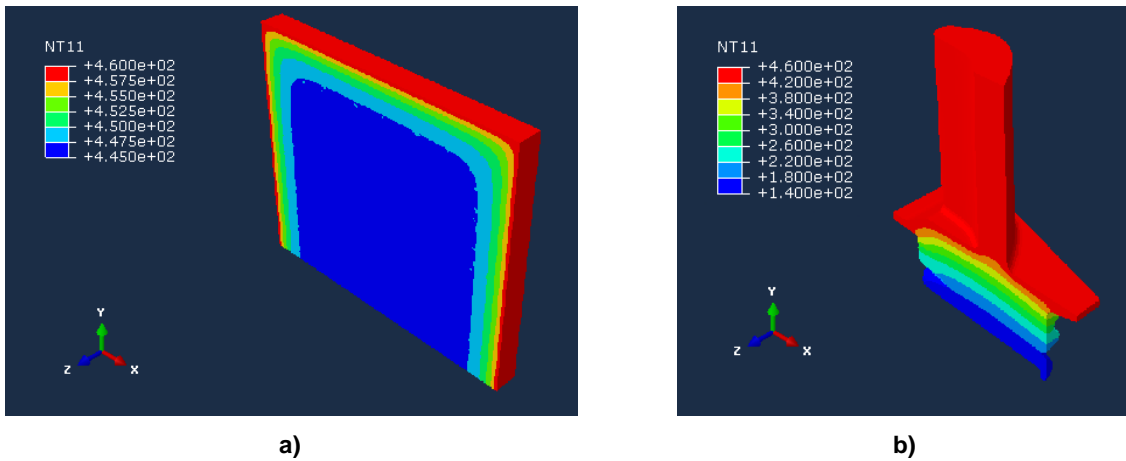


Figure A2 – Temperature distribution at 25 seconds for a) rectangular block model; b) blade model.

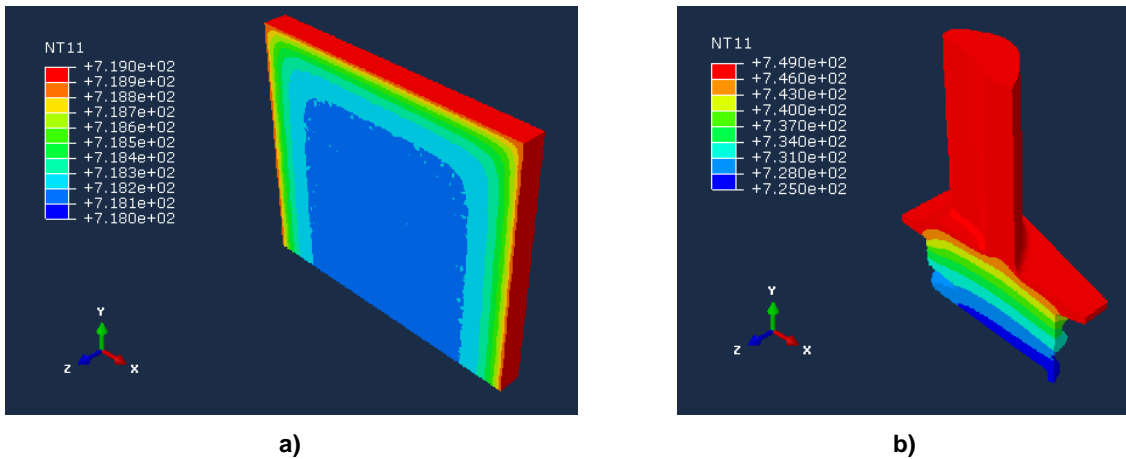
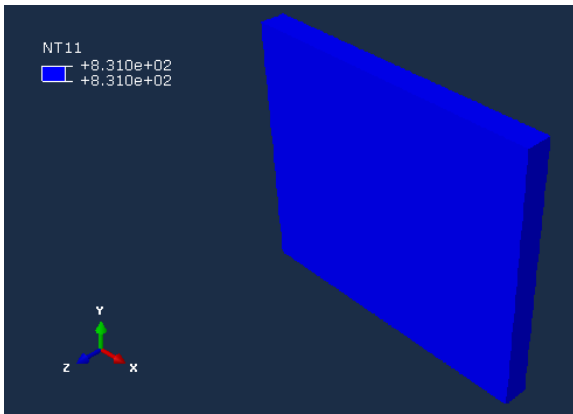
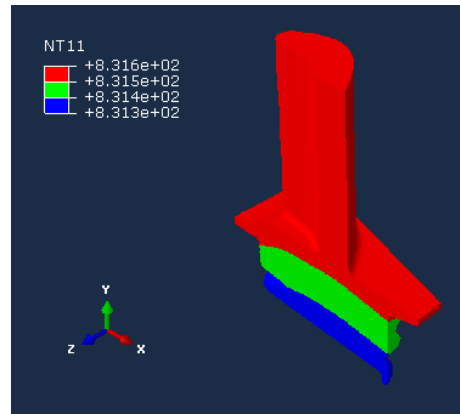


Figure A3 – Temperature distribution for a) rectangular block model at 525 s; b) blade model at 535 s.

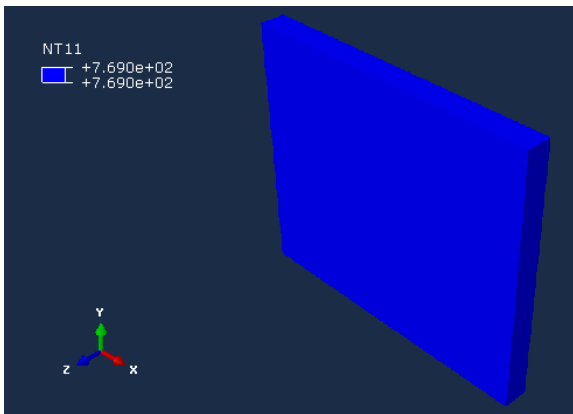


a)

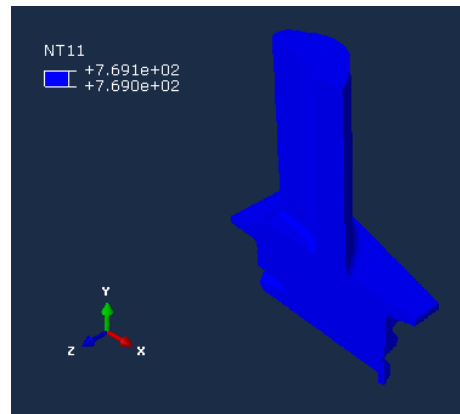


b)

Figure A4 – Temperature distribution for a) rectangular block model at 1025 s; b) blade model at 1035 s.

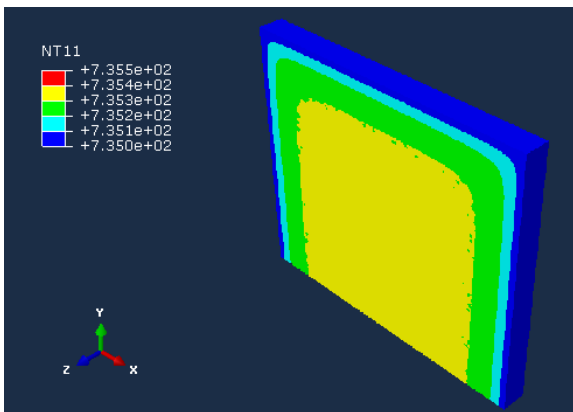


a)

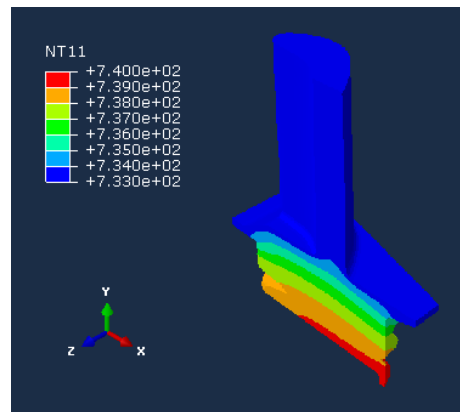


b)

Figure A5 – Temperature distribution for a) rectangular block model at 1775 s; b) blade model at 1785 s.

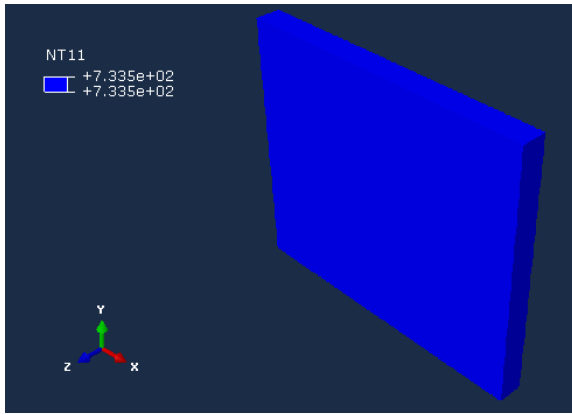


a)

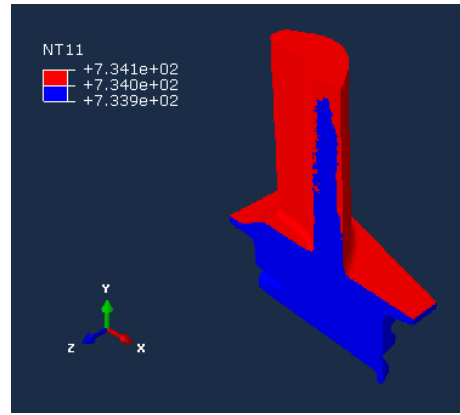


b)

Figure A6 – Temperature distribution for a) rectangular block model at 5275 s; b) blade model at 5285 s.

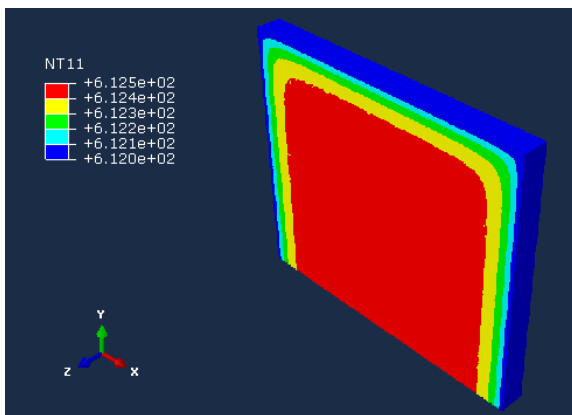


a)

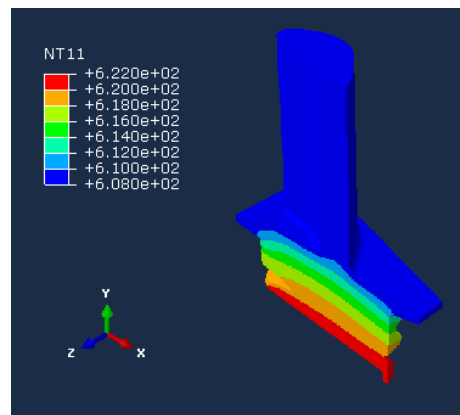


b)

Figure A7 – Temperature distribution for a) rectangular block model at 5525 s; b) blade model at 5235 s.

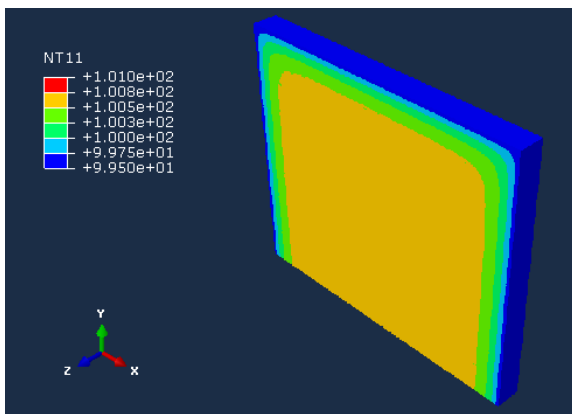


a)

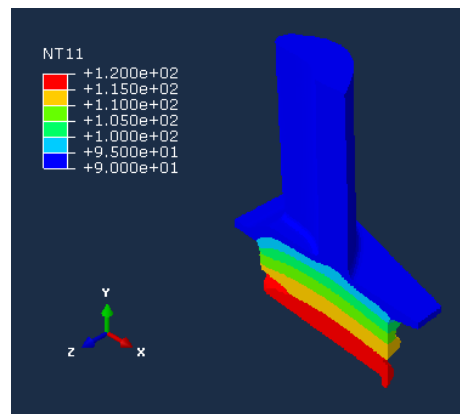


b)

Figure A8 – Temperature distribution for a) rectangular block model at 5775 s; b) blade model at 5785 s.



a)



b)

Figure A9 – Temperature distribution for a) rectangular block model at 7775 s; b) blade model at 7785 s.

It can be seen that, after the first two instants selected, the models are no longer synchronized, due to the increments of time becoming different as a result of the different geometries and complexity of the models.

Nonetheless, the distributions are similar for both models, as the first one, the rectangular block model, was used to ascertain the need for thermal analysis in the blade model. Nevertheless, the differences seen, besides being caused by the 10 second gaps of the time increments, can also be explained by the very difference in geometry and larger size of the blade model, considering that the rectangular block is intended to represent the blade's airfoil.

The end temperatures of both models have already been shown in **Figure 4.2**, but it is still important to see the temperature distribution during the cooling period for the blade model, exempt from the rectangular block model for the reasons explained in section **4.1**.

In **Figure A10 a), b) and c)**, we can see the aforementioned cooling process right up to the final instant of the cycle.

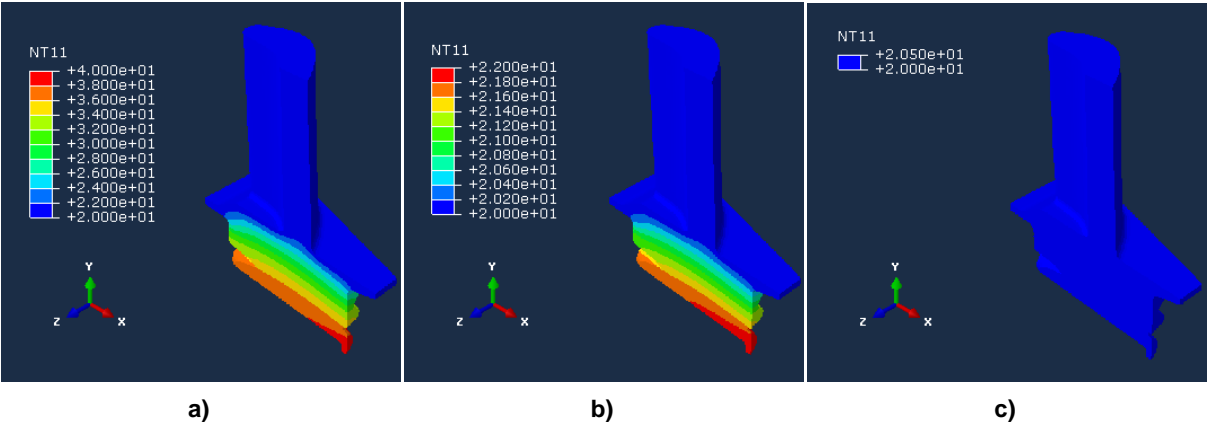


Figure A10 – Temperature distribution in the thermal model during the cooling period for instant a) 7885 s; b) 7985 s; c) 8050 s.

Appendix D – Distribution of Stress, Strain and Displacement for the remaining directions

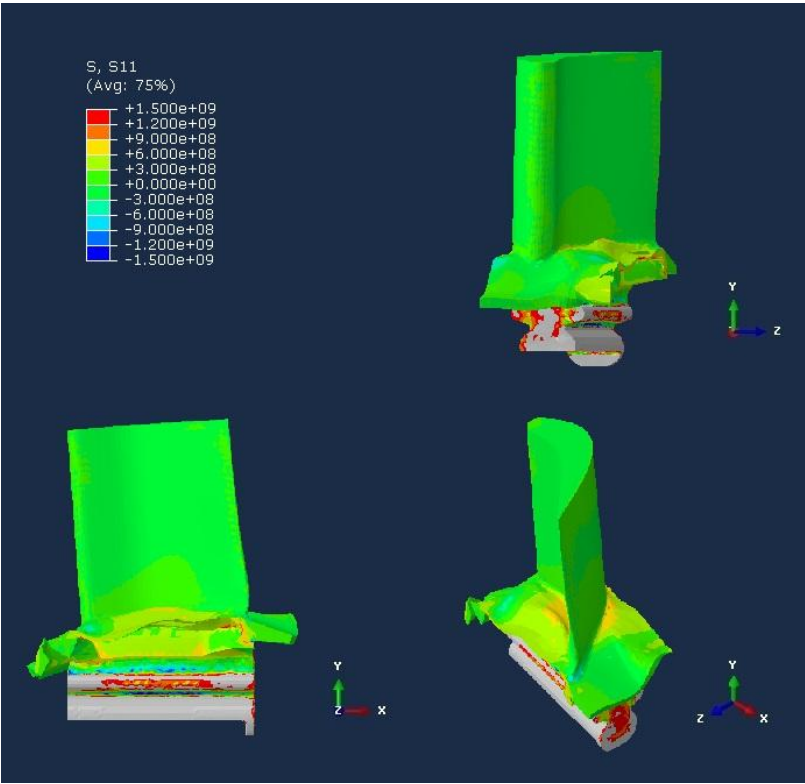


Figure A11 - Stress (S11) distribution after 50 PDL-FNC flight cycles.

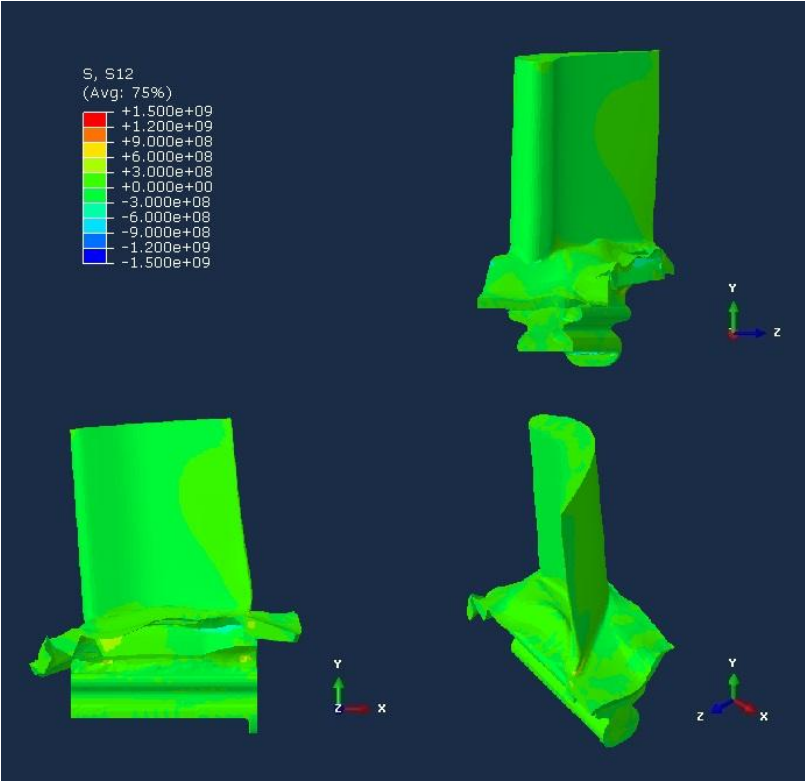


Figure A12 - Stress (S12) distribution after 50 PDL-FNC flight cycles.

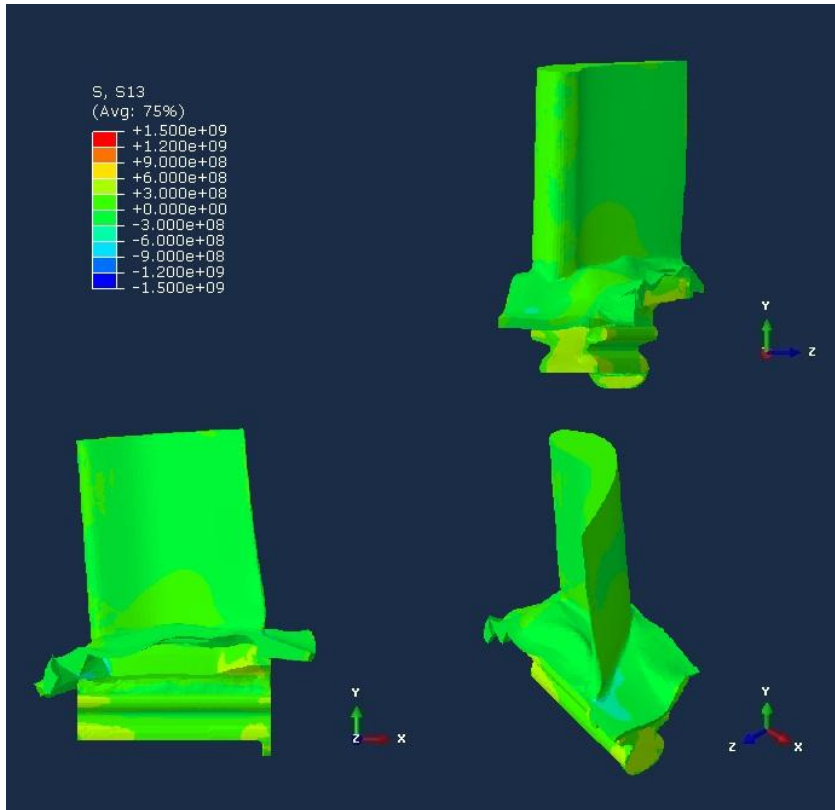


Figure A13 - Stress (S13) distribution after 50 PDL-FNC flight cycles.

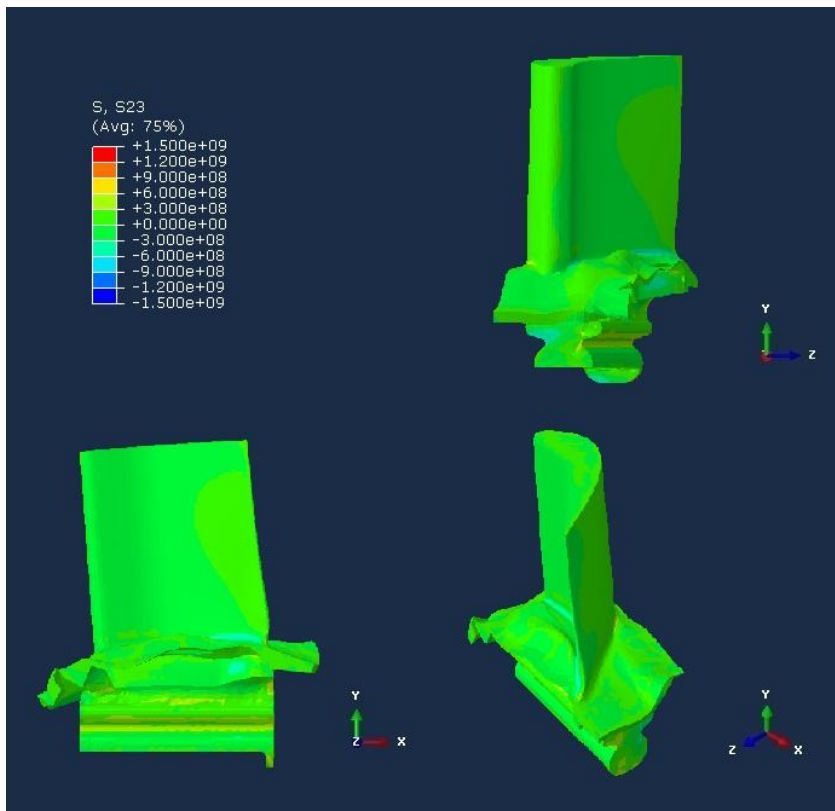


Figure A14 - Stress (S23) distribution after 50 PDL-FNC flight cycles.

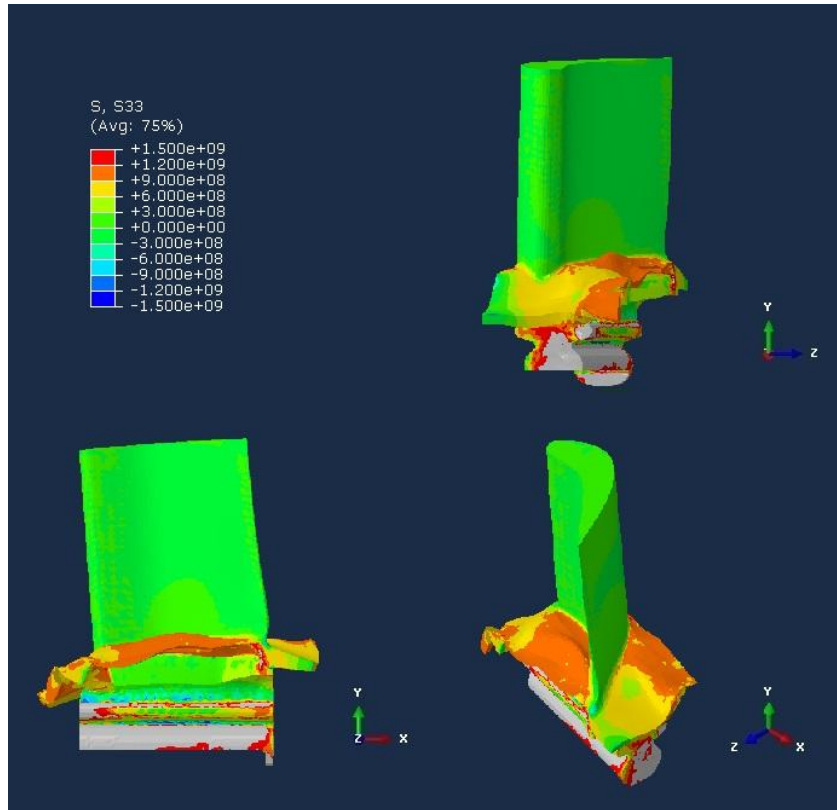


Figure A15 - Stress (S33) distribution after 50 PDL-FNC flight cycles.

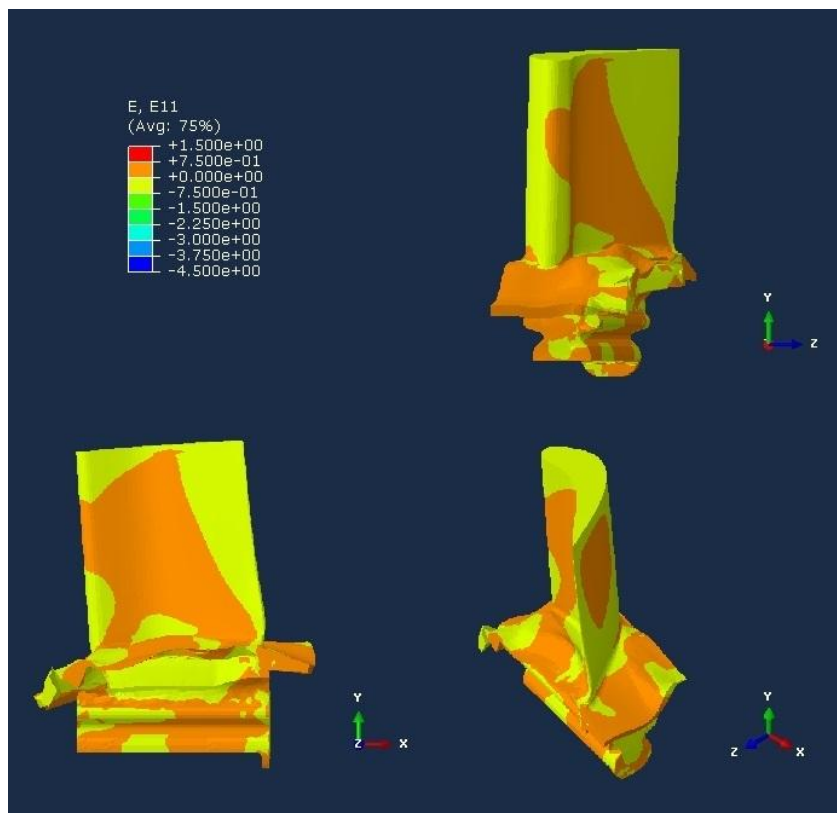


Figure A16 - Strain (E11) distribution after 50 PDL-FNC flight cycles.

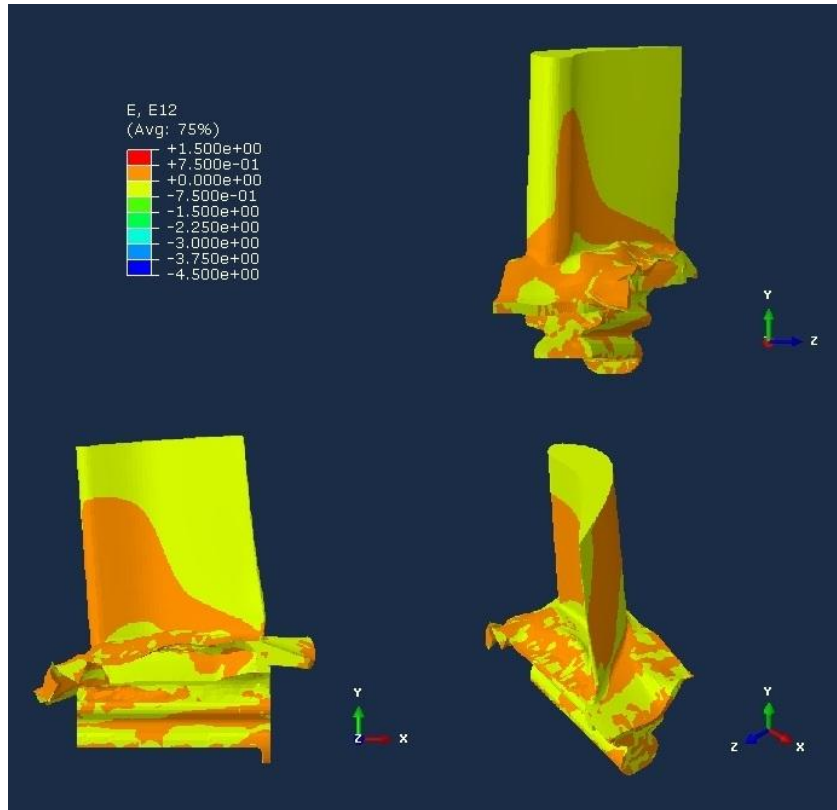


Figure A17 - Strain (E12) distribution after 50 PDL-FNC flight cycles.

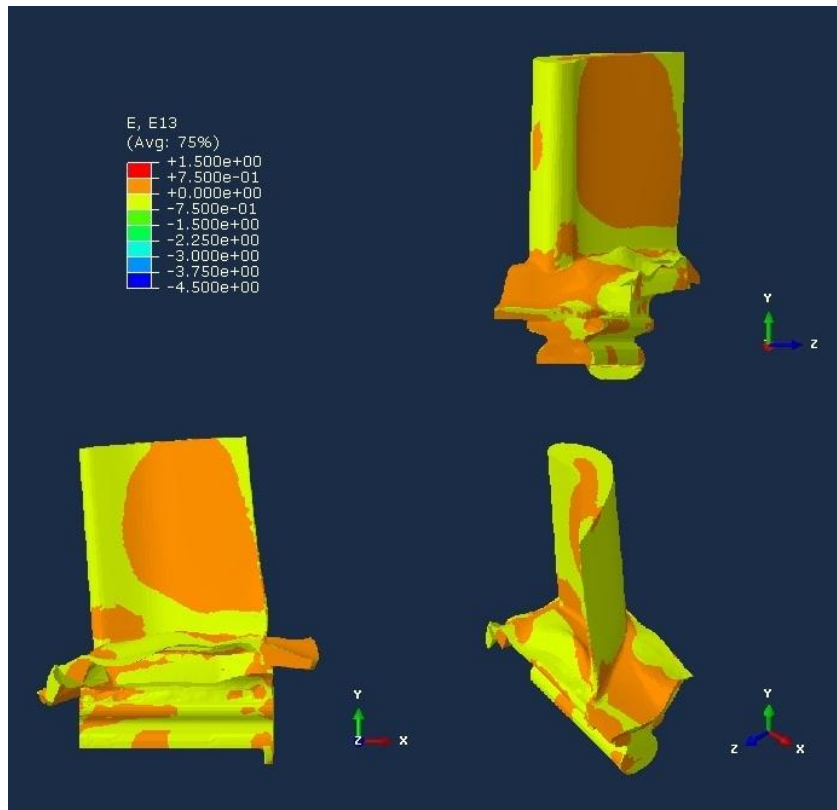


Figure A18 - Strain (E13) distribution after 50 PDL-FNC flight cycles.

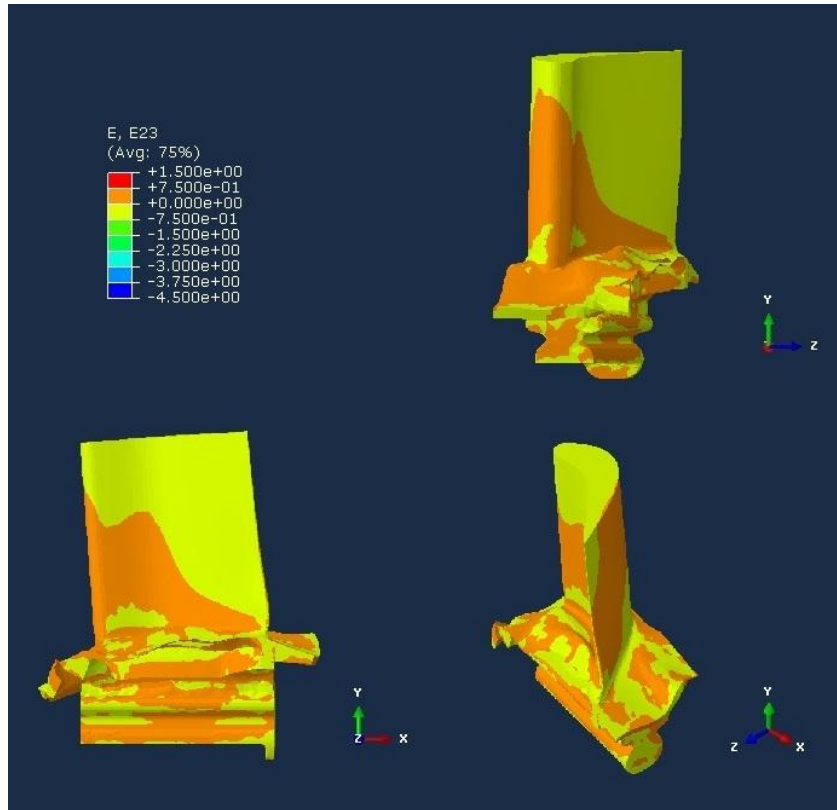


Figure A19 - Strain (E23) distribution after 50 PDL-FNC flight cycles.

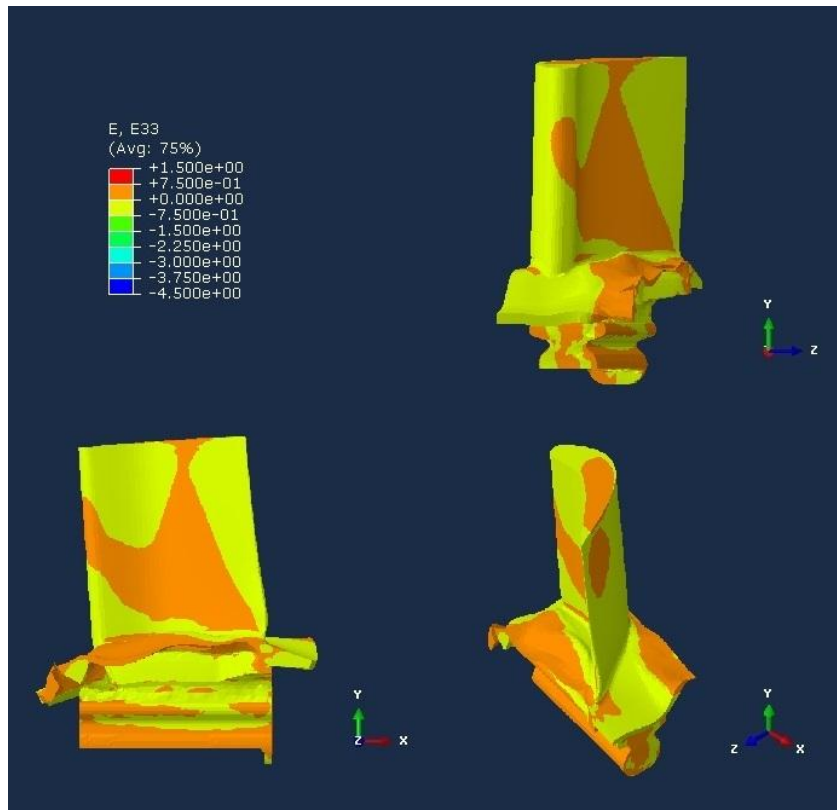


Figure A20 - Strain (E33) distribution after 50 PDL-FNC flight cycles.

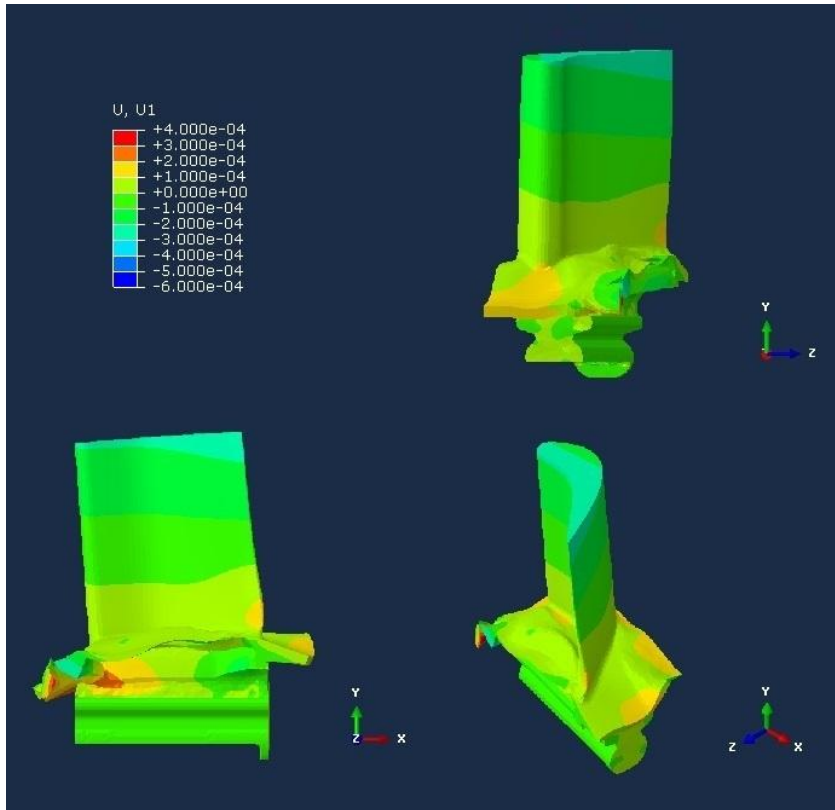


Figure A21 - Displacement (U1) distribution after 50 PDL-FNC flight cycles.

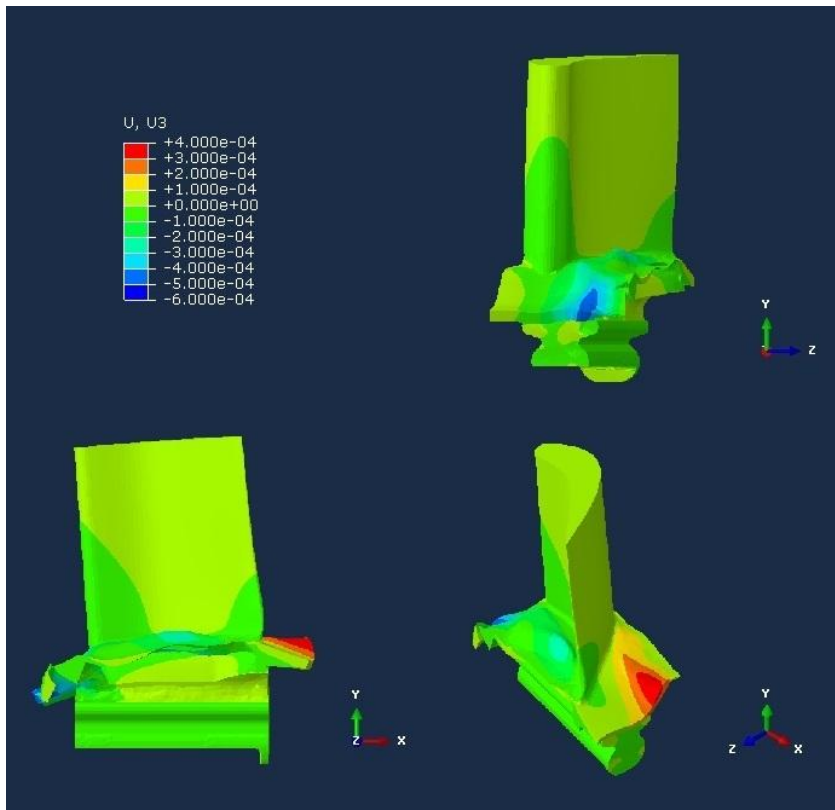


Figure A22 - Displacement (U3) distribution after 50 PDL-FNC flight cycles.